

**ELASTIC J/ψ MESON
PHOTOPRODUCTION
AT HERA**

Peter Bispham



THE UNIVERSITY
of MANCHESTER

High Energy Group
Department of Physics and Astronomy

March 1996

A thesis submitted to The University of Manchester
for the degree of Doctor of Philosophy in the Faculty of Science and Engineering

Contents

List of Figures	5
List of Tables	9
1 Introduction	16
2 The H1 Detector at HERA	18
2.1 The HERA Collider	18
2.2 The H1 Detector	20
2.2.1 Particle Tracking	21
2.2.2 Calorimetry	28
2.2.3 Muon Detection	32
2.2.4 Luminosity Measurement	35
2.2.5 Event Triggering	37
3 Photoproduction at H1	40
3.1 Kinematics of Photoproduction	40
3.2 The J/ψ Meson	42
3.3 Elasticity and Momentum Transfer	44
3.4 Diffractive J/ψ Production Mechanisms	44
3.4.1 Vector Meson Dominance	46
3.4.2 Monte Carlo Generator	47

<u>Contents</u>	3
3.4.3 QCD Inspired Models	48
3.4.4 The Pomeron	49
4 Event Selection	50
4.1 Level 5 Muon Classification	50
4.2 User Data Selection	53
4.3 Reconstructing Event Kinematics	54
4.3.1 J/ψ Kinematics	59
4.4 Muon Background Removal	59
5 Use of the Forward Direction	64
5.1 Forward Detector Performance in 1994	64
5.1.1 The Forward Muon Detector	65
5.1.2 Forward Tracker Performance	70
5.1.3 Forward Muon Trigger	72
5.2 Monte Carlo Simulation	73
5.2.1 Forward Muons in the Simulation	75
5.3 Forward Contribution to Kinematics	78
5.4 Angle and Momentum Measurement	81
5.4.1 Multiple Scattering	82
5.4.2 Momentum Loss	84
6 Measurement of $\sigma(\gamma p \rightarrow J/\psi p)$	89
6.1 Sources of Contamination	89
6.1.1 Tagging the Proton Remnant	90
6.1.2 Contribution from other Processes	91
6.2 Detector Acceptance	95
6.2.1 Geometric Acceptance	96
6.2.2 Trigger Selection	99

6.2.3	Trigger Efficiency	101
6.2.4	Selection Efficiency	106
6.2.5	Proton Veto Cuts	109
6.3	Luminosity and Branching Ratio	111
6.4	Photon Flux	112
6.5	Slope Parameter	117
7	Summary	122
A	Removal of Inelastic Events	124
	References	127

List of Figures

2.1	<i>Plan view of the HERA rings and the position of the H1 detector. The exploded view shows the various beam pre-accelerators.</i>	19
2.2	<i>Right-handed co-ordinate system used at H1.</i>	21
2.3	<i>Three dimensional view of the H1 Detector.</i>	22
2.4	<i>Side view of H1 Detector with individual sub-detectors labelled.</i>	23
2.5	<i>Relative arrangement of inner tracking detectors.</i>	24
2.6	<i>Details of the Forward Tracker.</i>	25
2.7	<i>Radial view of the central tracking detectors. The drift chambers CJC1 and CJC2 are shown, with the chambers CIZ and COZ labelled as Inner and Outer Z Chambers. The proportional chambers CIP and COP are labelled Inner and Outer MWPC respectively.</i>	27
2.8	<i>Calorimetry at H1 shown from a side view.</i>	29
2.9	<i>Electromagnetic radiation lengths (X_0) and nuclear interaction lengths (λ) in the liquid argon cryostat. Note that $1\lambda \simeq 20 X_0$.</i>	30
2.10	<i>The Forward Muon Detector. The diagram to the left shows the arrangement of the toroid, the θ and ϕ layers and the arrangement of drift cells on those layers. The diagram on the right-hand side shows some details of an individual drift cell.</i>	34
2.11	<i>Layout of the Luminosity System. The electron tagger and proton detector are labelled ET and PD respectively. The upper right diagram shows the lead filter and water Čerenkov calorimeter (VC). The upper left diagram shows a hit in the ET in the (x,y) plane.</i>	35
2.12	<i>Arrangement of scintillators of the Forward Proton Spectrometer in the (x,y) plane. The position of the beam-pipe is shown by the black circle.</i>	37

3.1	<i>Basic diagram of ep scattering via photoproduction. The 4-vectors of the electron, virtual photon and proton are labelled k, q and p respectively.</i>	41
3.2	<i>Elastic (upper diagram) and dissociative (lower) J/ψ production.</i>	45
3.3	<i>Diffraction elastic J/ψ production via soft pomeron exchange.</i>	46
3.4	<i>QCD-inspired gluon ladder model of the hard pomeron.</i>	48
4.1	<i>Elastic J/ψ decays as recorded in 1994 H1 data. The upper diagram shows a two-muon final state with one muon being detected in the Forward Muon Detector. The lower diagram shows a J/ψ decay in both side and radial views, where both muons are detected in the LAr calorimeter. The lower diagram also shows an example of a combined central/forward track.</i>	55
4.2	<i>The diagram to the left shows a comparison of generated (solid histogram) and reconstructed values (points) of the kinematic variable y for simulation of the elastic decay $J/\psi \rightarrow \mu^+ \mu^-$. The diagram to the right shows the distribution of the fractional difference between generated and reconstructed values.</i>	57
4.3	<i>Comparison of generated (left hand diagram) and reconstructed (right hand) values of variable z. Elastic diffractive Monte Carlo was used, corresponding to the decay $J/\psi \rightarrow \mu^+ \mu^-$.</i>	58
4.4	<i>Comparison of generated (solid histogram) and reconstructed (points) values of J/ψ energy, transverse momentum (P_T), θ angle and ϕ angle from simulation of the decay $J/\psi \rightarrow \mu^+ \mu^-$.</i>	60
4.5	<i>The left-hand diagram shows a comparison of generated (solid histogram) and reconstructed (points) values of the J/ψ pseudo-rapidity for simulation of the elastic decay $J/\psi \rightarrow \mu^+ \mu^-$. The fractional difference between generated and reconstructed values is shown in the diagram to the right.</i>	61
4.6	<i>Cosmic Event in 1994 data. The event is shown from side (main figure) and radial (upper right) views. The track kinematics are shown in the lower right figure in an Energy-η-ϕ distribution.</i>	62
5.1	<i>Example of unacceptably high currents drawn in layer θ_4 compared with the other three theta layers. The scale of the key alongside θ_4 shows units of μA.</i>	66
5.2	<i>The normalised relative number of hits in each voltage region for the layers ϕ_1 (upper) and θ_2 (lower). The quadrants are labelled $Q_{0...3}$.</i>	68
5.3	<i>The position of regions whose cells are powered by individual high voltage channels denoted Inner, Outer 1 and Outer 2. The upper plot shows their arrangement within a quadrant of a phi layer, the lower plot within a theta layer quadrant.</i>	69

- 5.4 Forward, combined, central and total track efficiencies for 1994 shown as a function of track angle theta. 71
- 5.5 Effect of our trigger selection on generated forward muons. Muon momentum is plotted against θ angle with no trigger selection (upper), and using our trigger selection (lower plot) without inclusion of the Forward Muon Trigger simulation. . 77
- 5.6 Invariant mass distribution for events containing one muon in the forward direction. The mean of the Breit-Wigner fit is (3.10 ± 0.03) GeV. The shaded area shows QED background events from Monte Carlo simulation of the process $\gamma\gamma \rightarrow \mu^+\mu^-$ 79
- 5.7 Contributions to J/ψ pseudorapidity from events found in data consisting of two central tracks, and those with one or two forward tracks (shaded histogram). . . 80
- 5.8 Contribution to the $W_{\gamma p}$ distribution from forward tracks (shaded histogram) and central tracks (solid histogram) in 1994 data. 82
- 5.9 A section of the H1 detector is shown, illustrating the angles θ_{FMD} , θ_{POE} and θ_{VTX} characteristic of multiple scattering. 83
- 5.10 Various distributions used in our study of multiple scattering. The upper two plots show differences in angle θ reconstructed from FMD hits (θ_{FMD}) and point of entry (θ_{POE}) compared with the vertex value (θ_{VTX}). The σ values of the left and right hand upper plots are expected to agree with the mean values of the corresponding left and right hand lower distributions, the latter obtained from muon momenta. 85
- 5.11 Momentum difference between measurements in the forward tracker and FMD for muons originating at the H1 vertex. Distributions are shown for data (points) and Monte Carlo simulation (solid histogram). 86
- 5.12 The upper plot shows forward momentum distribution of J/ψ events with one forward-going muon with our data sample and trigger selection (upper), and for 3 pb^{-1} of combined elastic/dissociative Monte-Carlo. The lower plot shows MC events found exclusively by simulation of the FMT for the same total luminosity. 87
- 6.1 Invariant mass distributions of di-muon pairs passing proton-veto cuts. The upper plot shows data fitted with a Gaussian plus linear background fit which is also shown by the dashed line. The lower plot shows data (points) compared with simulation (solid histogram) normalised to the data in the region $2.9 \text{ GeV} < M_{\mu^+\mu^-} < 3.3 \text{ GeV}$. The shaded area on both plots shows simulation of QED background normalised to the data luminosity of 2.89 pb^{-1} 92

- 6.2 Normalised resolutions of the reconstruction of $W_{\gamma p}$ (left hand upper and lower diagrams) and track angle θ (right hand) fitted with Gaussian and Breit-Wigner fits respectively. The upper plots correspond to events containing 2 central tracks, the lower plots for the case where at least 1 forward track is found in the event. 98
- 6.3 Efficiencies shown as a function of $W_{\gamma p}$ for the trigger elements (a) `dcrphi-Ta`, (b) `Mu_ECQ`, (c) `Mu_Bar` and (d) `Mu_BEC`. The points represent data values, the solid histogram shows simulation values, whose errors are not shown. 102
- 6.4 Efficiencies shown as a function of $W_{\gamma p}$ for the trigger elements comprising sub-trigger 54, (a) `dcrphi-TNeg`, (b) `Topo_BR` and (c) `zVtx_Cls`. The points represent data values, the solid histogram shows simulation values, whose errors are not shown. 103
- 6.5 Efficiencies of the instrumented iron detector (left hand diagram) and the muon-finding routine of the LAr calorimeter. The solid histogram shows Monte Carlo simulation, the points data. Errors on the simulated values are not displayed. . . 107
- 6.6 Invariant mass distributions (a) all pairs in elastic data class X, (b) events failing elastic cuts thus belonging to class Y. 109
- 6.7 Elastic J/ψ photoproduction cross section shown as a function of $W_{\gamma p}$. Results from previous experiments are included. The lines represent functions normalised to the E516 data point and correspond to VMD models with values of $\epsilon = 0.0808$ (dashed line) and $\epsilon = 0.225$ (solid line). The other data include various experiments at lower energy to HERA and also the published H1 and ZEUS results from 1993 running. 116
- 6.8 Slope parameter measurements. Distributions of $\frac{d\sigma}{dp_t^2}$ against p_t^2 are shown, where the points represent elastic data sample X (left hand diagram) and sample Y (right hand). The full histograms correspond to elastic and proton dissociation simulated events respectively. 118
- 6.9 J/ψ elastic slope parameters. The solid line represents the predicted rise according to soft pomeron theory, normalised to the E516 data point. The dashed line represents the case of zero shrinkage of the b parameter, also normalised to the same point. Inconsistency of results at lower $W_{\gamma p}$ than HERA is apparent. . . . 119

List of Tables

2.1	<i>Various properties of the HERA beams during 1994 operation, and their corresponding design values. Integrated luminosities shown are those delivered by HERA, and not necessarily those accepted by H1.</i>	20
3.1	<i>Currently accepted properties of the J/ψ charmonium state, including some principle decay modes and their branching ratios.</i>	43
3.2	<i>Generator values used in the production of the Monte Carlo files for elastic and proton-dissociative diffractive J/ψ production. The slope parameters are given at $W_{\gamma p} = 14 \text{ GeV}$.</i>	47
4.1	<i>Inner track cuts performed by the 1994 level 5 classification code for event class ECMUON.</i>	52
4.2	<i>1994 ECMUON cuts on muon tracks and links to inner tracks shown for the forward and backward endcaps (FEC and BEC), barrel region and Forward Muon Detector (FMD).</i>	53
5.1	<i>Status of the Forward Muon Detector during selected run ranges of 1994 data taking. The integrated luminosity collected for each range is also shown.</i>	65
5.2	<i>Elastic J/ψ Monte Carlo simulation. Properties of muon pairs from simulated J/ψ decay are shown, where p is the μ^\pm momentum in GeV. The numbers correspond to simulated luminosity of 60 pb^{-1}.</i>	75
5.3	<i>Proton-dissociative J/ψ Monte Carlo simulation. Properties of muon pairs from simulated J/ψ decay are shown, where p is the μ^\pm momentum in GeV. The numbers correspond to simulated luminosity of 20 pb^{-1}.</i>	75
5.4	<i>Elastic Monte Carlo simulation. Generated properties of J/ψ decay muons are shown, that have been selected by our set of sub-triggers.</i>	78

5.5	<i>Proton-dissociative Monte Carlo simulation. Generated properties of J/ψ decay muons are shown, that have been selected by our set of sub-triggers.</i>	78
6.1	<i>Currently accepted properties of the charmonium state ψ' including some principle decay modes branching ratios.</i>	93
6.2	<i>Geometric acceptances calculated using elastic VMD Monte Carlo where both muons fall in the range $7^\circ < \theta < 160^\circ$ together with their statistical errors. The effects of using simulation of proton dissociation, and with different VMD parameter are also shown. The reconstruction resolution of $W_{\gamma p}$ and θ is also shown. All errors are shown as percentages of the acceptance value for their $W_{\gamma p}$ bin.</i>	97
6.3	<i>Combinations of trigger elements constituting the heavy flavour sub-triggers labelled 18, 19, 22 and 54 at level 1 of the H1 trigger system.</i>	100
6.4	<i>Mean pre-scales and rates for our chosen sub-triggers during 1994 operation.</i>	100
6.5	<i>Difference between data and Monte Carlo for measured efficiencies of trigger elements $dcr\phi_Ta$, Mu_ECQ, Mu_Bar and Mu_BEC. Only the trigger elements $dcr\phi_Ta$ and $dcr\phi_TNeg$ display a difference in efficiency greater than statistical error.</i>	101
6.6	<i>Trigger acceptances calculated using elastic VMD Monte Carlo where both muons fall in the range $7^\circ < \theta < 160^\circ$, together with their statistical error. The effects of using simulation of proton dissociation, and with different VMD parameters are also shown. The reconstruction resolution of $W_{\gamma p}$ and θ is also shown. Errors shown are expressed as percentages of the acceptance values or each $W_{\gamma p}$ bin.</i>	104
6.7	<i>Comparison of data and simulation of the detection efficiencies of the two muon identification methods used for this analysis, and also the Forward Tracker.</i>	108
6.8	<i>Analysis acceptances calculated using elastic VMD Monte Carlo where both muons fall in the range $7^\circ < \theta < 160^\circ$. The systematic errors due to simulation of the Forward Tracker and muon detectors are also shown.</i>	108
6.9	<i>Values of acceptances of the proton-veto cuts applied to the data sample for each bin of $W_{\gamma p}$, denoted \mathcal{E}_{class}^{MC}. The values labelled $\Delta\mathcal{E}_{class}^{MC}$ are estimates of the systematic uncertainties of these cuts. The number of events in class X and Y are denoted N_X and N_Y and are quoted with their statistical error. The value of N_X corrected for dissociative events is labelled N_X^{corr} and is quoted together with its statistical and systematic errors.</i>	110
6.10	<i>Cross section σ_{ep} for the kinematic region $Q^2 < 4\text{ GeV}^2$. The parameters used in the calculation are shown in the upper table. A summary of the statistical and systematic errors encountered in the calculation is given in the lower table.</i>	113

6.11 *Photoproduction cross sections calculated for each bin of $W_{\gamma p}$. The bin centre values of $W_{\gamma p}$ are also shown.* 115

6.12 *Values of the slope parameter measured at lower and higher ranges of $W_{\gamma p}$. The first errors quoted are statistical, the second systematic. No evidence for increase of this parameter with increasing $W_{\gamma p}$ is found, with both values agreeing with the value of $(4.6 \pm 0.3 \pm 0.3) \text{ GeV}^{-2}$ measured across the entire range of $W_{\gamma p}$.* . 120

A.1 *Values of ζ_i ($i = 1, 2$) used in the correction for dissociative events shown for each bin of centre of mass energy $W_{\gamma p}$.* 125

Abstract

Presented is a measurement of the elastic cross section $\sigma(\gamma p \rightarrow J/\psi p)$ for photo-production of J/ψ mesons using data from the H1 detector at the HERA storage ring. Collisions of 27.5 GeV positrons with 820 GeV protons provide a detectable centre of mass energy between the proton and quasi-real photons radiated by the positron of $30 \text{ GeV} < W_{\gamma p} < 180 \text{ GeV}$. The measurement was made via the decay $J/\psi \rightarrow \mu^+ \mu^-$ using an integrated beam luminosity of 2.89 pb^{-1} from the 1994 HERA running period. This analysis extends the angular range of previous H1 analyses of this type by considering the use of the forward direction ($7^\circ \leq \theta \leq 25^\circ$). The cross section was found to rise with centre of mass energy from $(44 \pm 19 \pm 13) \text{ nb}$ measured at $W_{\gamma p} = 50 \text{ GeV}$ to $(71 \pm 18 \pm 15) \text{ nb}$ at $W_{\gamma p} = 146 \text{ GeV}$, the former figure evaluated from muons detected in the forward direction. These results cannot be explained by the interchange of a Donnachie-Landshoff soft pomeron between proton and photon when compared with previous results at $W_{\gamma p} \lesssim 14 \text{ GeV}$. The use of the Forward Muon Detector for analysis of this type is explored, and found to possess great potential for higher integrated luminosities of future HERA running periods.

No portion of the work referred to in this thesis has been submitted in support of an application for another degree or qualification of this or any other institute of learning.

Copyright in text of this thesis rests with the author. Copies (by any process) either in full, or of extracts, may be made **only** in accordance with instructions given by the author and lodged in the John Rylands University Library of Manchester. Details may be obtained from the librarian. This page must form part of any such copies made. Further copies (by any process) of copies made in accordance with such instructions may not be made without the permission (in writing) of the author.

The ownership of any intellectual property rights which may be described in this thesis is vested in the University of Manchester, subject to any prior agreement to the contrary, and may not be made available for use by third parties without the written permission of the University, which will prescribe the terms and conditions of any such agreement.

Further information on the conditions under which disclosures and exploitation may take place is available from the Head of Department of Physics and Astronomy.

This work was supported financially by the Particle Physics and Astronomy Research Council (PPARC), formerly the Science and Engineering Research Council (SERC), between October 1992 and October 1995.

The author was educated at Rainhill High School, Merseyside, between 1982 and 1989. In 1992 he was awarded a 1st class BSc (Hons.) degree in Physics with Astrophysics at the University of Leicester. The work presented in this thesis was conducted at the University of Manchester and the Deutches Elektronen Synchotron (DESY), Hamburg.

Posthumously dedicated to

Daniel John Hughes

(1970-95)

Chapter 1

Introduction

The J/ψ meson has been studied at a number of experiments since its discovery in 1974, and many of its properties are well understood. Previous photoproduction experiments operated at centre of mass energies of $W_{\gamma p} \lesssim 30$ GeV. This figure is to be compared with the 1994 centre of mass energy at HERA of $\sqrt{s_{ep}} = 300$ GeV allowing measurements to be made¹ at a mean photoproduction centre of mass energy of $W_{\gamma p} \approx 90$ GeV. This allows us to extend the energy range of γp cross section measurements for the J/ψ meson considerably.

Elastic J/ψ photoproduction at the HERA $e^\pm p$ collider provides very clean events, with neither the proton nor the scattered electron (or positron) being detected in the main detector, and the proton remaining intact after the interaction. Only the final state of the J/ψ decay is detected, consisting of oppositely charged pairs of electrons or muons, or more often a hadronic system. This analysis specifically examines the branching of the J/ψ into a di-muon pair.

One of the main goals of the H1 detector is the identification and measurement of highly energetic particles, especially electrons and muons. This thesis attempts to extend J/ψ analysis to the forward region, and examines in particular the use of the Forward Muon Detector (FMD). This forward area has not been studied before for this type of analysis, and the rôle of the FMD with future integrated

¹Taking detector acceptance into consideration.

luminosities approaching the design value of 100 pb^{-1} per year [1] is explored. The clean environment of elastic $J/\psi \rightarrow \mu^+ \mu^-$ decay provides an ideal opportunity to assess detector performance.

It is eventually hoped that inelastic J/ψ production, where the scattered proton does not remain intact, will provide an opportunity to extract the gluon distribution of the proton, a task for which total integrated luminosity of 20 pb^{-1} is thought to be required [2].

Throughout the course of this thesis, descriptions of detectors correspond to their status during 1994 data taking, and all analysis is done with data collected during that year. Chapter 2 gives an overview of the HERA collider, the H1 detector and its component sub-detectors. Chapter 3 gives an introduction to photoproduction physics at HERA, explaining the kinematics involved and the J/ψ production mechanisms studied in this analysis. Practical reconstruction of the event kinematics, track cuts and event selection are discussed in chapter 4. Specific assessment of the forward direction is made in chapter 5, which includes a summary of the Forward Muon Detector status during 1994. The calculation of the photoproduction cross section $\sigma(\gamma p \rightarrow J/\psi p)$ is presented in chapter 6 and the entire analysis summarised in chapter 7.

Chapter 2

The H1 Detector at HERA

Presented in this chapter is an overview of the various detectors and procedures used in data taking at the H1 particle physics experiment. Also described are the HERA accelerator and the collisions this machine provided during 1994 operation.

2.1 The HERA Collider

The **H**adron **E**lectron **R**ing **A**ccelerator is the worlds first $e^\pm p$ collider. Commissioned in 1985, with first collisions achieved in 1992, electrons and protons are accelerated in vacuo in opposite directions around rings of 6.3 km circumference. The collider is situated 15-20 m underground at the DESY laboratory, Hamburg, Germany.

Figure 2.1 shows a plan view of the layout of the HERA accelerator and various pre-accelerators of the beams. Electrons are injected into the HERA ring with 12 GeV (pre-accelerated by LINAC2, DESY2 and PETRA2), while protons have 40 GeV on injection (LINAC3, DESY3 and PETRA2). The beam momenta are then increased up to their full values by HERA, which for 1994 were 27.5 GeV for electrons/positrons, and 820 GeV for protons¹. In 1994 HERA operated with

¹Note that values of particle momentum and mass included in this thesis are given in units of GeV rather than GeV/c and GeV/c² respectively.

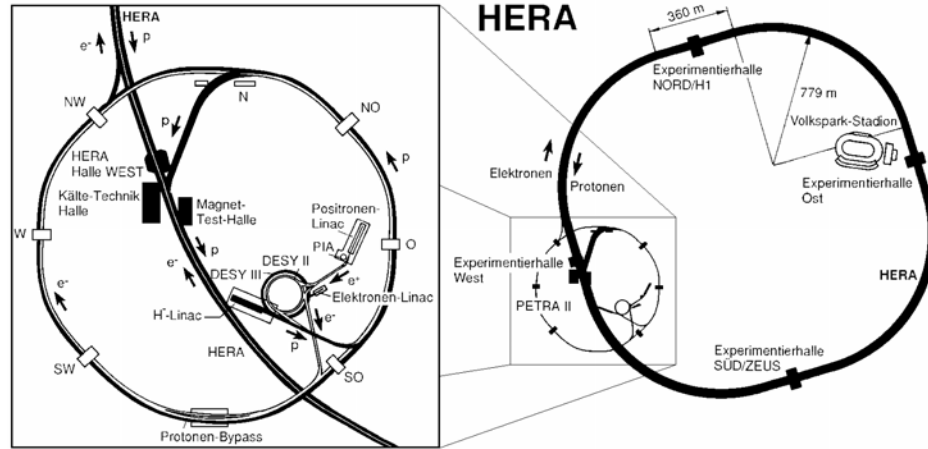


Figure 2.1: Plan view of the HERA rings and the position of the H1 detector. The exploded view shows the various beam pre-accelerators.

153 colliding bunches of electrons and protons together with smaller numbers of non-colliding satellite bunches used for monitoring the background introduced from the individual beams.

Yearly increases in integrated beam luminosity² have occurred from 25 nb^{-1} in 1992 to 3.9 pb^{-1} in 1994. Originally an e^-p collider, it was from summer 1994 that e^+p collisions were attempted for the first time, corresponding to approximately 85 % of useful data for that year.

Table 2.1 shows some parameters of 1994 HERA running, together with the design values for each quantity. Note that the centre of mass energy provided in 1994 of $\sqrt{s_{ep}} = 300 \text{ GeV}$ falls short of its design value of $\sqrt{s_{ep}} = 314 \text{ GeV}$ due to the energy of the electron beam falling below the design value of 30 GeV. However, this 1994 value itself constitutes an improvement upon the 1993 centre of mass energy achieved of 296 GeV, with an electron beam of 26.7 GeV momentum.

²The luminosities shown are those delivered by HERA during H1 runs of sufficient quality for physics analysis.

<i>Beam Parameter</i>		<i>Design</i>		<i>1994</i>	
		e-beam	p-beam	e-beam	p-beam
Energy	(GeV)	30	820	27.5	820
Number of Bunches		210	210	153	153
Beam Current	(mA)	58	163	17	41
Lifetime	(h)	4-10	>100	4-10	>100
Bunch Separation	(ns)	96		96	
Specific Luminosity	($\text{cm}^{-2}\text{s}^{-1}$)	1.5×10^{31}		1.4×10^{30}	
Integrated Luminosity	($\text{pb}^{-1}\text{y}^{-1}$)	100		5.5	
CM Energy	(GeV)	314		300	

Table 2.1: Various properties of the HERA beams during 1994 operation, and their corresponding design values. Integrated luminosities shown are those delivered by HERA, and not necessarily those accepted by H1.

2.2 The H1 Detector

To measure charged particles and jets produced from $e^\pm p$ interactions, the H1 magnetic detector has been assembled around one of the points of collision of the HERA storage ring. In addition to momentum and energy measurements of particles produced from these interactions, it is also necessary to have a complex triggering system to select interesting physics events from background. A system to measure the luminosity captured by H1 from that delivered by HERA is also very important.

The co-ordinate system used at H1 is shown in figure 2.2. The right-handed Cartesian (x, y, z) co-ordinate system has its positive z axis defined as the direction of the proton beam, and the x axis horizontal. The nominal H1 interaction vertex is located at $(0, 0, 0)$. The proton direction is that for which $\theta = 0$ and z positive, with the region $\theta < 90^\circ$ known as the forward direction. The direction opposite to that of the incoming proton and $\theta > 90^\circ$ is then known as backward. Due to the imbalance

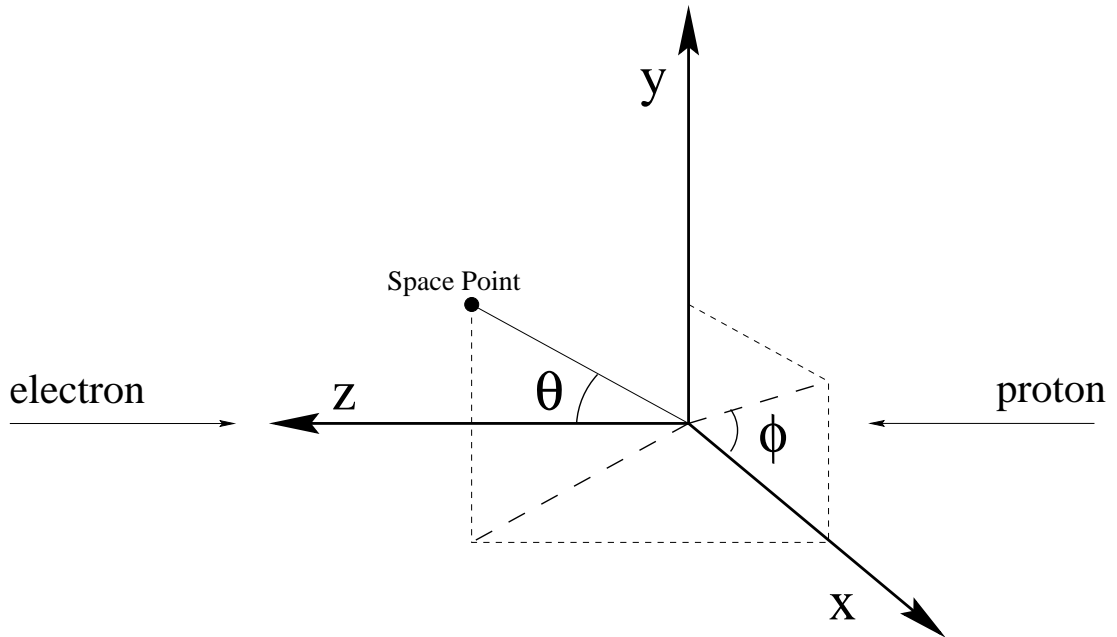


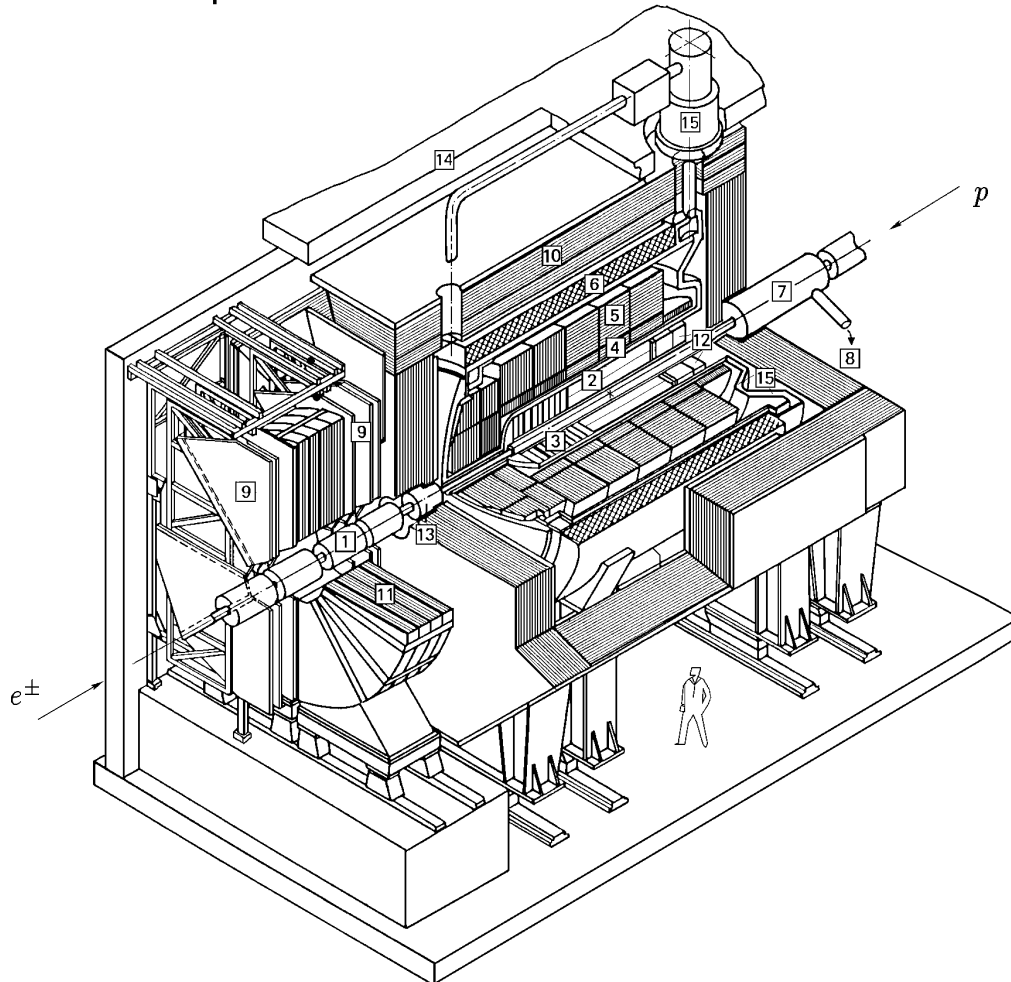
Figure 2.2: *Right-handed co-ordinate system used at H1.*

in the energy of the proton and electron beams, typical events within the detector have an asymmetric topology, with a Lorentz boost in the forward direction. This is reflected in the design of the detector, whose asymmetric arrangement of sub-detectors is shown in figures 2.3 and 2.4.

2.2.1 Particle Tracking

The tracking system at H1 can be divided into three major components. The Central Tracker (CT) detector covers the angular region $15^\circ < \theta < 165^\circ$, with the higher level of instrumentation required for the Lorentz boost in the forward direction provided by the Forward Tracker (FT) for the range $7^\circ < \theta < 25^\circ$. The backward region of $155.5^\circ < \theta < 174.5^\circ$ is further covered by the Backward Proportional Chambers (BPC). The relative arrangement of these components is shown in figure 2.4 and in more detail in figure 2.5.

HERA Experiment H1



- | | | | |
|---|---|----|--|
| 1 | Beam pipe and beam magnets | 9 | Muon chambers |
| 2 | Central tracking chambers | 10 | Instrumented Iron (iron stabs + streamer tube detectors) |
| 3 | Forward tracking and Transition radiators | 11 | Muon toroid magnet |
| 4 | Electromagnetic Calorimeter (lead) | 12 | Warm electromagnetic calorimeter |
| 5 | Hadronic Calorimeter (stainless steel) | 13 | Plug calorimeter (Cu, Si) |
| 6 | Superconducting coil (1.2T) | 14 | Concrete shielding |
| 7 | Compensating magnet | 15 | Liquid Argon cryostat |
| 8 | Helium cryogenics | | |

Figure 2.3: Three dimensional view of the H1 Detector.

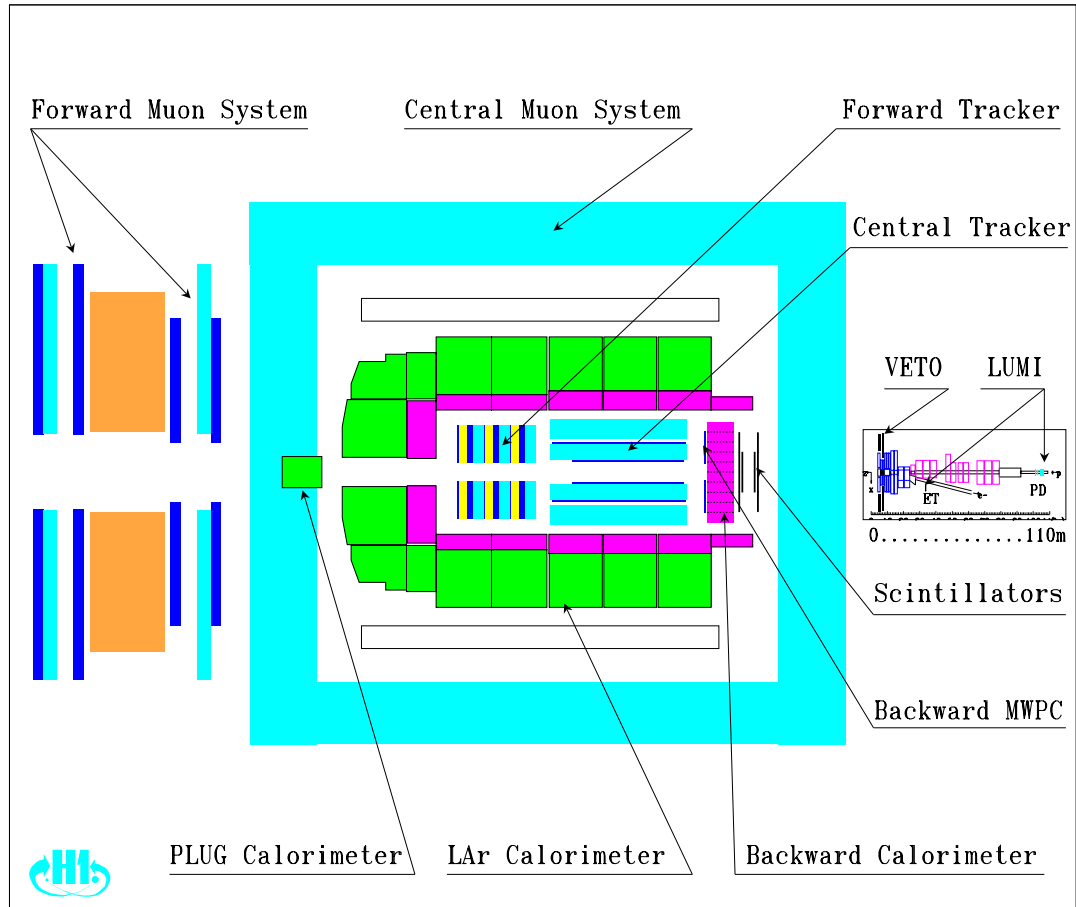


Figure 2.4: Side view of H1 Detector with individual sub-detectors labelled.

The paths of charged particles within H1 are bent by a longitudinal, homogeneous ($\Delta B/B < 2\%$) magnetic field of 1.12 T, provided by a superconducting solenoid in the central region. This solenoid is cooled by liquid helium and the field surrounded by an octagonal iron return yoke. A compensating magnet is located at the proton entrance side of H1 to provide a longitudinal field equal and opposite to that of the H1 main solenoid, such that $\int B_z dz = 0$. The determination of the bending effect of the field on tracks is made using the tracking detectors, providing a measurement of track momenta. The super-conducting coil providing the main field and the compensating magnet are labelled [6] and [7] in figure 2.3 respectively.

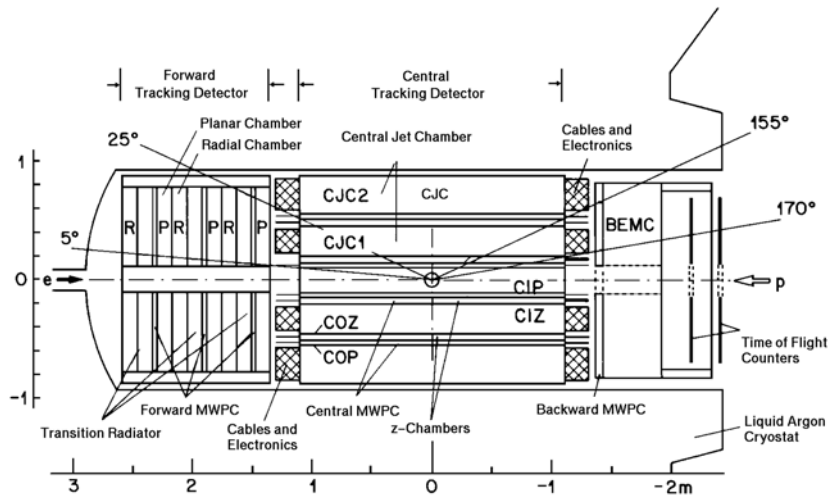


Figure 2.5: Relative arrangement of inner tracking detectors.

The Forward Tracker

Labelled [\[3\]](#) in figure 2.3, the Forward Tracker consists of three units, or supermodules, which are shown in figure 2.6. These almost identical supermodules are labelled 0 to 2 with supermodule 0 being that closest to the H1 interaction point. Each supermodule consists of planar drift chambers, a multi-wire proportional chamber (MWPC) and radial drift chambers.

The planar chambers consist of 3 planes, each 4 wires deep and offset at 60° with respect to one another in the (x, y) plane. They are designed to provide an accurate reconstruction of the θ co-ordinate of a track. The planar chambers appear at the front of each supermodule as it is more straightforward to link track segments in these chambers to tracks in the central tracking detector where appropriate.

The MWPC planes are used to provide a signal to act as a trigger for tracks traversing the detector. They are situated behind the planar chambers partly for convenience as they both share the same gas mixture. In addition, placing them here rather than at the end of each supermodule maximises the efficiency of the trigger within each supermodule. If both the planes of pad readout comprising the MWPC

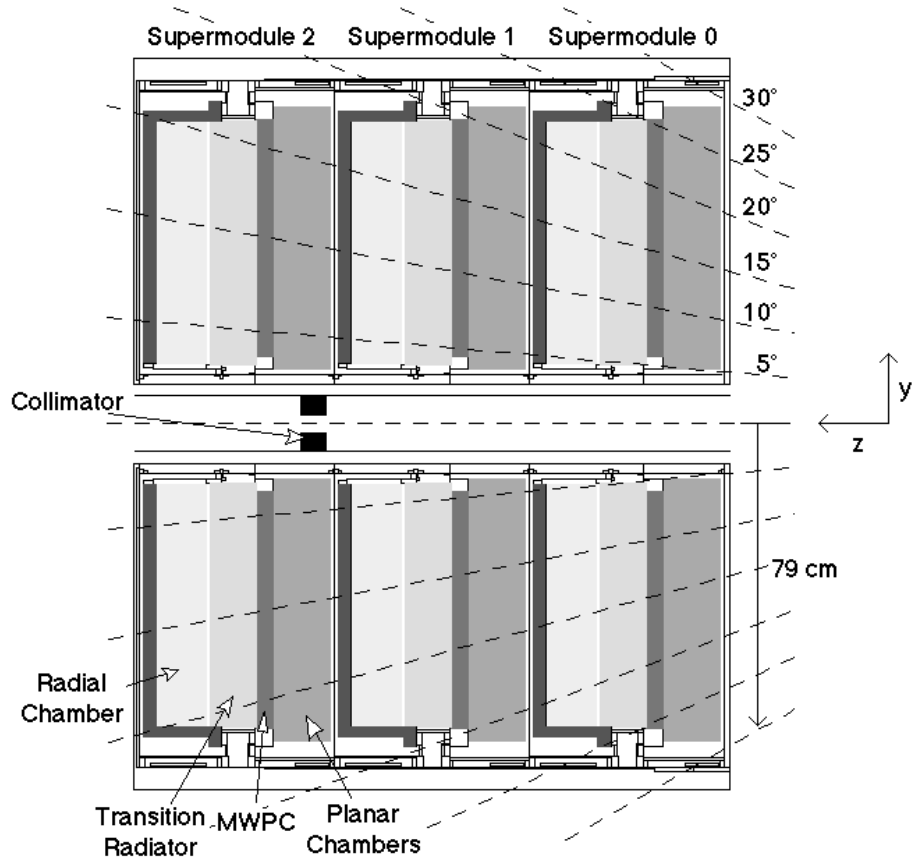


Figure 2.6: Details of the Forward Tracker.

give a signal, then this constitutes a trigger signal. Located after the MWPC (as z increases) comes a Transition Radiator (TR), designed to enable $e - \pi$ separation in the Forward Tracker. This is done by e^\pm traversing the TR producing X-rays which are detected as ionisation charge in the radial chambers situated at higher z , with some success [3].

The radial chambers consist of planes of radially arranged wires with a separation of 10 mm in z between the planes. They are designed to provide an accurate measurement of the azimuthal angle ϕ over the entire range $0^\circ < \phi < 360^\circ$. A coarse measurement of the angle θ can also be made using charge division in the radial wires.

A momentum resolution of $\sigma_p/p < 0.03 p$ for the Forward Tracker has been achieved [4] for tracks with momenta above 3 GeV linked to the event vertex. The track angular resolution is $\sigma_{\theta,\phi} < 1$ mrad, with σ_θ as low as 0.2 mrad for high momenta tracks containing segments in all three supermodules. The total sensitive region in the z direction provided by the FT is between $134 \text{ cm} < z < 254 \text{ cm}$.

The Central Tracker

In a similar way to the Forward Tracker, the Central Tracker is responsible for the reconstruction and triggering of tracks in its own angular range, namely $15^\circ < \theta < 165^\circ$. However, charged tracks with angle $\theta < 30^\circ$ or $\theta > 150^\circ$ have lower reconstruction accuracy in the Central Tracker than the angular range between these limits. Labelled 2 in figure 2.3, it consists of two large concentric drift chambers [5] CJC1 and CJC2 for track reconstruction, and two thin drift chambers CIZ and COZ for measurement of the z co-ordinate. Triggering of tracks is done by concentric layers of proportional chambers named CIP and COP, with the COP (outer) having a radius of around 3 times larger than the CIP (inner). The detailed arrangement of these chambers is shown in figure 2.7.

The drift chambers CJC1 and CJC2 consist of wires arranged in the z direction and are designed to accurately measure the transverse momenta of tracks passing through it. The direction of drift of free charge produced in these chambers is tangential about the axis. These chambers can achieve a space point resolution of $170 \mu\text{m}$ in the drift direction, and by charge division a resolution of 1% can be achieved in the z co-ordinate. This z measurement is complemented by the resolution of $300 \mu\text{m}$ provided by the z chambers CIZ (inner) and COZ (outer).

The Backward Proportional Chambers

As with the MWPC devices of the Forward and Central Trackers, those in the backward direction are designed to provide a response time below that of two bunch crossings of the HERA beam. They also provide a coarse space point

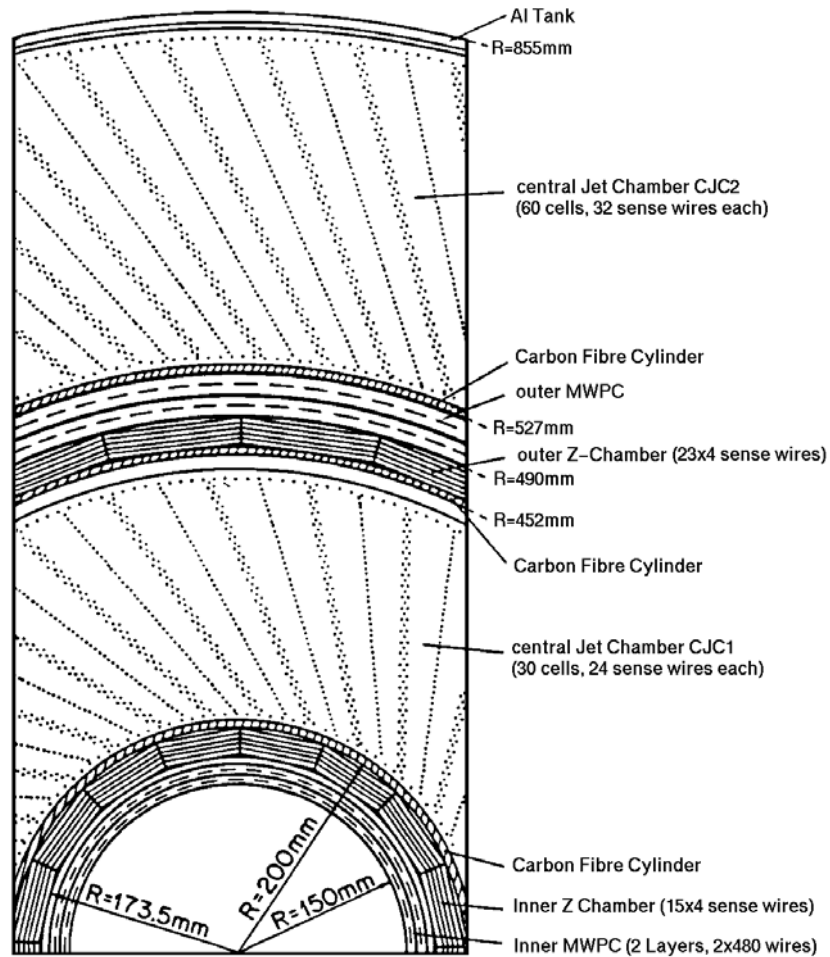


Figure 2.7: Radial view of the central tracking detectors. The drift chambers CJC1 and CJC2 are shown, with the chambers CIZ and COZ labelled as Inner and Outer Z Chambers. The proportional chambers CIP and COP are labelled Inner and Outer MWPC respectively.

determination for the trigger decision as to whether to reject or keep each event (see section 2.2.5). The space point information it provides is also useful to gain a more accurate track fit in this region, particularly if backward-going tracks of small angle leave very few drift chamber points in the central drift chambers.

2.2.2 Calorimetry

The calorimetry at H1 is separated into electromagnetic and hadronic calorimeter detectors. In both sets of calorimeters the energy of incident particles is measured by sampling particle showers they induce in the calorimeter medium, although the physical mechanism by which these showers occur is rather different for each of the electromagnetic and hadronic cases.

One of the chief considerations in the design of a calorimeter is the radiation length, X_0 for the electromagnetic case, and its hadronic analogy the nuclear interaction length, λ . In both cases they are a measure of the length of the shower, and are characteristic of the calorimeter medium. The nuclear interaction length λ is typically much greater than X_0 for a particular medium, for example $\lambda \simeq 30 X_0$ for lead. In all calorimeters at H1, showers are induced in layers of suitable material, with the shape and energy of the shower sampled by regularly spaced sensitive regions within this medium.

The calorimeters at H1 consist of the main liquid argon (LAr) electromagnetic and hadronic cryostat (EMC and HAC respectively), the Backwards Electromagnetic Calorimeter (BEMC), and the plug and tail-catcher (TC) hadronic calorimeters. Diagram 2.8 shows these calorimeters and their relative positions in the layout of H1. The EMC, HAC and plug are also labelled 4, 5 and 13 in figure 2.3.

Noise in the calorimeters is sampled using special H1 runs during which random event triggers are used without any noise suppression in order to find the level of background noise in each calorimeter. These background values are then included in the physical simulation of the H1 detector.

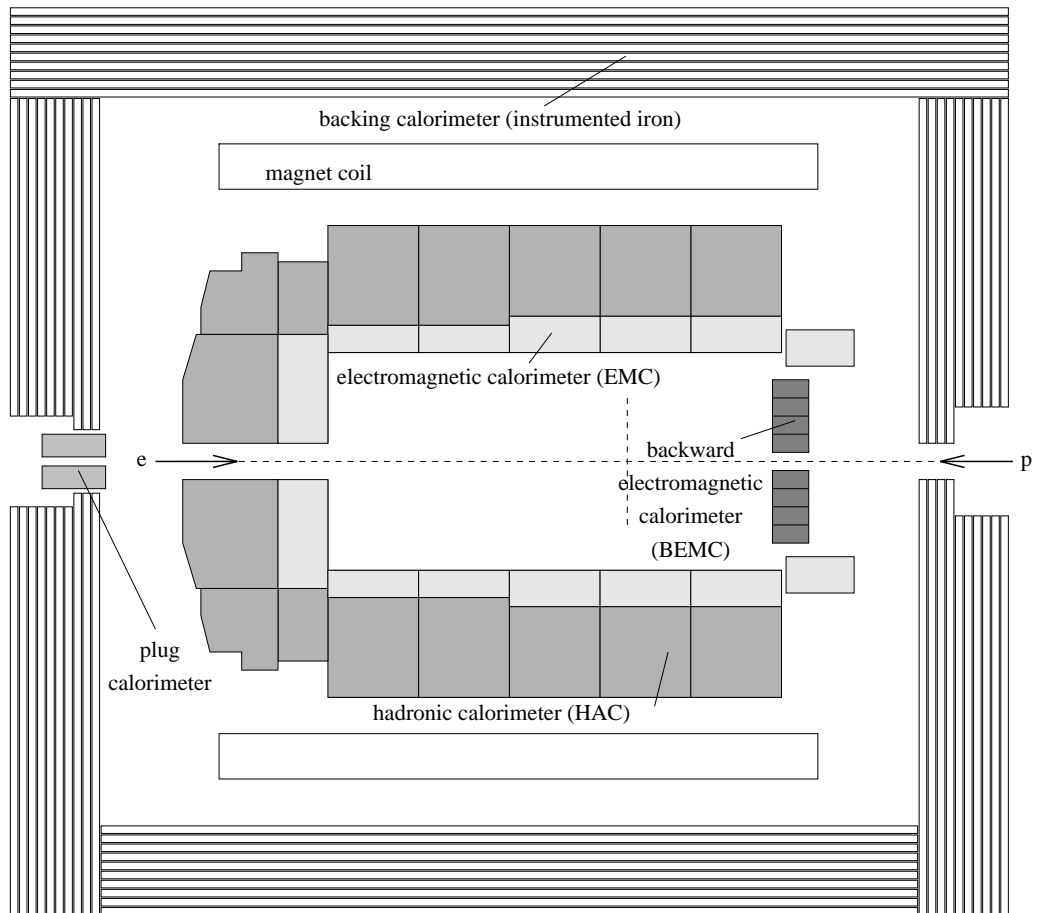


Figure 2.8: Calorimetry at H1 shown from a side view.

Electromagnetic Calorimeters

These exist to measure energy deposited by electrons and photons from interactions at the H1 vertex. Pair production³ and bremsstrahlung radiation from the leptons cause particle showers along the direction of the incident particle. The length along this direction that this shower may extend to is governed by the radiation length of the medium.

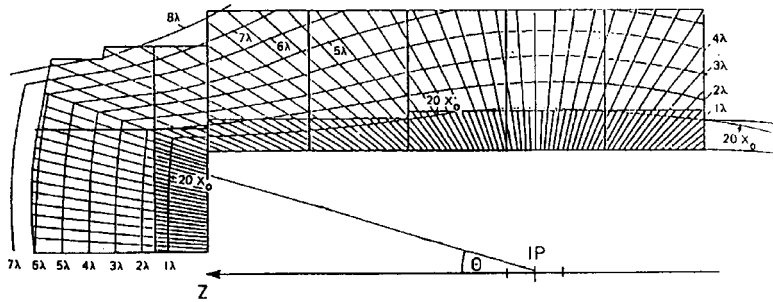


Figure 2.9: Electromagnetic radiation lengths (X_0) and nuclear interaction lengths (λ) in the liquid argon cryostat. Note that $1\lambda \simeq 20X_0$.

The electromagnetic section of the LAr calorimeter covers the angular range 4° to 153° , and has a depth of ≈ 20 radiation lengths as shown in figure 2.9. The calorimeter is divided into a large number of cells to give very fine granularity, necessary to reconstruct clusters from these cells. A reconstruction program is used for this purpose, with a close correspondence between these clusters and particle showers. Background is reduced by ignoring calorimeter cells which cannot be associated with any cluster. Showering in the calorimeter is provided by a series of 2.4 mm thick lead plates, with the areas of 2.35 mm thickness between these plates containing liquid argon instrumented by a series of readout pads. The energy resolution provided by this method is given by $\frac{\sigma_E}{E} = \frac{12\%}{\sqrt{E}} \oplus 1\%$ [6] where E is the particle energy in GeV. The calorimeter was calibrated off-site at CERN before installation at DESY and currently has an uncertainty in calibration of 3%.

³The process $\gamma \rightarrow e^+ e^-$.

The BEMC is a lead-scintillator calorimeter, with the lead providing the showering to be detected by the scintillator layers. The length of the calorimeter is equivalent to 22.5 radiation lengths, but only 0.3λ . It is situated in the negative z direction as shown in figure 2.8, and is primarily concerned with the detection of the scattered beam lepton (e^\pm) in deep inelastic scattering (DIS) events. The angular range of the detector of $151^\circ < \theta < 177^\circ$ covers the kinematic range $4\text{ GeV} \lesssim Q^2 \lesssim 100\text{ GeV}^2$ (see section 3.1), this range dominating the DIS cross section. The dominant source of noise in this calorimeter comes from the proton beam.

Hadronic Calorimeters

The mechanism of shower development in the hadronic case is mainly via inelastic nuclear collisions. Hadronic energies detected in clusters tend to be $\simeq 30\%$ less than the energy of the incident hadron. The missing energy is lost in nuclear excitations for example, or other unseen processes.

The hadronic section of the liquid argon cryostat constitutes the main hadronic calorimeter at H1, and is situated further from the nominal interaction point than the electromagnetic section due to radiation length considerations, since $\lambda \gg X_0$. This arrangement is shown in figure 2.9. In this outer section, 2.4 mm layers of instrumented LAr are interspersed with 19 mm layers of stainless steel. It is this latter component that causes showering. Energy resolution in this set of cells is poorer than in the EMC, and is $\frac{\sigma_E}{E} = \frac{50\%}{\sqrt{E}} \oplus 2\%$ [7] with 5% calibration uncertainty. Clusters identified as hadronic by virtue of their topology must be appropriately weighted in order to compensate for the 30% energy loss from nuclear processes mentioned earlier in this section.

The plug is designed to cover the missing angular range in the proton direction of $0.6^\circ \lesssim \theta \lesssim 4^\circ$. This hadronic calorimeter is made of alternate layers of copper absorber to provide showers, and silicon detectors to sample them. The total of 17 layers cover a range in the z co-ordinate of $476\text{ cm} < z < 545\text{ cm}$, equivalent to 4.25λ . Its main purpose is to detect hadrons emitted close to the beam pipe.

Part of the instrumented iron muon detector is used to measure hadronic energy leaking out of the HAC, and is also known as the tail-catcher (TC). The instrumented iron consists of 16 limited streamer tube (LST) layers, 10 of which have additional pads (readout electrodes) to sample the tail of such cluster development. The angular range covered by the TC is between 6° and 172° , with a depth of 4.5λ . The energy measurement has a resolution of $\frac{\sigma_E}{E} \simeq \frac{100\%}{\sqrt{E}}$, the poorest of the individual calorimeter components.

2.2.3 Muon Detection

The iron return yoke of the H1 magnetic field has been instrumented to provide accurate detection of muons penetrating the inner detectors. The location of these muon chambers are shown in figure 2.4 and labelled 10 in figure 2.3. In addition to this system, due to the asymmetry in beam energy and hence in particle density, a forward muon spectrometer has been assembled in the proton direction (+z) as shown in figure 2.4, with its components labelled 9 and 11 in figure 2.3. These ‘outer’ detectors themselves provide only reasonable momentum measurement of the muons they detect, their principle aim being to identify which of the tracks in the inner tracking detectors were left by muons. This allows us to take advantage of the greater accuracy of momentum measurements provided by these inner detectors.

The Iron Chambers

As mentioned in section 2.2.2, the iron return yoke is instrumented with layers of limited streamer tubes. Their primary purpose is the detection of muons from the event vertex. The iron may be separated into three components, the forward endcap ($6^\circ < \theta < 33^\circ$), the barrel region ($33^\circ < \theta < 137^\circ$) and the backward endcap ($137^\circ < \theta < 172^\circ$). The layout of the iron instrumentation in the endcaps provides position measurement of muon impact according to an (x,y) co-ordinate system, whereas the barrel uses a (z, ϕ) set of co-ordinates.

The LST arrangement consists of 16 wire layers, 5 strip and 11 pad layers to be used in track reconstruction. Wire hits have spatial resolution of 3-4 mm, strips provide 10-15 mm resolution with the corresponding figure for the pads being ≈ 10 cm. Using the magnetic field strength at the return yoke, an approximate momentum measurement may be made. The B field varies strongly inside the iron plates so the mean field for each gap in the layers is used in the measurement. The lower momentum limit is generally around 1.5 GeV for a muon to penetrate the iron sufficiently to be detected, with this value as high as 2 GeV for the forward endcap.

The Forward Muon Detector

Covering the angular range $3^\circ \leq \theta \leq 17^\circ$, the Forward Muon Detector (FMD) consists of a series of planes of drift chambers used in conjunction with its own separate toroidal magnet of 1.6 T to complement high energy muon detection in this region [8]. The planes of the detector consist of a number of drift cells mounted onto a large metal frame. An example cell is shown in figure 2.10. These are essentially boxes of 12 cm width, 2 cm thickness and of varying length. A central sense wire runs along the length of each cell, the cell itself containing a gas mixture of 92.5 % Ar, 5 % CO₂ and 2.5 % CH₄. Electrodes are arranged along the length of the inside of each cell providing an almost uniform electric field across the cell width. Ionisation charge produced by muons in the gas mixture drifts in the electric field to the sense wire at around $5 \text{ cm}\mu\text{s}^{-1}$. The overall spatial accuracy of a cell is currently estimated to be $\approx 350 \mu\text{m}$ perpendicular to the sense wire, compared with a design figure of $250 \mu\text{m}$. This drift velocity is measured using special runs, the details of which are described elsewhere [9], while attempts to calibrate these cells off-site have been made [10][11].

Three planes are arranged before and behind the toroid, with the first and third layers in each case having their sense wires aligned to provide accurate measurement of the θ co-ordinate of a muon track, with ϕ measured by the intermediate second layer. This arrangement is shown in figure 2.10. The bend in the path of muons caused by the field of the toroid is used in conjunction with the measured

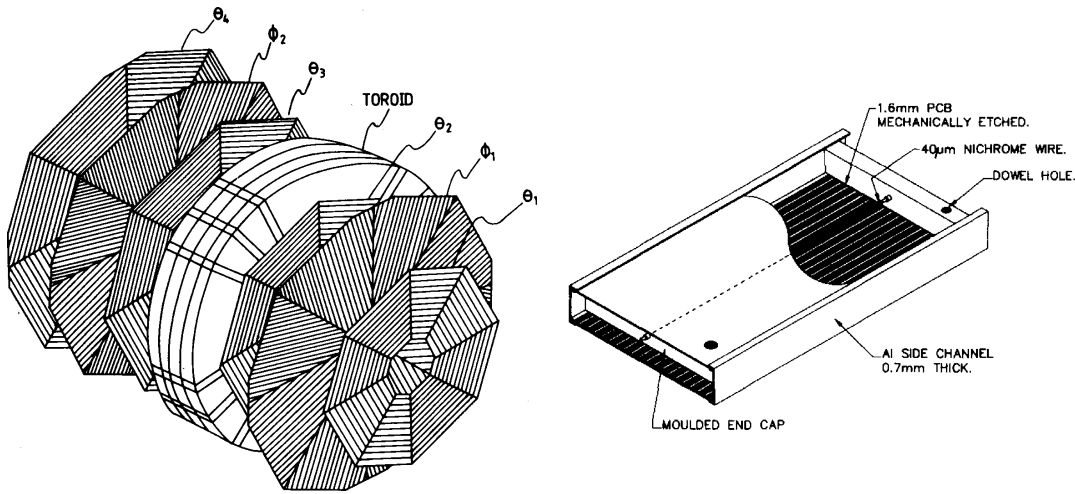


Figure 2.10: The Forward Muon Detector. The diagram to the left shows the arrangement of the toroid, the θ and ϕ layers and the arrangement of drift cells on those layers. The diagram on the right-hand side shows some details of an individual drift cell.

difference in θ between the pre-toroid and post-toroid layers to provide a momentum measurement resolution of 24 % at 5 GeV to 36 % at 200 GeV. The lower limit on this accuracy is multiple scattering in the FMD magnet before the post-toroid segment is made.

An important use for the FMD has been in detecting secondary particles from the interaction of the scattered proton with material comprising and surrounding the beam-pipe in H1. This is of use in rapidity-gap physics analysis [9] and also in this particular analysis (see chapter 6).

The FMD provides momentum measurement of muons in a range theoretically 5 GeV to 200 GeV. The lower limit is caused by material between the event vertex and the FMD, and also the requirement that the muon traverses the entire FMD in order for an accurate momentum measurement to be made. The theoretical upper limit of 200 GeV is from the field strength of the toroidal magnet. Muons with momenta approaching this value are not bent sufficiently in the field for momentum measurement to be made. Practically, uncertainties in alignment determination of the planes of detection currently limits the momentum measurement to ≤ 40 GeV.

2.2.4 Luminosity Measurement

The integrated luminosity delivered by HERA and that accepted by H1 is measured via the Bethe-Heitler process $ep \rightarrow ep\gamma$, where bremsstrahlung radiation of a photon from the beam electron occurs in the proton electromagnetic field. Small scattering angles of these electrons mean that they escape detection in the BEMC calorimeter (scattering angles $\sim \mathcal{O}\left(\frac{m_e}{E_e}\right) \simeq 19 \mu\text{rad}$ for 27.5 GeV electrons).

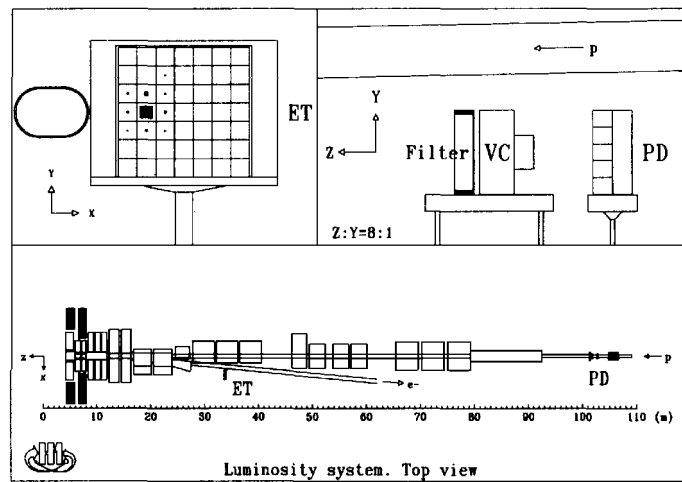


Figure 2.11: *Layout of the Luminosity System. The electron tagger and proton detector are labelled ET and PD respectively. The upper right diagram shows the lead filter and water Čerenkov calorimeter (VC). The upper left diagram shows a hit in the ET in the (x, y) plane.*

To measure this process, detectors have been installed at points along the beam pipe behind the BEMC calorimeter in order to detect the emitted photon and scattered electron, and to measure their energies. These detectors are both shown in figure 2.11 and are situated at 33.4 m (electron tagger) and 102.9 m (photon tagger) from the nominal H1 vertex. Candidates for this process are considered when coincidence is found between detected electrons and photons. These ‘overlapping’ events are sought using a random trigger selection.

The electron tagger (ET) and photon detector (PD) are both Čerenkov calorimeters⁴. Both are $22 X_0$ in length, and have square cross-sectional areas of 154×154 mm (ET) and 100×100 mm (PD). Position resolution of < 1 mm and energy resolution of $\frac{\sigma_E}{E} = \frac{10\%}{\sqrt{E}} \oplus 1\%$ have been achieved in both detectors, where E is the energy of the incident particle in GeV.

It has been necessary to install 2 metres of iron shielding behind the photon detector in order to reduce background from the incoming proton beam. Synchrotron radiation from the electron beam is reduced by the installation of a $2 X_0$ lead filter and water Čerenkov counter between the electron beam and the front of the photon detector. These additional features are also shown in figure 2.11. Only clean events where the bremsstrahlung photon does not interact with the filter are kept. Further background sources are assessed via the satellite bunches of beam leptons with no corresponding proton bunch mentioned in section 2.1. Using the well-known cross section of this process and the acceptance of the detectors, the luminosity may be measured [12].

The Proton Tagger

Although not part of the luminosity system at H1, it is worth describing here a device used to detect the other beam particle, namely the proton tagger. This is situated 24 metres from the nominal interaction point in the proton direction. It consists of 7 scintillators arranged in the (x, y) plane as shown in figure 2.12, to detect fragments of protons that have dissociated as a result of their interaction with beam electrons. This sub-detector was of great importance to this analysis for this purpose. The detector covers a rapidity range of $6 < \eta < 8$ units (see section 4.3.1 for definition of rapidity). A more detailed detector description is given elsewhere [13].

⁴Čerenkov radiation is emitted by a charged particle whose velocity is greater than the local phase velocity of light in the medium in question.

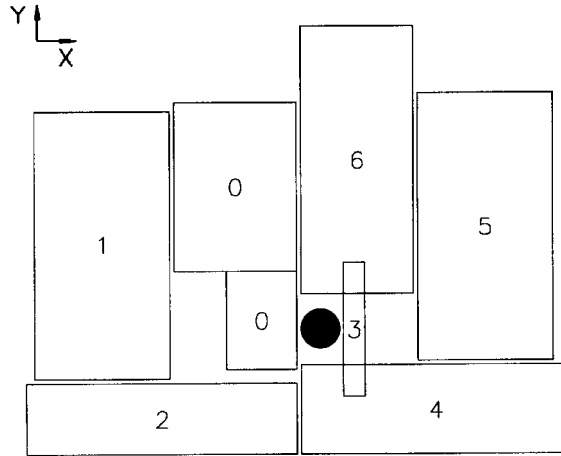


Figure 2.12: Arrangement of scintillators of the Forward Proton Spectrometer in the (x, y) plane. The position of the beam-pipe is shown by the black circle.

2.2.5 Event Triggering

Interesting physics events arising from ep interactions inside H1 are hidden within a huge number of background events. In order to identify and record these desirable events and reject the others, a complex system of triggers is required.

Bunch crossings (bc) of beams in the H1 vertex region occur every 96 ns, i.e. at a rate of 10.4 MHz. The most efficient method of analysing the resulting constant stream of information is via the ‘pipe-lined’ system chosen at H1, which reduces dead-time⁵ to a minimum. In this data acquisition (DAQ) method, 5 levels of triggers and data processing were originally proposed, labelled level 1 to level 5. Of these, only level 1, level 4 and level 5 (denoted L1, L4 and L5) were in operation for 1994 data taking. Each level analyses the output of the previous level. Levels 1 and 4 are described below, with level 5 explored later in section 4.1.

⁵The time for which the H1 detector is insensitive to ep collisions.

Level 1

The crucial first step in the H1 triggering set-up, this stage involves nine individual trigger devices such as the proportional chambers of the Central and Forward Trackers described earlier (section 2.2.1). The response of each of these devices for a certain bunch crossing are fed simultaneously into a trigger logic system which decides whether it corresponded to an acceptable event. The response of the nine trigger devices are compared with pre-defined ‘sub-triggers’ which are desirable combinations of trigger elements. Up to 128 of these combinations can be defined for differing purposes. For example, events which are candidates for cosmic rays can be very useful for calibration of sub-detectors, as can the ‘beam-halo’ events described in section 4.4. Sub-triggers used to identify these background events for detector studies are denoted ‘monitor triggers’. The combinations of trigger elements that correspond to candidates of various physics processes are of course also allowed to pass through to the next trigger level.

If L1 accepts the event, it sends out a signal to keep the event data of that bunch-crossing, and freezes the entire H1 detector while this information is passed to the next level. The detector is dead during this time, which lasts ~ 1 ms. As the level 1 decision on a bunch crossing is made 24 bunch-crossings after it occurred, it can be seen that a pipelined operation is preferable to stopping the detector for 24 bunch-crossings for each processed, whether it results in an acceptable event or not. It is however necessary in the pipe-lined method to keep a buffer containing information on 24 bunch crossings at any one time. During 1994 level 1 operated at a mean of 20 Hz, with a data rate of 1.2 MBs^{-1} .

Level 4

The level 4 ‘filter farm’ takes the information passed to it from level 1 and performs further event reconstruction as necessary. For instance, for an event accepted at level 1 as a possible muon candidate, level 4 will run detailed reconstruction code of the iron chambers (ITREC) to provide further information on the

quality of the muon candidate. The event will be rejected at this level if certain criteria are not met.

Level 4 aims to reject beam-gas and beam-wall (see section 4.4) events occurring inside the detector, and also those accepted at level 1 due to trigger noise. Level 1 monitor triggers were automatically accepted at L4 for 1994 positron running. On average, around 30 % of all physics triggers at level 1 were kept by level 4. The output from this level was at a rate of 5-10 Hz with a data rate of $\approx 1 \text{ MBs}^{-1}$.

Events accepted at level 4 then undergo full reconstruction by the program H1REC. Their next stage then is to go through the level 5 classification scheme described in section 4.1. For completeness it is mentioned here that level 5 ran at $\lesssim 5 \text{ Hz}$ with a data rate of around 0.3 MBs^{-1} during 1994 positron running.

Chapter 3

Photoproduction at H1

Photoproduction processes account for the majority of events seen at HERA and therefore provide most of the total ep cross section. The electron¹ beam provides an intense source of almost real photons which can then interact with the proton. The momentum transfer from the beam electron to the photon is generally low for such events. Various models exist to describe the interaction of the photon with the proton. This chapter examines some of these models, and gives an introduction to photoproduction physics at HERA as far as they relate to this particular analysis.

3.1 Kinematics of Photoproduction

A basic photoproduction diagram is shown in figure 3.1 which can be considered as two separate vertices, $e \rightarrow e + \gamma^*$ and $\gamma^* + p \rightarrow X$, where γ^* is the virtual photon. The final state of the proton is denoted by X in this diagram, which may break up from its interaction with the virtual photon. The $e\gamma^*e$ vertex shown in figure 3.1 can be described by the standard kinematic variables of deep inelastic scattering defined by equations 3.1.

¹When the electron beam is referred to it should be understood that this applies equally to a beam of positrons.

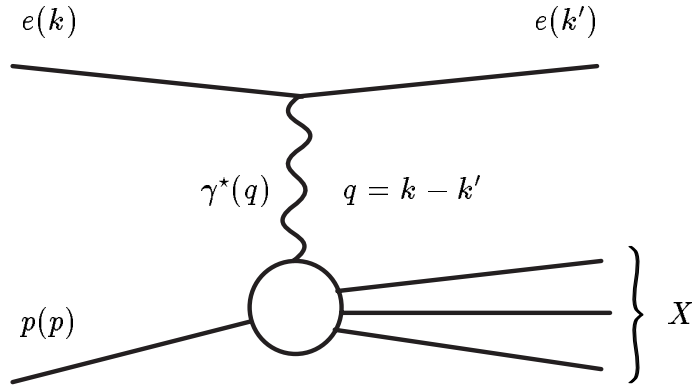


Figure 3.1: Basic diagram of ep scattering via photoproduction. The 4-vectors of the electron, virtual photon and proton are labelled k , q and p respectively.

$$s_{ep} = (p + k)^2; \quad Q^2 = -(k - k')^2 = -q^2; \quad y = \frac{p \cdot q}{p \cdot k}. \quad (3.1)$$

These variables have the following meanings:

- s_{ep} is the centre of mass energy squared of the ep system. For the beam energies at HERA in 1994 (see table 2.1) we have $\sqrt{s_{ep}} = 300$ GeV.
- Q^2 is the four momentum transfer squared of the photon between the electron and proton, and is a measure of the virtuality of the photon. For photoproduction this value is typically a very small fraction of a GeV^2 , though it is usually defined as $Q^2 < 1 \text{ GeV}^2$. For non-photoproduction events, this may extend to values of $Q^2 \leq s_{ep} \sim 10^5 \text{ GeV}^2$, with this regime corresponding to deep inelastic scattering (DIS) of the electron and proton.
- y is the fractional energy loss of the electron in the proton rest frame, from its photon emission. This scaling variable has a value between 0 and 1 and is known as the inelasticity parameter. For elastic events the variable y tends to be small, whereas $y \rightarrow 1$ for inelastic events.

We can also define kinematic variables relating to the γp vertex as shown in equations 3.2,

$$x = \frac{Q^2}{2p \cdot q}; \quad s_{\gamma p} = W_{\gamma p}^2 = (p + q)^2. \quad (3.2)$$

These variables are described below:

- x is the fraction of the proton momentum carried by the parton struck by the quasi-real photon. It is also known as the Bjorken scaling variable.
- $s_{\gamma p}$ is the centre of mass energy squared of the γp system.

The scaling variables x and y can be related to the photon virtuality and the ep centre of mass energy through equation 3.3,

$$Q^2 = xys_{ep} \approx 4xyE_eE_p, \quad (3.3)$$

where E_e and E_p are the electron and proton beam energies and s_{ep} is the total centre-of-mass energy of the ep system. The practical reconstruction of these kinematics is explored in section 4.3.

3.2 The J/ψ Meson

The bound states $c\bar{c}$ known as charmonium were discovered almost simultaneously by experiments at both the Stanford Linear Accelerator Center (SLAC) [14] and the Brookhaven National Laboratory (BNL) [15] in 1974. Stanford denoted their discovery at around 3.1 GeV the ψ particle, while the similar find at Brookhaven was called the J particle. The discovery was shared, as was the resulting 1976 Nobel Prize in physics, with the particle now denoted the J/ψ . The particle was detected by its decay into electron pairs in both experiments, from e^+e^- collisions at SLAC using the SPEAR accelerator, and in p Be collisions at Brookhaven.

This discovery sparked a wave of creative turmoil in particle physics, with this evidence of a $c\bar{c}$ bound state causing huge interest in charm physics in particular,

including work at the e^+e^- collider DORIS at DESY. The entire series of states of the $c\bar{c}$ system were soon found, and termed ‘charmonium’. The quark-antiquark states are said to be a ‘hidden flavour’ system, since the net charm of the system equals zero. The energy levels of this system were found to be in very close agreement with theoretical predictions and provided strong evidence for the quark model. It is implied by the mass of these meson states that the charm quark has a higher mass than the (u, d, s) quarks, of $m_c \approx m_{J/\psi}/2 \approx 1.5$ GeV.

<i>Bound State</i>	<i>Mass (MeV)</i>	<i>Decay Modes</i>	<i>Branching Ratio (%)</i>
J/ψ or $\psi(3097)$	3096.88 ± 0.04	Hadrons	86.0 ± 2.0
		mainly $(2n+1)\pi$	
		e^+e^-	5.99 ± 0.25
		$\mu^+\mu^-$	5.97 ± 0.25

Table 3.1: *Currently accepted properties of the J/ψ charmonium state, including some principle decay modes and their branching ratios.*

Some decay modes for the J/ψ are shown in table 3.1 together with some currently accepted properties [16]. The charmonium level above the J/ψ is denoted ψ' , with an energy of 3.69 GeV. The ψ' level can decay to a J/ψ plus hadrons and also to e^+e^- and $\mu^+\mu^-$ pairs and thus contributes background to a J/ψ signal. This idea is discussed in section 6.1. It should also be noted that the J/ψ can only decay into the lepton pairs e^+e^- and $\mu^+\mu^-$, or hadronic states containing only the lighter (u, d, s) quarks. States containing single (open) charm, for instance the D vector meson states D^+ ($c\bar{d}$) and D^0 ($u\bar{c}$), have masses higher² than $m_{J/\psi}/2$. Therefore, decays such as $J/\psi \rightarrow D^0\bar{D}^0$ are allowed by all conservation laws except that of energy. It is for this reason that the J/ψ has a comparatively long lifetime when compared with other vector mesons.

²The masses of the D^0 and D^+ mesons are 1865 MeV and 1869 MeV respectively.

3.3 Elasticity and Momentum Transfer

A schematic diagram of elastic J/ψ production is shown in the upper diagram of figure 3.2, with the incoming electron interacting with the proton, and the proton remaining intact. Unfortunately there is a major source of background from the process shown in the lower diagram of figure 3.2. In this case the interaction between the electron and proton causes dissociation of the proton which may remain undetected. Many of these events can be identified by the introduction of another kinematic variable, z , defined in equation 3.4,

$$z = \frac{p \cdot p_{J/\psi}}{p \cdot q}, \quad (3.4)$$

where $p_{J/\psi}$ is the J/ψ momentum and other 4-vectors are as defined in figure 3.1. This is an indication of the elasticity of the $J/\psi p$ vertex. It is a measure of the photon energy given to the J/ψ emitted from the vertex, and in the proton rest frame $z = \frac{E_{J/\psi}}{E_\gamma}$. The closer this value is to unity, the smaller the hadronic system accompanying the J/ψ and hence the more elastic the event. The squared four-momentum transfer between the incoming proton and J/ψ is given by the variable t defined in equation 3.5. Elastic and diffractive J/ψ production processes tend to have small values of t , while events where the proton dissociates tend to have higher t values.

$$t = (p - p')^2 = (q - p_{J/\psi})^2 \quad (3.5)$$

3.4 Diffractive J/ψ Production Mechanisms

Now we shall examine more closely the $\gamma^* + p \rightarrow X$ vertex of figure 3.1 more closely. The virtual photon can itself collide directly with constituents of the proton, a rare process, or it can interact via some colourless, chargeless exchange in which quantum numbers are conserved. This latter notion is known as a *diffractive*

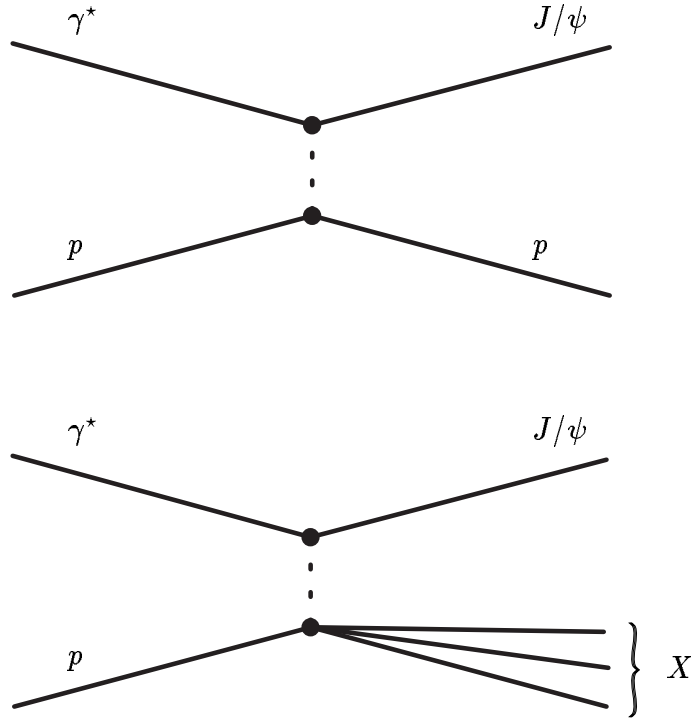


Figure 3.2: *Elastic (upper diagram) and dissociative (lower) J/ψ production.*

interaction, whose mediator is known as the pomeron, \mathbb{P} . The pomeron has been with us for over 20 years and has not yet been fully understood. It is thought that the higher energies available at HERA may further our understanding of diffractive processes.

As mentioned already, the t -channel momentum transfer between proton and J/ψ is typically small ($\lesssim 1 \text{ GeV}^2$) for diffractive events. No theory inspired by QCD perturbation theory has yet been devised which has successfully described previous data for this range of t values. It has also not been possible to make reliable perturbative calculations at a scale $Q^2 \lesssim 1 \text{ GeV}^2$. Instead, non-perturbative phenomenological models have been devised to describe data at this energy scale. One such model is the idea of Vector Meson Dominance described in section 3.4.1. An example of a QCD-inspired production mechanism is given in section 3.4.3.

3.4.1 Vector Meson Dominance

In this model the virtual photon is said to fluctuate into a virtual quark-antiquark bound state which then interacts with the proton. It is this idea, known as Vector Meson Dominance (VMD) [17] which allows the photon to be treated as a source of quarks and gluons. The γp vertex then begins to appear similar to a $J/\psi p$ vertex and we can treat the process as hadron-hadron scattering. This model describes well results quoted by previous experiments at lower γp energy to that attainable at HERA [18][19][20].

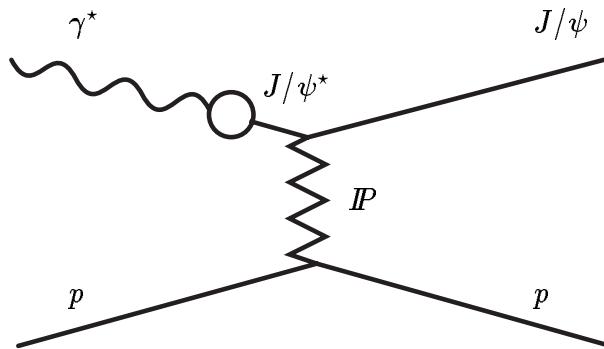


Figure 3.3: *Diffractive elastic J/ψ production via soft pomeron exchange.*

Figure 3.3 shows a diagram of this mechanism. The pomeron in this model is the ‘soft’ pomeron proposed by Donnachie and Landshoff [21], which couples to single quarks in the proton and J/ψ like an isoscalar $C=+1$ photon. It may possibly be the exchange of two non-perturbative gluons, or glueball exchange [22].

The behaviour of the production cross section predicted by this model is given by equations 3.6,

$$\begin{aligned} \frac{d\sigma_{el}}{dt} &\propto e^{-bt} \\ \sigma &\propto W_{\gamma p}^{4\epsilon} \end{aligned} \quad (3.6)$$

where the experimental value of the parameter b has been measured [23] as ($b = 4.7 \pm 1.9$) GeV^{-2} at $|t| < 0.75 \text{ GeV}^2$ and a mean photoproduction energy of $\langle W_{\gamma p} \rangle = 90 \text{ GeV}$. This slope parameter is a function of $W_{\gamma p}$, and in the VMD model follows the relation $b = b_0 + 4\alpha'_{\mathcal{P}} \ln\left(\frac{W_{\gamma p}}{W_0}\right)$, where $\alpha'_{\mathcal{P}} = 0.25 \text{ GeV}^{-2}$ for a soft \mathcal{P} . The constant b_0 enables normalisation to previous results measured at W_0 , such as those shown in table 3.2. In the model of the soft pomeron the value of the parameter ϵ in the lower of equations 3.6 is $\epsilon = 0.0808$.

3.4.2 Monte Carlo Generator

The Monte Carlo simulation files used for this analysis were generated using the DIFFVM program, a generator of diffractive processes in ep collisions based on Vector Meson Dominance. The processes modelled corresponded to diffractive elastic J/ψ production, with subsequent decay to a di-muon pair. The case where the proton dissociates was also modelled. Details of the generator values used are given in table 3.2. The various stages necessary to produce full detector simulation of H1 events from this generator are described in section 5.2. These Monte Carlo files were those used for all results presented in chapters 4 and 5 of this thesis.

<i>Generated Value</i>		<i>Elastic</i>	<i>Dissociative</i>
Integrated Luminosity	(pb^{-1})	60	20
Parameter ϵ		0.0808	0.0808
Slope Parameter b	(GeV^{-2})	5.00	2.50
Branching Ratio to $\mu^+\mu^-$	(%)	5.98	5.98

Table 3.2: *Generator values used in the production of the Monte Carlo files for elastic and proton-dissociative diffractive J/ψ production. The slope parameters are given at $W_{\gamma p} = 14 \text{ GeV}$.*

It was necessary to normalise these files to results of previous experiments. The elastic files having a b parameter normalised to $b = (5.0 \pm 2.0) \text{ GeV}^{-2}$ at $\langle W_{\gamma p} \rangle = 14 \text{ GeV}$ from results of the E516 experiment [18], while the files containing proton dissociation were normalised to the NA14 result [24] of $b = (2.5 \pm 0.2) \text{ GeV}^{-2}$

also at $\langle W_{\gamma p} \rangle = 14 \text{ GeV}$. The slope parameter b governs the exponential fall of the differential cross section $\frac{d\sigma_{el}}{dt}$ with increasing t , as shown in equation 3.6. A cut was done on the γp centre-of-mass energy $W_{\gamma p} > 20 \text{ GeV}$ and no cuts were made on the scattered positron.

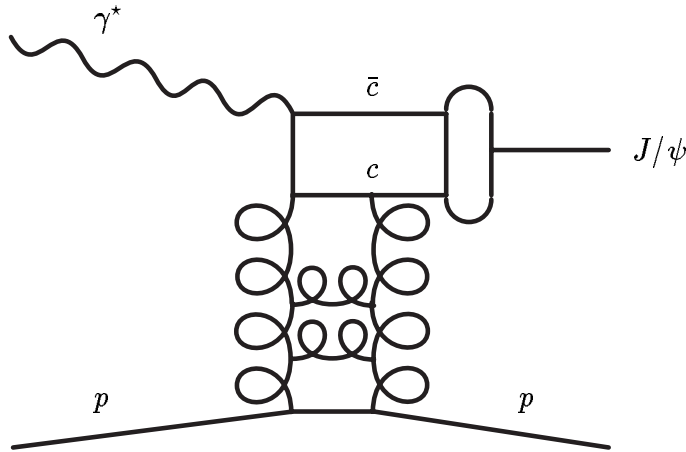


Figure 3.4: QCD-inspired gluon ladder model of the hard pomeron.

3.4.3 QCD Inspired Models

This time, pomeron exchange is the result of a hard subprocess in which the photon scatters from a gluon in the pomeron, $\gamma \mathbb{P} \rightarrow \gamma g_{\mathbb{P}} X_{\mathbb{P}} \rightarrow c\bar{c} X_{\mathbb{P}} \rightarrow J/\psi$, where $X_{\mathbb{P}}$ is the pomeron remnant. In the simplest case this remnant is a gluon which, together with the $c\bar{c}$ pair, forms a J/ψ . The mechanism by which this might occur is described in the LUND program [25]. This program considers that it is possible for the $c\bar{c}g$ state to collapse into a single particle, i.e. the J/ψ , if the invariant mass of the $c\bar{c}$ system is insufficient to produce two particles, for instance pair production of D mesons ($m_{c\bar{c}} < 2m_D$). Recently (1993) work has been done to explain the pomeron in terms of a QCD gluon ladder [26] as shown in figure 3.4.

In QCD inspired models the elastic cross section is said to be proportional to the square of the gluon momentum density in the proton $g(x)$, as shown in equation 3.7,

$$\sigma_{\gamma p} \sim [x g(x)]^2 \quad (3.7)$$

where x is the kinematic variable defined in equation 3.2 of this chapter. Using the approximation for x shown in equation 3.8 we may study x at values of $x \sim 10^{-3}$ for a mean energy of $\langle W_{\gamma p} \rangle \approx 90$ GeV.

$$x \simeq \frac{m_{J/\psi}^2}{W_{\gamma p}^2} \quad (3.8)$$

3.4.4 The Pomeron

In both the soft (VMD) and hard (QCD) models of the \mathbb{P} we have seen we refer to the exchange of a current with the vacuum quantum numbers. In neither model is the pomeron considered to be a single elementary particle, though as we have seen, it may have particles associated with it. It is not clear at the moment whether these soft and hard models should be treated as entirely separate, or whether they mix with one another, possibly as Q^2 increases. Attempts to provide models by which they might combine have not been very successful as yet [22] and such theories require help from data.

Chapter 4

Event Selection

In section 2.2.5 the ‘filter farm’ cuts applied to events found by the level 1 trigger were described. Events passed by level 4 as analysis events then proceed to level 5, where they are classified according to which analyses they may be useful to, whereas those which are not of physics interest are rejected. Each event may be classed as being of interest to several different physics analysis working groups. This procedure in effect breaks up the entire (very large) set of data into smaller sections. Events passed by level 5 are written to data set tape (DST) for analysis purposes.

The level 5 class of interest to our $J/\psi \rightarrow \mu^+ \mu^-$ analysis was denoted class ECMUON. This contained events that at a first look were candidates for either J/ψ decay to muons, or inclusive muon events¹ characteristic of D^* decay. Events of this muon class therefore provided the starting point for our analysis.

4.1 Level 5 Muon Classification

The cuts of the level 5 classification code follow. In these cuts we make reference to ‘inner’ and ‘outer’ tracks, the former being charged tracks reconstructed in either the central and/or forward tracking detectors, while the latter refer to tracks

¹The charm quark decay $c \rightarrow \mu \nu_\mu s$.

left in the various outer muon detectors. Inner tracks were only used if they could be fitted to a common vertex on the z axis within 40 cm of the H1 nominal vertex, and if they also passed certain criteria outlined in table 4.1.

Inner Tracks

The cuts shown in table 4.1 on inner tracks were designed to ensure a sample of events in which tracks originated from a point close to the nominal interaction point, and that the tracks were of sufficient quality to provide reasonable momentum measurement for analysis. By combined tracks we refer to the case where hits are found in both the central and forward trackers which may be fitted by a single track.

In table 4.1, p_t is the transverse momentum of the track, z_0 the position of its extrapolated vertex and dca is the radial distance of closest approach to the z axis. The chi-square of the vertex fit is denoted χ_{vertex}^2 , while χ_{track}^2 is that of the forward or combined track fit. The starting radius of a central track in the CJC drift chambers is labelled r_{start} , while r_{length} is the radial length of this CJC track. The total number of space-point measurements used in reconstructing a track is denoted n_{hit} , for any of central, forward or combined tracks. For forward tracks this cut was on hits in the planar chambers only. Note that in photoproduction the incoming electron and the photon it radiates are virtually parallel, so the transverse momentum of any particle in an event is measured with respect to the incoming electron direction, i.e. the beam axis.

Outer Tracks

We then look at the possibility that good inner tracks can be linked to outer tracks in the muon detectors. Outer background tracks are also seen in these detectors so the following quality cuts must be made on muon identification, and only those outer tracks linked to quality inner tracks were used.

<i>Parameter</i>		<i>Central</i>	<i>Combined</i>	<i>Forward</i>
p_t	(GeV)	≥ 0.2	≥ 0.2	≥ 0.2
$ \text{dca} $	(cm)	≤ 2	≤ 2	≤ 2
$ z_0 $	(cm)	< 40	< 50	< 50
χ_{vertex}^2		< 20	< 20	< 20
χ_{track}^2		-	< 10	-
r_{start}	(cm)	< 30	-	-
r_{length}	(cm)	> 15	-	-
n_{hit}		≥ 10	≥ 12	≥ 12

Table 4.1: Inner track cuts performed by the 1994 level 5 classification code for event class ECMUON.

In table 4.2 the cuts on the parameters ρ_x and ρ_y are a test of the compatibility of the iron track with the nominal vertex in the x and y dimensions, while the z_0 cut tests the vertex given by the muon track in the z dimension. The parameter $\Delta\phi$ measures the difference in the ϕ angle between pre-toroid and post-toroid layers of the FMD. In addition to these quality cuts, the inner track to which they were linked had to have a momentum measured as greater than 0.8 GeV and below 20 GeV. Muon links were also sought in the calorimeters at level 5 (though not at level 4), with the quality of the link between an inner track to an electromagnetic cluster in the main LAr calorimeter being given by a quality index 1 (poor quality), 2 (medium) and 3 (good). A muon leaves a typical track in the calorimeter, a penetrating track with small and localised energy deposits. Only those links of quality 2 or 3 were considered sufficient by level 5 to class as a muon candidate. Figure 4.1 shows examples of J/ψ candidates where muons have been identified in the LAr calorimeter.

However, not every event containing an identified muon was classed as ECMUON, in which was kept only the following five listed combinations of identified particles:

<i>Parameter</i>		<i>FEC</i>	<i>Barrel</i>	<i>BEC</i>	<i>FMD</i>
ρ_x	(cm)	≤ 100	≤ 100	≤ 100	-
ρ_y	(cm)	≤ 100	≤ 100	≤ 100	-
z_0	(cm)	-	≤ 100	-	+300 -400
1st Layer		≤ 5	≤ 5	≤ 8	-
Number of Layers		≥ 6	≥ 2	≥ 3	≥ 4
Probability	(%)	≥ 0.1	≥ 0.1	≥ 0.1	≥ 0.1
χ_{track}^2		-	-	-	≤ 20
$\Delta\phi$	(rad)	-	-	-	≤ 1

Table 4.2: 1994 ECMUON cuts on muon tracks and links to inner tracks shown for the forward and backward endcaps (FEC and BEC), barrel region and Forward Muon Detector (FMD).

- One muon in Iron or Forward Muon Detector chambers.
- Two or more muons (chambers or calorimeter).
- One muon (chambers or calorimeter) with ≤ 5 inner tracks.
- One muon (chambers or calorimeter) and one electron candidate.
- Exactly two inner tracks with one identified lepton (e, μ).

As mentioned earlier, these combinations were designed to identify either the decay $J/\psi \rightarrow \mu\mu X$, or events with open charm with final states $\mu, \mu\mu, \mu e, e$. They are also necessary to keep the data sample of class ECMUON at an acceptable size. Rare exotic decays were also included in this class, candidates for which are where muons or electrons are found with very high transverse momentum.

4.2 User Data Selection

With the intention of producing a sample from which the cross section of the elastic decay $J/\psi \rightarrow \mu^+\mu^-$ may be measured, a user selection was made from the

ECMUON data. In selecting elastic candidates, a trade-off was necessary between making the cuts too severe and losing potential candidates, or making the cuts too loose causing high running times of further analysis code and highlighting hardware limitations of disk space. It was found that the most crucial cut in this respect was on the track multiplicity of the event². Elastic events were expected to contain low numbers of tracks, ideally two good vertex constrained tracks, both linked to muon tracks or clusters.

Therefore, in making the selection only ECMUON events containing < 20 vertex constrained tracks were analysed, and if this number was still above 6 after quality cuts on the inner tracks, then the event was rejected. Furthermore, only if the event contained ≥ 2 muon candidates was it kept in our data selection. The cuts on inner tracks and muon quality at this stage were the same as those given in tables 4.1 and 4.2, with the additional condition that forward tracks contain hits in the planar chambers of at least two supermodules for reasonable momentum measurement. Forward tracks with hits in planar chambers of only one supermodule were however kept if hits in at least one of the radial chambers were used in the track fit. No cut on track angle was done in making our sample, with all inner tracks considered whether they be central, combined or forward tracks.

Note that the user selection outlined above contained not only elastic events, but also events from other processes (mainly photoproduction with some degree of proton dissociation), but biased towards low multiplicity. It provided a convenient sample of data to work with.

4.3 Reconstructing Event Kinematics

To proceed further in identifying elastic events it is necessary to analyse the event kinematics in more detail. Our low multiplicity data sample was analysed and di-muon pairs sought using the same definitions of good tracks and muon candidates defined in tables 4.1 and 4.2. In section 3.1 and 3.2 we explained the kinematics of the

²The total number of inner tracks in the event.

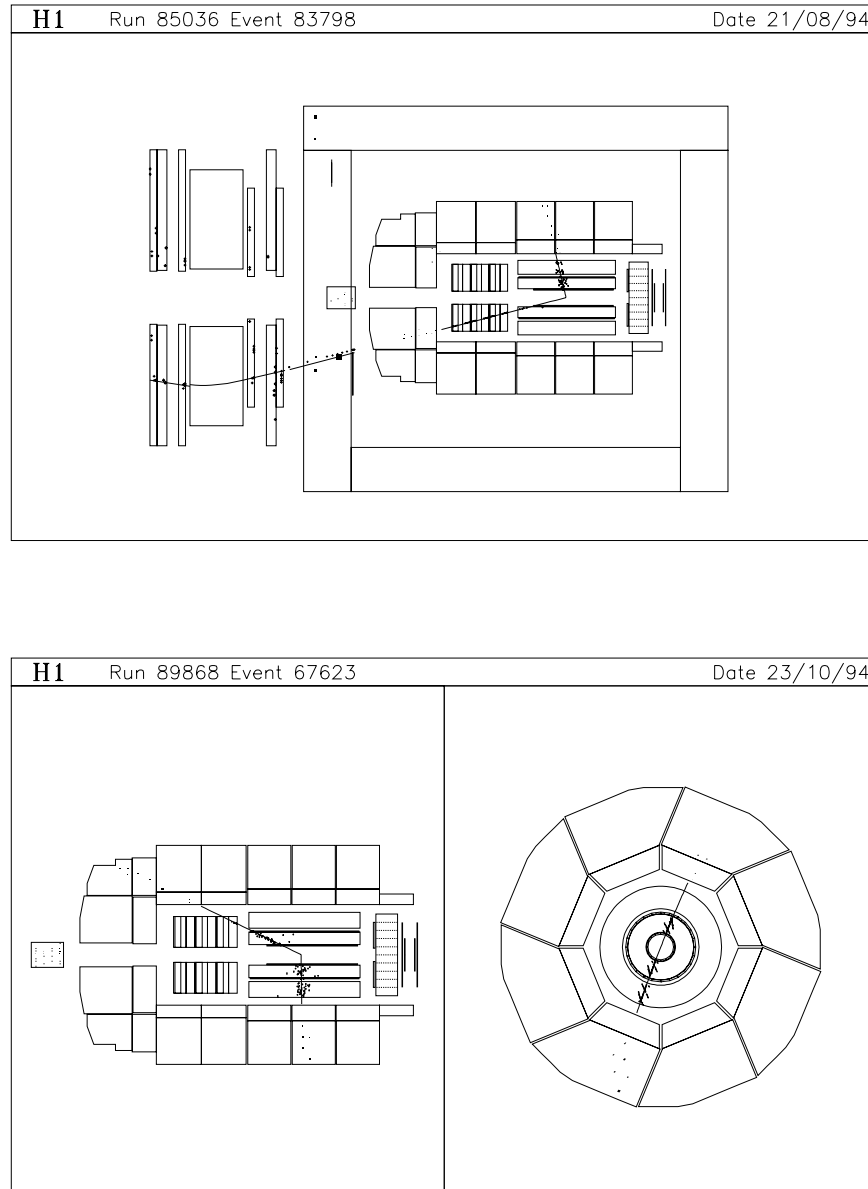


Figure 4.1: Elastic J/ψ decays as recorded in 1994 H1 data. The upper diagram shows a two-muon final state with one muon being detected in the Forward Muon Detector. The lower diagram shows a J/ψ decay in both side and radial views, where both muons are detected in the LAr calorimeter. The lower diagram also shows an example of a combined central/forward track.

electron and proton vertices. In the events we are considering, the scattered electron is not detected in the main body of the detector, i.e. the BEMC or LAr calorimeters. It can be detected in the electron tagger (see chapter 2) which provides us with a position and energy measurement from which we may calculate event kinematics directly and very accurately. However, if we insist on this condition we drastically decrease the size of our sample, due in part to the low acceptance of this tagging detector. Using e -tagged events would also bias the kinematics of the sample we choose, as we would be effectively restraining the variable $Q^2 < 0.01 \text{ GeV}^2$. The range of the variable y would also be restricted, the lower threshold being so high that a J/ψ produced in an e -tagged event would almost certainly be too far in the backward region to detect. Hence by not following this procedure, we have no direct knowledge of the properties of the scattered electron. To calculate variables such as the fractional energy loss of the electron y , and the four momentum transfer Q^2 , we must therefore use the method proposed by Jaquet and Blondel [27]. This method uses variables that may be measured in the main body of the detector to reconstruct the kinematics via equations 4.1 and 4.2,

$$y_{jb} = \sum_{i=1}^n \frac{E_i - p_{z,i}}{2E_e} \quad (4.1)$$

$$Q^2 = \sum_{i=1}^n \frac{p_{x,i} + p_{y,i}}{1 - y_{jb}} \quad (4.2)$$

where E_i and $p_{z,i}$ are the energy and longitudinal momentum of individual inner tracks and calorimeter cells in the laboratory frame of reference, over which the sum is made for each event. These momenta in the x and y dimensions are labelled $p_{x,i}$ and $p_{y,i}$; E_e is the energy of the incoming electron beam (27.5 GeV). Of course by insisting that the electron is not scattered by sufficient angle to be detected by H1, we are in effect imposing a kinematic cut on events of $Q^2 \leq 4 \text{ GeV}^2$. Events containing candidates for the scattered electron in the BEMC or LAr were rejected.

Once y has been reconstructed accurately, we are able to measure all of the other kinematic variables listed in section 3.1. For instance the elasticity variable z from equation 3.4 can be reconstructed using relation 4.3,

$$z = \frac{E_\psi - p_{z,\psi}}{2E_e y_{jb}} \quad (4.3)$$

where E_ψ and $p_{z,\psi}$ are the energy and longitudinal momentum of the J/ψ particle, whose measurement is studied in section 4.3.1.

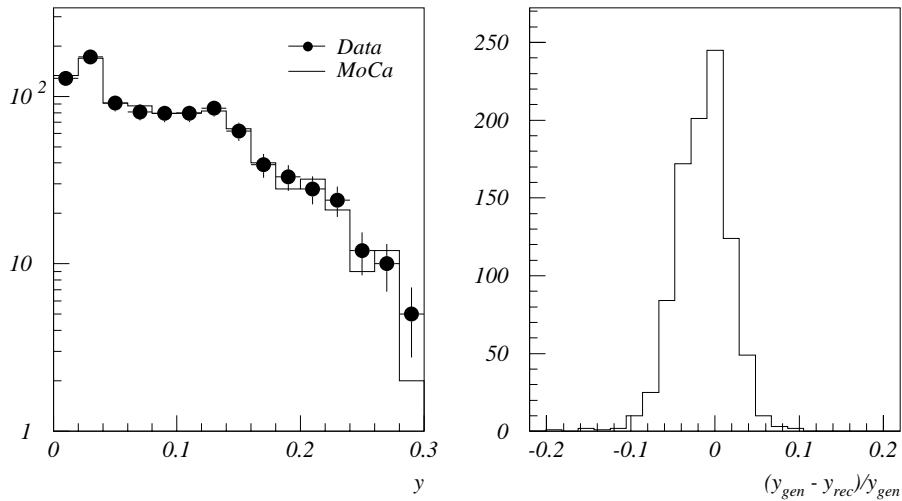


Figure 4.2: The diagram to the left shows a comparison of generated (solid histogram) and reconstructed values (points) of the kinematic variable y for simulation of the elastic decay $J/\psi \rightarrow \mu^+ \mu^-$. The diagram to the right shows the distribution of the fractional difference between generated and reconstructed values.

Figure 4.2 shows comparison of the reconstructed values of y with those calculated from the generated values for Monte Carlo simulation of the elastic process $J/\psi \rightarrow \mu^+ \mu^-$. Figure 4.3 shows the generated and reconstructed values of the z variable using the formulae outlined in equations 4.1 and 4.3 and the reconstructed value of y , again for elastic Monte Carlo. Note the smearing effect in our recon-

structured value of z , representing the best accuracy available to us. The generated z distribution resembles a delta function at $z = 1$, while the reconstructed values are smeared over a range of $0.95 \rightarrow 1.05$. Hence in order to ensure that we keep all elastic events, the tightest cut we can make on the elasticity variable in our data sample is $|z - 1| < 0.05$. The reason why the generated z distribution is not a delta function is due to mass corrections. These come from the formula $z = \frac{W_{\gamma p}^2 - M_X^2 + t}{W_{\gamma p}^2 - m_p^2} \approx 1 - \frac{M_X^2}{W_{\gamma p}^2}$ with M_X the invariant mass of the proton final state, and m_p the proton mass. For elastic production, $m_p = M_X \ll W_{\gamma p}$, hence only a small deviation of generated z from unity occurs.

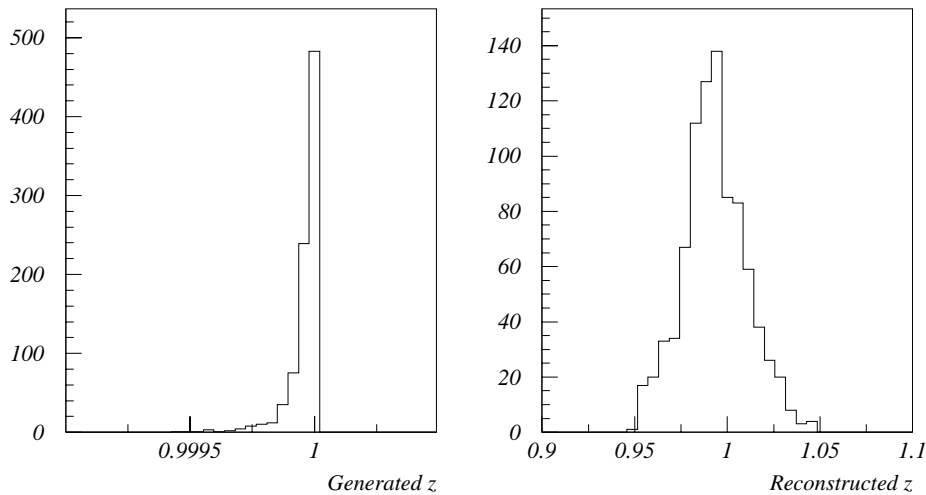


Figure 4.3: Comparison of generated (left hand diagram) and reconstructed (right hand) values of variable z . Elastic diffractive Monte Carlo was used, corresponding to the decay $J/\psi \rightarrow \mu^+ \mu^-$.

This relatively loose cut at $|z - 1| < 0.05$ means that not all events from other processes present in our low multiplicity data sample are removed. This is especially true of events containing proton dissociation whose z values range from around $0.9 \rightarrow 1$. This idea is discussed in more detail in chapter 6. Note also that with the elasticity variable at this high value, there should be very little activity

accompanying the di-muon pair, so it is not necessary to make an explicit cut on the number of inner tracks in the event totalling exactly two.

4.3.1 J/ψ Kinematics

The numerator of equation 4.3 shows that for practical reconstruction of the z variable, it is necessary to first reconstruct the energy and longitudinal momentum of the J/ψ particle. As we detect the entire final state of the J/ψ , we can readily reconstruct variables such as these from the measured properties of the two detected muons. Some examples of generated and reconstructed values of J/ψ properties are shown in figure 4.4 for simulation of the elastic process $J/\psi \rightarrow \mu^+ \mu^-$. In all of these plots, the solid lines show the generated values, while the points show the reconstructed values. The distributions show how accurately J/ψ energy E , transverse momentum p_t , and the angles θ and ϕ of the J/ψ path can be reconstructed.

Another useful parameter we can measure is pseudo-rapidity η , defined in equation 4.4. It is a unit often used to describe the longitudinal momentum distribution of particles since its Lorentz transformation properties are straightforward. We can calculate η for the J/ψ particle from the momenta of the individual muons it decays into, with distributions of generated and reconstructed values shown in figure 4.5.

$$\eta = -\ln \tan \left(\frac{\theta}{2} \right) \quad (4.4)$$

4.4 Muon Background Removal

There are several potential sources of muon background at HERA. For example a source of oppositely charged muon pairs is the process $\gamma\gamma \rightarrow \mu^+ \mu^-$ in the high intensity photon flux from the electron beam. However, as muons produced in

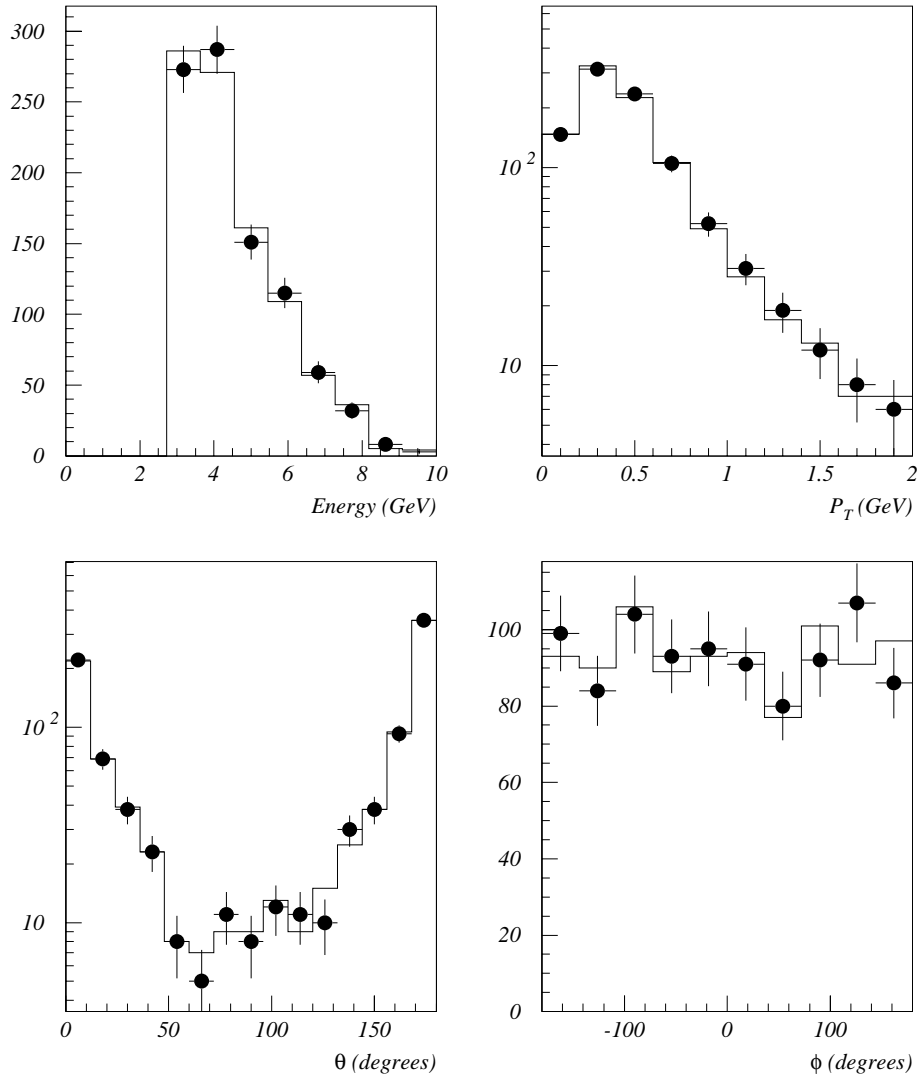


Figure 4.4: Comparison of generated (solid histogram) and reconstructed (points) values of J/ψ energy, transverse momentum (P_T), θ angle and ϕ angle from simulation of the decay $J/\psi \rightarrow \mu^+ \mu^-$.

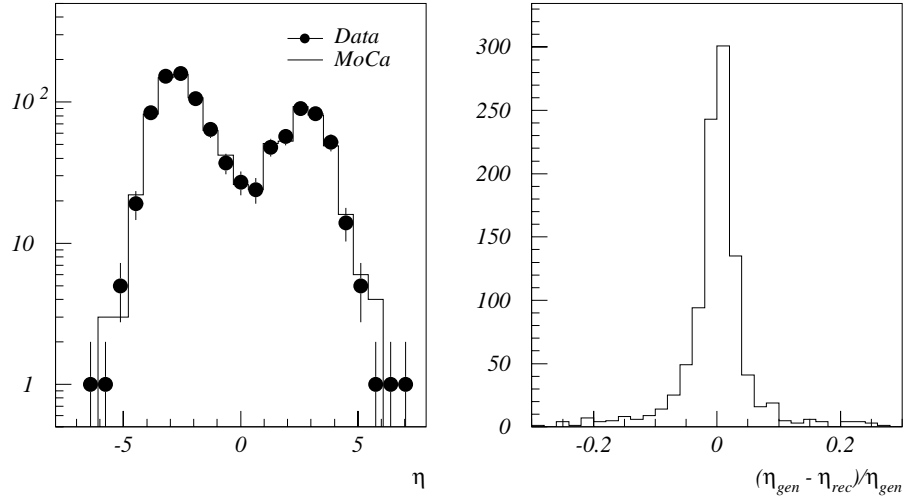


Figure 4.5: The left-hand diagram shows a comparison of generated (solid histogram) and reconstructed (points) values of the J/ψ pseudo-rapidity for simulation of the elastic decay $J/\psi \rightarrow \mu^+ \mu^-$. The fractional difference between generated and reconstructed values is shown in the diagram to the right.

this way normally possess low transverse and total momentum, the actual fraction that are detected is low. These muons are denoted physics muons as they are produced from interactions of beam particles. In addition to these, other sources of muons exist which are not produced in this way, and are described in the following sections.

Beam Halo and Cosmic Muons

When the proton beam is accelerated around the storage ring, it is possible that protons interact with the wall of the beam pipe and produce high energy muons in the proton direction. These muons follow the proton beam and normally penetrate the entire detector. Events containing these ‘beam halo’ muons are sought by a special trigger and are hence easily removed.

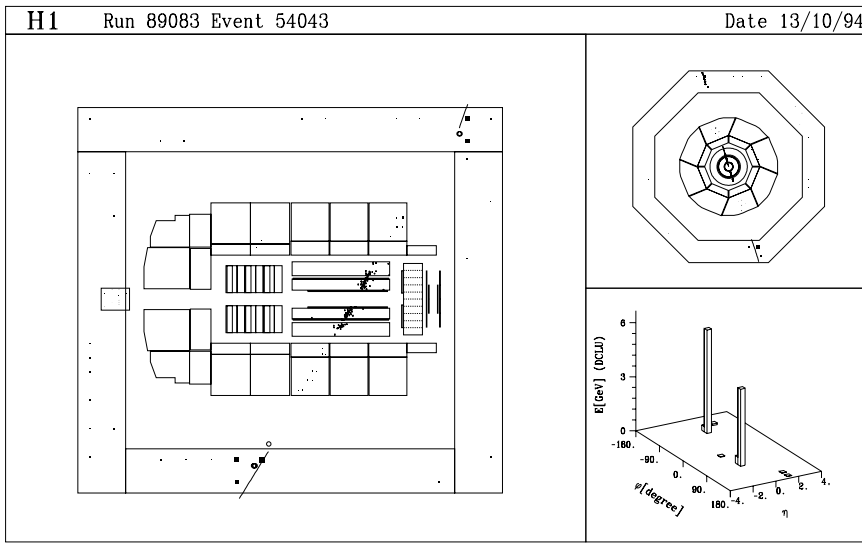


Figure 4.6: Cosmic Event in 1994 data. The event is shown from side (main figure) and radial (upper right) views. The track kinematics are shown in the lower right figure in an Energy- η - ϕ distribution.

Cosmic muons are another major source of background and are also removed from analysis data by a suitable trigger. However, cosmic events that traverse the H1 detector close to the nominal interaction point can pass the L4 trigger decision and are removed at a later stage using timing information from the calorimeters. Figure 4.6 shows one such event found in our data sample. Both cosmic and beam halo muons are however very useful for Forward Muon Detector tests, with the one disadvantage that they are of very high energy when compared with physics muons in general. This means they are not bent by a great amount in the magnetic field of the forward toroid, and so provide no opportunity for studies of momentum measurements to be made.

Beam-gas events are those where the proton interacts with residual gas in the beam pipe, producing muons. This can occur within the detector close to the nominal interaction point, leading to these muons being confused with physics muons. These are removed at level 4 by the cut shown in equation 4.5,

$$\sum p(1 - \cos(\theta)) > 1.5 \text{ GeV} \quad (4.5)$$

where the sum is made over inner tracks in the region of the nominal H1 vertex. The measured parameter corresponds to the summed difference in total and longitudinal momentum for these tracks. The acceptable value of 1.5 for 1994 running was lower than for previous years in order to keep low multiplicity events, for example elastic ρ and J/ψ candidates. These would otherwise have been lost had the cut been tighter than this, due to the potentially low sum total of this parameter over the low number of tracks in these events.

Chapter 5

Use of the Forward Direction

The forward direction has not previously been used for muon analysis of this type, effectively resulting in an angular cut on muon tracks of approximately $\theta > 20^\circ$ in previous analyses. This biases the topology of the event in favour of the backwards region ($-z$) of the detector, which in turn affects the kinematic selection of an event sample. This chapter will focus upon the nature of muons that are excluded by this cut, their contribution to J/ψ kinematics and the performance of the various forward detectors and triggers during 1994. Data from this running period is compared and contrasted with Monte Carlo simulation.

5.1 Forward Detector Performance in 1994

The forward direction, as mentioned in chapter 2, consists mainly of the Forward Tracker, the forward endcap iron chambers and the Forward Muon Detector (FMD). High energy muon data in this direction is triggered by the Forward Muon Trigger (FMT), a sub-trigger operating at level 1 in the H1 triggering system in the manner described in section 2.2.5. Triggered events then undergo level 4 and event classification and are subsequently written to dataset tape (DST) for later analysis (see chapter 4).

5.1.1 The Forward Muon Detector

During 1994, there was a serious problem with the currents drawn by the final layers of the Forward Muon Detector which meant that for a great deal of collected beam luminosity this detector was not included in the H1 detector read-out. The reason behind these high currents was later found to be caused by synchrotron radiation from the electron/positron beam. A series of collimators are positioned in front of the H1 detector (with respect to the incoming electron beam), whose purpose are to shield the detector from such radiation. However, synchrotron radiation from the electron beam was being scattered in unexpected directions during 1994, and was getting past the collimators and into the beam-pipe wall by the FMD. This caused huge numbers of secondary particles to strike layers of the FMD. Figure 5.1 shows an example of the currents drawn in each of the four theta layers, and clearly demonstrates the problem. The part of the detector mainly affected was the θ_4 layer, positioned furthest from the interaction point and the first layer encountered by the electron beam. During normal operation no one area of a layer is expected to draw larger currents than any other, with these currents remaining below $\sim 10 \mu\text{A}$. In contrast, the scale of figure 5.1 shows that areas of θ_4 were drawing above $25 \mu\text{A}$ at this stage.

However, this problem did not affect the entire data for the year and a brief summary of the status of the FMD is given in table 5.1.

<i>Run Range</i>	<i>Luminosity nb^{-1}</i>	<i>HERA Status</i>	<i>FMD Status</i>
76137 → 82005	498	e^-p running	okay
83146 → 87049	1173	e^+p running	reduced efficiency
87050 → 88847	1114	"	zero efficiency
88849 → 89912	709	"	$\approx 50\%$ efficiency
90101 → 90419	299	"	okay

Table 5.1: *Status of the Forward Muon Detector during selected run ranges of 1994 data taking. The integrated luminosity collected for each range is also shown.*

Currents of the Forward Muon system

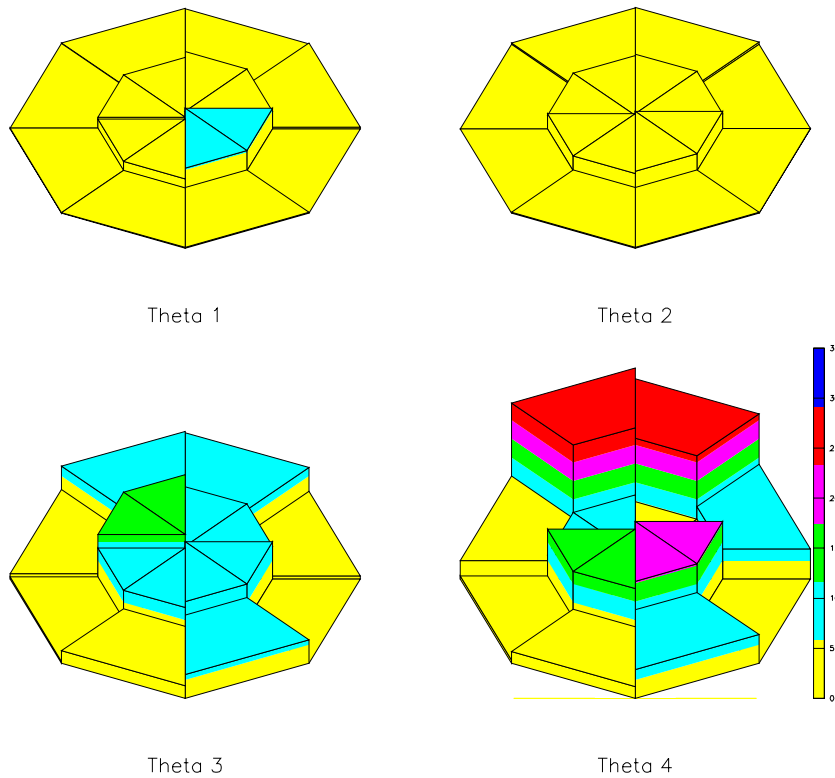


Figure 5.1: Example of unacceptably high currents drawn in layer θ_4 compared with the other three theta layers. The scale of the key alongside θ_4 shows units of μA .

When high currents are drawn by FMD cells in an area of a layer, they must be reduced by turning down the high voltage (HV) powering the cells in that area. The status of voltage on specific regions of the Forward Muon Detector is automatically included in the read-out of the detector, which records the status as switched on or off. However, often during a run in 1994, the voltage on a troublesome area was merely turned down until any high currents drawn in that area fell to an acceptable level. This action would have led to the area being effectively off, although according to the readout the area was fully operational. Another problem was that for each layer, a sample HV channel was taken to be representative of the

status of that layer. For example if the representative channel was flagged on or off for θ_4 , then all of the layer θ_4 was flagged as being on or off, regardless of whether the other HV regions in θ_4 were operational or not.

With the volts on the cells off and area reduced to some lower value, the hit efficiency¹ of those cells is also reduced to some unknown lower value. With the reconstruction code of the FMD (MTREC) looking for hits in the layers with which to reconstruct a track, areas of inactivity of this type will clearly affect its ability to do so. Hence it was not possible to tell from the detector read-out what the track reconstruction efficiency of the FMD was for long periods of time for 1994, leading to some entries in table 5.1 being merely estimates.

A postmortem method therefore had to be developed to measure these periods of inactivity of HV regions of the Forward Muon Detector. To do this the number of hits in these regions of the layers was measured for each run in 1994 and normalised to a particularly reliable high voltage area for that run. Normalising to the same HV region for every run, the relative number of hits of each region should remain constant between runs. Variations from this constant pattern gives us some idea of changes in efficiency of regions of the detector on a run by run basis. The regions of each layer corresponding to individual high voltage channels are shown in figure 5.3, which also demonstrates how these areas are labelled.

The high voltage channel that was chosen as being particularly reliable was an inner sense region of the θ_2 layer, a choice justified by looking at the low currents ($< 10 \mu\text{A}$) drawn in this area as shown in figure 5.1. This layer was amongst those shielded from the synchrotron radiation by the forward muon toroid and gave no problems throughout the entire running period. The inner sense areas closer to the proton beam also tended to receive a greater number of hits than the outer areas, thus reducing the likelihood of us having no hits in this area to normalise to during shorter H1 runs. Figure 5.2 shows an example of the normalised number of hits in each voltage region for two layers of a particular run. A couple of features merit note: the upper plot shows an area with no hits at all (Q_2 Outer 2), and also

¹The efficiency of a muon producing a pulse of charge at the sense wire of a FMD chamber.

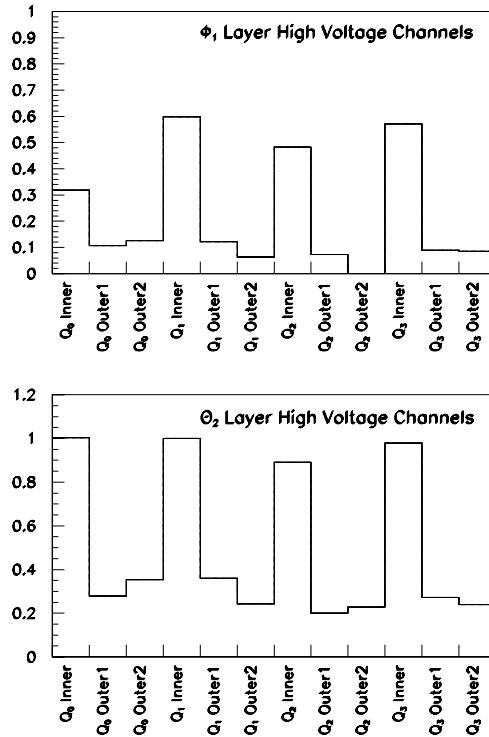


Figure 5.2: The normalised relative number of hits in each voltage region for the layers ϕ_1 (upper) and θ_2 (lower). The quadrants are labelled $Q_{0\dots3}$.

an area (Q_0 Inner) with approximately half the number of hits as the other inner layers. These correspond to a dead outer 2 channel in quadrant 2, and the inner channel of quadrant zero running at half efficiency. Both of these effects had been previously known to us and provided confidence in this method.

Once this had been done for every run of analysis quality in the 1994 data, trends were sought for in the efficiency of the layers, for example long periods of time for which particular HV regions were off or running at approximately the same reduced efficiency. Once done, suitable dead areas were added to the simulation data of the Forward Muon Detector and Monte Carlo files were re-simulated with this new version (H1SIM 3.0620 and higher). The simulation of files is described in more detail in section 5.2.

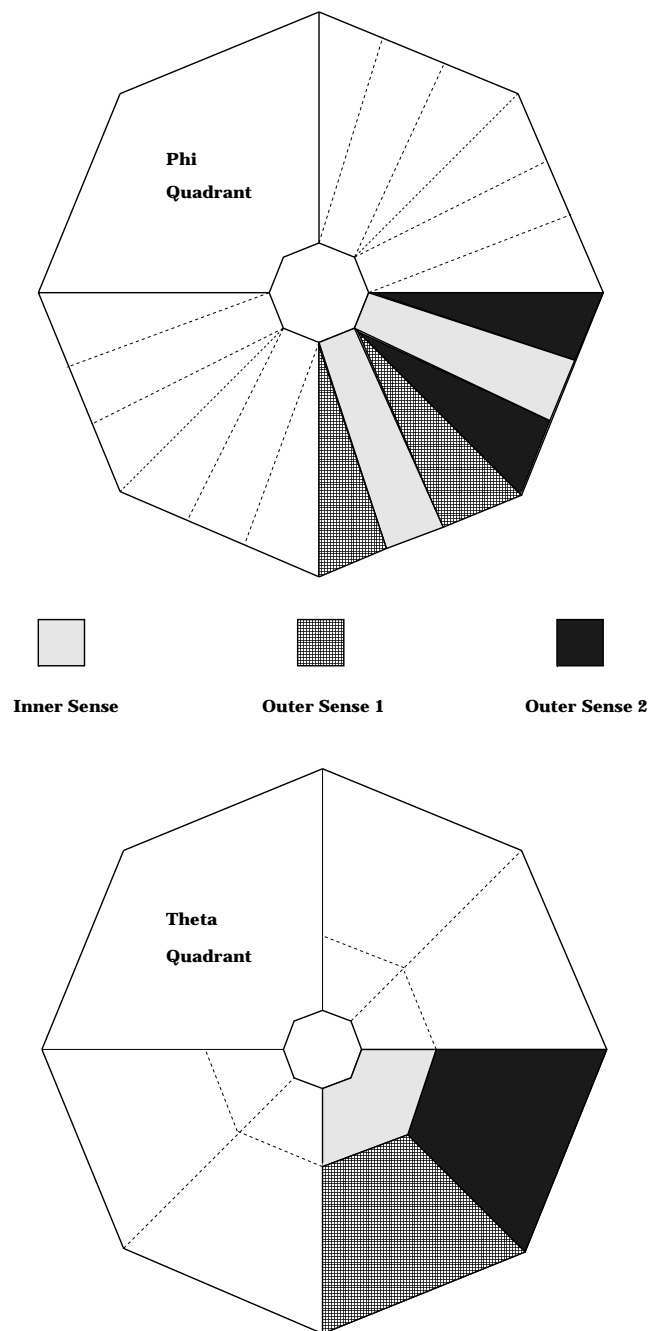


Figure 5.3: *The position of regions whose cells are powered by individual high voltage channels denoted Inner, Outer 1 and Outer 2. The upper plot shows their arrangement within a quadrant of a phi layer, the lower plot within a theta layer quadrant.*

5.1.2 Forward Tracker Performance

As described in section 2.2.1 the forward direction at H1 has its own special sets of tracking modules to aid particle detection in this region. The Forward Tracker performed consistently during 1994 data taking and for this study was used in conjunction with the various muon detectors to search for muons in the data. Forward Tracker reconstruction efficiencies for muon-linked tracks is shown in figure 5.4. These were measured by demanding an extremely good quality forward iron endcap muon track that could be extrapolated back to the event vertex, then measuring the Forward Tracker response. Note that a track hereby denoted as a ‘forward’ track has no central tracker contribution and vice versa. Combined tracks are those fitted through hits in both central and forward tracking detectors. The cuts on the iron endcap track follow, with the numbers given in parentheses being the standard definition of a muon by the level 5 classification code for class ECMUON described in chapter 4.

- Track points back to within radial distance of 50 cm (100 cm) of the nominal vertex position.
- Track began within the first 4 (5) layers of the iron endcap.
- Track consists of at least 7 (6) iron layers.

These cuts were designed to reduce contamination by cosmic and beam-halo muons, and to ensure that the muon passing through the iron definitely passed through the Forward Tracker. We then measure the response of this detector, providing us with an accurate measurement of its efficiency.

The efficiencies shown in figure 5.4 correspond to a combination of the inner tracker efficiency of finding track segments, the efficiency of the code that links these to form a full track fitted to the event vertex and the code that links the iron muon track back to this inner track. The combined efficiency of these processes has been measured as a function of track angle θ as measured from the entry point of the iron endcap track.

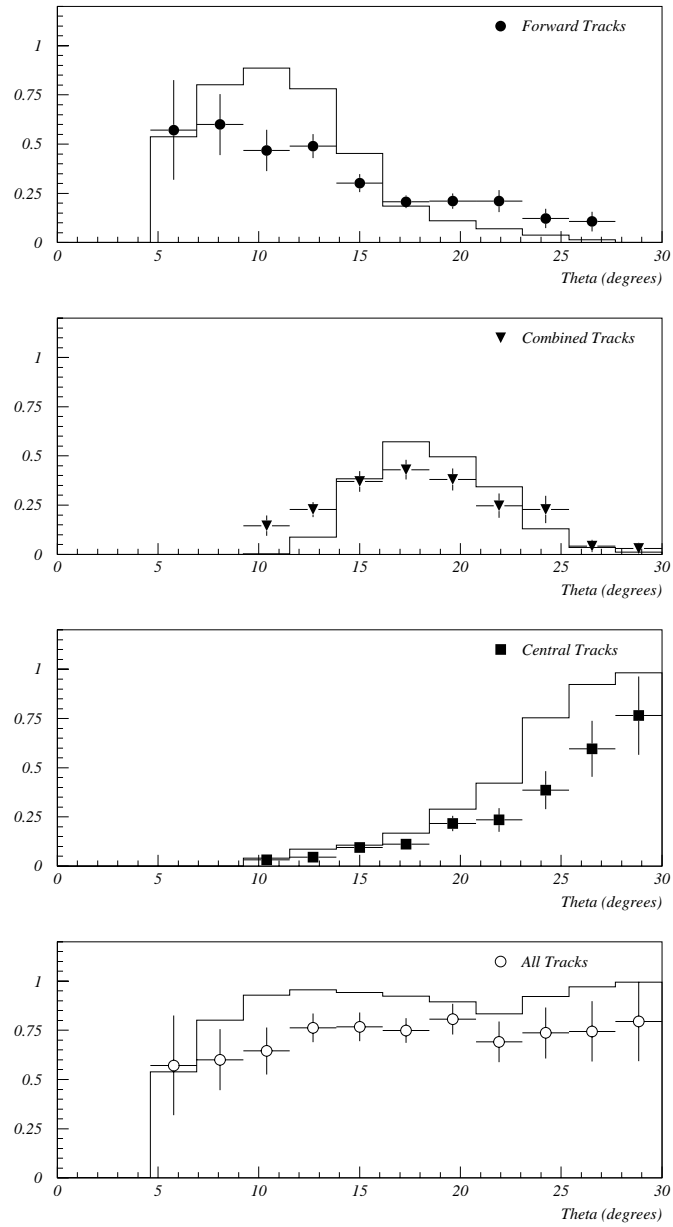


Figure 5.4: Forward, combined, central and total track efficiencies for 1994 shown as a function of track angle θ .

The definition of a good Forward Tracker track is as shown in table 4.1, with the following additional quality cuts:

- At least 2 planar layers comprising of the track, no radials required.
- If only 1 planar segment, at least 1 radial layer in the track fit.

These cuts were the same cuts as used in forward J/ψ analysis in this thesis. They are required to ensure faith in the parameters given by the forward tracker, particularly the momentum measurement. Only vertex-constrained tracks were used for this analysis, with momentum and angle measurements given being those at the event vertex, whose extrapolated position is found using all inner tracks in each event.

As expected, the plot of efficiency against angle θ shown in figure 5.4 shows that forward, combined and central tracks each have their maximum efficiency at values offset to one another. If we combine these efficiencies we arrive at the total distribution (lower plot), which shows the total efficiency of tracking muons in the forward direction $\theta < 30^\circ$. It is seen that the efficiency in simulation is generally higher than for data. It is thought that the dip in efficiency at around 22° is due to inefficiency in the code that links the forward and combined tracks, an effect possibly due to multiple scattering of tracks at this angle as they pass through the wall at the end of the Central Jet Chamber.

5.1.3 Forward Muon Trigger

The triggering scheme at H1 was mentioned in section 2.2.5, but one trigger of particular use to us is the Forward Muon Trigger (FMT). This trigger is fully documented elsewhere [1] but a brief description is included here.

During 1994 running, two sub-triggers were used to seek forward going muons. The validated FMT looked for full Forward Muon Detector tracks at level 1 of the H1 triggering scheme, while the pre-toroid FMT looked for pre-toroid tracks

in the FMD. This latter sub-trigger had problems with high rates during the 1994 running period, and was ‘pre-scaled’ by a factor of 10. This meant that for every 10 times this sub-trigger fired, only one of these bunch-crossings was kept. The validated FMT suffered heavily from the inactivity of the final layers of the Forward Muon Detector during 1994, and was also measured to be only approximately 50 % efficient during normal operation [28]. The pre-scale on the pre-toroid FMT precluded any attempt to use this sub-trigger for analysis. The triggers that were used are described in section 6.2.2, and all of the plots shown in this chapter show events that were found by this set of triggers.

It was planned for 1995 data taking that a looser cut be placed upon the full-track trigger, with the definition of a full track being 3/4 hit layers rather than the 4/4 for 1994. This of course leads to a higher trigger rate at level 1. This effect is compensated by the inclusion in 1995 of level 2 and 3 pipelined trigger steps, which look for topological combinations between FMD tracks and forward proportional chamber hits. The lower threshold of inner track momentum of muon candidates the trigger passes was also raised. These steps were aimed to prevent the need for pre-scales on the triggers, and to increase the efficiency of the trigger as a result. A first look at the 1995 operation has shown this indeed to be the case [28].

5.2 Monte Carlo Simulation

For future use of the FMD in analysis, it is necessary to have a simulation that accurately reflects the status and response of various detectors during the data taking in order to enable a realistic comparison between data and Monte Carlo. At H1, the simulation package H1SIM consists of three separate stages, namely the GEANT, DIGI and TRIGGER steps. An event generator first simulates the desired $e^\pm p$ collision. A simplistic description of these stages follows.

First of all, Monte Carlo generator programs are used to simulate chosen collisions and processes at the detector vertex. In our case the end result is the process $\gamma p \rightarrow J/\psi p$. The output of the generator then provides input to the fol-

lowing GEANT stage. The GEANT program uses information about the physical properties of material comprising the detector, and also of the many physical processes that can occur when particles traverse it, such as multiple scattering, e^+e^- pair production to name but two. The program tracks particles from the generator level through the detector and produces information on the position of the particles as they pass through the various sensitive regions of the detector. The response of these sensitive regions is then simulated by the following DIGI step, which converts the space points provided by GEANT into a set of parameters (e.g. charges and times) to be used later on to find tracks by the reconstruction code of the various sub-detectors. A certain amount of smearing of these two parameters is done in order to reproduce the desired resolution of the individual sub-detectors.

At this stage, we have all the information that we would start with had we been considering a real data event, and the TRIGGER step then goes through the process of simulating the response of all the individual sub-triggers of H1 had they encountered the event during normal data-taking. However, it should be noted that the pre-scaling of sub-triggers, such as that of the FMT mentioned earlier in section 5.1.3, is *not* included when producing Monte Carlo files in this way. The files then go through the process of event classification precisely as data would.

The Monte Carlo files used for this study of the forward direction correspond to elastic and proton-dissociative J/ψ photoproduction through the Vector Meson Dominance model, processes displayed in figure 3.2 and described in section 3.4.1. In each case the detector response to the generated events was simulated and reconstructed using a detector description containing information of FMD dead areas described in section 5.1.1. It was not possible to include dead areas on a run-by-run basis, rather general trends of inactivity in different periods of the data taking were included by killing suitable combinations of HV channels during the DIGI step of the simulation.

5.2.1 Forward Muons in the Simulation

Some of the properties of the muons produced in the Monte Carlo files are shown in table 5.2 for the elastic case, and table 5.3 for the case where the proton dissociates. These numbers are *generated* values and as such take no account of detector, trigger or other efficiencies.

			μ^+				
			$7^\circ < \theta < 17^\circ$		$17^\circ < \theta < 155^\circ$		$\theta > 155^\circ$
			$p < 5$	$p > 5$	$p < 2$	$p > 2$	all p
μ^-	$7^\circ < \theta < 17^\circ$	$p < 5$	0	16	288	40	40
		$p > 5$	14	382	218	318	0
	$17^\circ < \theta < 155^\circ$	$p < 2$	260	222	1422	1044	746
		$p > 2$	28	318	1010	868	266
	$\theta > 155^\circ$	all p	44	0	724	254	594

Table 5.2: Elastic J/ψ Monte Carlo simulation. Properties of muon pairs from simulated J/ψ decay are shown, where p is the μ^\pm momentum in GeV. The numbers correspond to simulated luminosity of 60 pb^{-1} .

			μ^+				
			$7^\circ < \theta < 17^\circ$		$17^\circ < \theta < 155^\circ$		$\theta > 155^\circ$
			$p < 5$	$p > 5$	$p < 2$	$p > 2$	all p
μ^-	$7^\circ < \theta < 17^\circ$	$p < 5$	1	7	243	39	43
		$p > 5$	8	158	138	190	1
	$17^\circ < \theta < 155^\circ$	$p < 2$	187	148	1420	1123	887
		$p > 2$	36	184	1037	620	360
	$\theta > 155^\circ$	all p	57	2	953	340	818

Table 5.3: Proton-dissociative J/ψ Monte Carlo simulation. Properties of muon pairs from simulated J/ψ decay are shown, where p is the μ^\pm momentum in GeV. The numbers correspond to simulated luminosity of 20 pb^{-1} .

Tables 5.2 and 5.3 show several similarities. For instance it is seen that large numbers of muons are produced in the central region with momenta $< 2 \text{ GeV}$. This was the reason behind the implementation in 1994 of a muon-finding routine using clusters left in the calorimeters [29]. Previous muon identification in this area

had been left to the barrel muon chambers, requiring over 1.5 GeV momentum for detection and thus biasing event kinematics and lacking the extra level of detection efficiency available from including the calorimeters. It is also clear from the tables that most muons produced in the forward direction have momenta > 5 GeV, making them visible to the FMD.

As mentioned in section 5.1.3, the loss of the Forward Muon Trigger during 1994 has meant that we accept only muon events triggered by central barrel or topological triggers and not those specifically designed to seek muons in the forward direction. Hence the number of forward-going muons in our data sample will be much reduced. We find that data gives us just 2 events reconstructed containing a full forward muon track linked to an inner track within the J/ψ mass range, using our central trigger selection. By reconstructing the detector response of these Monte Carlo files and normalising their luminosities (60 pb^{-1} and 20 pb^{-1} for elastic and proton-dissociative respectively) to the 1994 H1 positron luminosity considered of $\sim 3 \text{ pb}^{-1}$, we find Monte Carlo predicts 1 event (elastic) and 2 events (dissociative) will be reconstructed by us using precisely the same trigger selection and reconstruction code. It is not known what exact proportion of these two processes constitutes our quasi-elastic data sample, but it is clear that the numbers are in agreement to order of magnitude. If we allow the extra option when selecting Monte Carlo events that the event was triggered by a simulated full track Forward Muon Trigger without pre-scaling, then the numbers from the simulation rise to 2 (elastic) and 10 (dissociative) events in approximately 3 pb^{-1} of luminosity. The uncertainty on the total of 12 is ± 1.5 and shows the sort of numbers that may have been possible.

The effect of our imposed trigger selection is shown in tables 5.4 and 5.5 and diagrammatically in figure 5.5. It is seen that the majority of the muons are in the central and backward areas of the detector, and by comparison with tables 5.2 and 5.3 that many muons generated in the forward direction are not found by the set of sub-triggers used. However the upper plot of figure 5.5 shows clearly the potential of the FMD and the trigger in the forward direction, with the momentum of muons produced tending to increase above 5 GeV as θ decreases below around 20° .

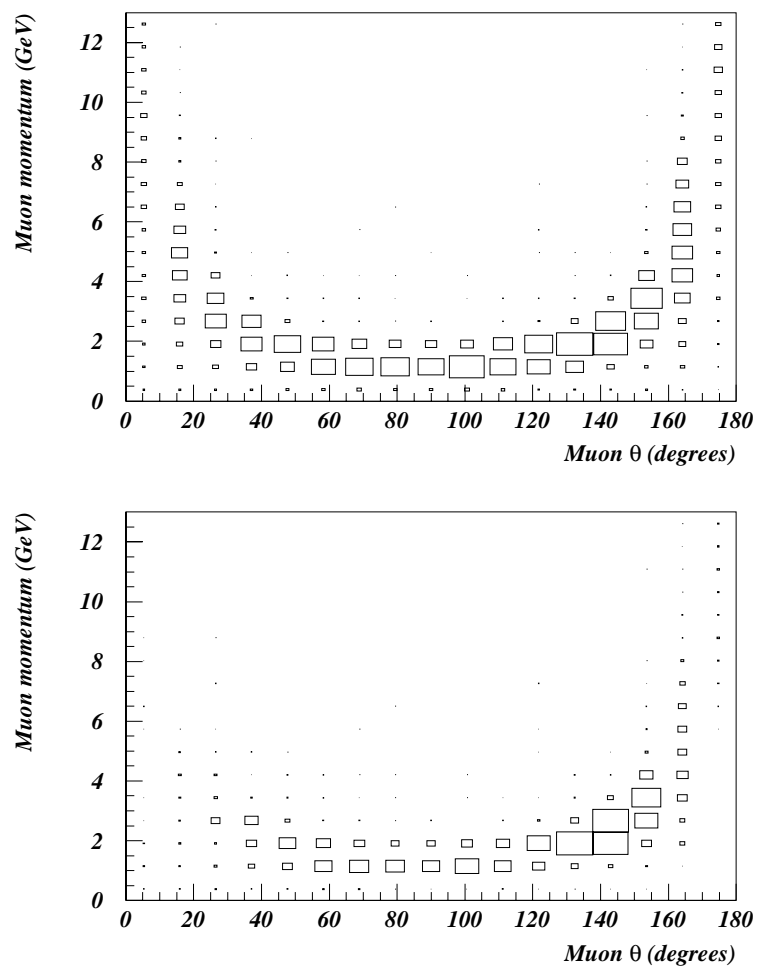


Figure 5.5: Effect of our trigger selection on generated forward muons. Muon momentum is plotted against θ angle with no trigger selection (upper), and using our trigger selection (lower plot) without inclusion of the Forward Muon Trigger simulation.

			μ^+				
			$7^\circ < \theta < 17^\circ$		$17^\circ < \theta < 155^\circ$		$\theta > 155^\circ$
			$p < 5$	$p > 5$	$p < 2$	$p > 2$	all p
μ^-	$7^\circ < \theta < 17^\circ$	$p < 5$	0	0	19	13	1
		$p > 5$	0	1	20	9	0
	$17^\circ < \theta < 155^\circ$	$p < 2$	28	17	504	521	188
		$p > 2$	8	14	430	438	161
	$\theta > 155^\circ$	all p	3	0	161	171	16

Table 5.4: Elastic Monte Carlo simulation. Generated properties of J/ψ decay muons are shown, that have been selected by our set of sub-triggers.

			μ^+				
			$7^\circ < \theta < 17^\circ$		$17^\circ < \theta < 155^\circ$		$\theta > 155^\circ$
			$p < 5$	$p > 5$	$p < 2$	$p > 2$	all p
μ^-	$7^\circ < \theta < 17^\circ$	$p < 5$	0	0	11	11	5
		$p > 5$	0	0	2	7	0
	$17^\circ < \theta < 155^\circ$	$p < 2$	13	2	288	458	303
		$p > 2$	12	5	428	302	196
	$\theta > 155^\circ$	all p	2	0	286	170	24

Table 5.5: Proton-dissociative Monte Carlo simulation. Generated properties of J/ψ decay muons are shown, that have been selected by our set of sub-triggers.

5.3 Forward Contribution to Kinematics

The forward direction is potentially very important to future physics analysis. The additional angular range provided by forward detectors allows us to extend measurements of many kinematic properties beyond the range available from the rest of the detector.

An invariant mass distribution of J/ψ decay to a di-muon pair of opposite charge, where one or both muons are detected by the Forward Tracker is shown in figure 5.6. The Breit-Wigner fit to the data points gives a mean of (3.10 ± 0.03) GeV and a width of the signal at half of its maximum height (FWHM)

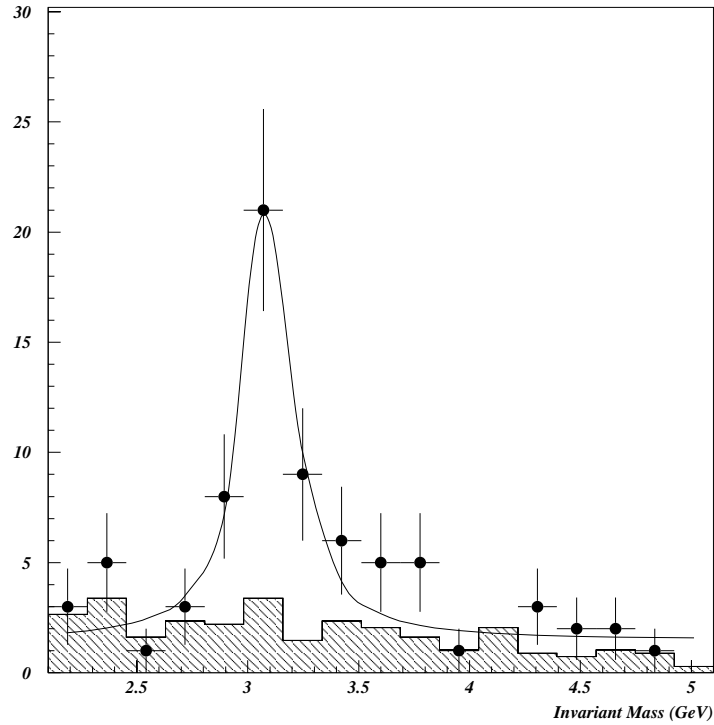


Figure 5.6: Invariant mass distribution for events containing one muon in the forward direction. The mean of the Breit-Wigner fit is (3.10 ± 0.03) GeV. The shaded area shows QED background events from Monte Carlo simulation of the process $\gamma\gamma \rightarrow \mu^+\mu^-$.

of (0.26 ± 0.09) GeV. Converting this width to a standard deviation² we obtain $\sigma = (0.11 \pm 0.04)$ GeV. A linear fit has been superimposed upon the fit to the signal to describe the background at either side of the signal.

To give an idea of the cause of the background, the shaded area of figure 5.6 shows invariant mass of muon pairs from Monte Carlo simulation of the $\gamma\gamma \rightarrow \mu^+\mu^-$ process, normalised to 1994 luminosity. The muons from this background source underwent precisely the same cuts as those in the data. This process is seen to account well for the number of background events seen on the data signal.

²Using the conversion $\sigma = \frac{\text{FWHM}}{\sqrt{(8 \ln 2)}}$.

When measuring the number of J/ψ events in the forward direction, it is necessary to remove the contributions from the background of figure 5.6. In the plots that follow, the kinematics are plotted for data within an area $\frac{3}{2}\sigma$ either side of the mean of the data fit. The numbers of events lying $\frac{3}{2}\sigma$ above and below this region were determined and subtracted from the signal. This method of using the sidebands of the data signal to estimate the background contribution was preferred to the use of Monte Carlo simulation of the QED process $\gamma\gamma \rightarrow \mu^+\mu^-$ for the same purpose.

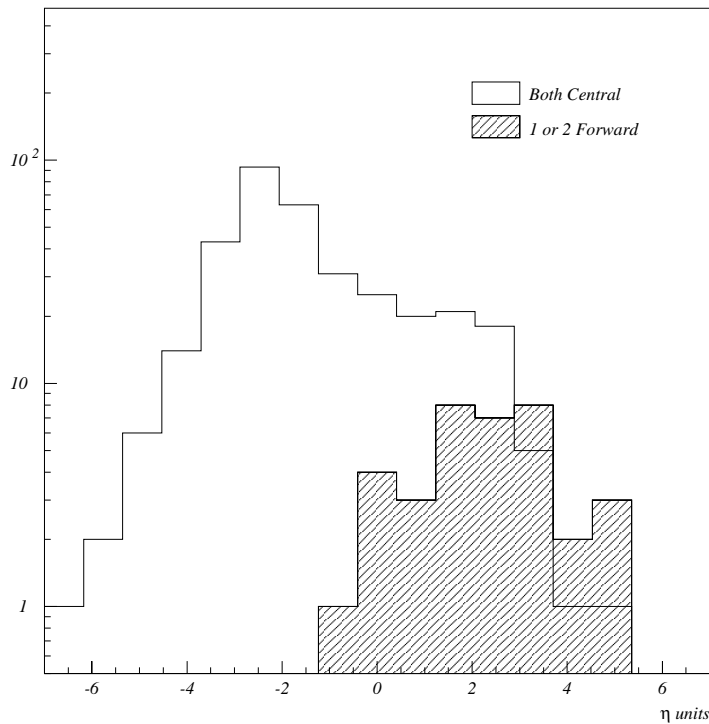


Figure 5.7: Contributions to J/ψ pseudorapidity from events found in data consisting of two central tracks, and those with one or two forward tracks (shaded histogram).

Figure 5.7 shows the forward contribution to the pseudo-rapidity of the J/ψ particle ($\eta_{J/\psi}$) in 1994 data. The contribution of the central area was measured in the same way as for forward tracks, with the same method of background subtraction.

The details of the fit to the central invariant mass distribution are included in chapter 6.

It can be seen from figure 5.7 that the forward direction can extend the $\eta_{J/\psi}$ measurement in the area of 0 to 5 rapidity units and further. The pseudorapidity values (η_{track}) that single muon tracks themselves may achieve in the H1 detector have a maximum of around 2.5 units due to the angular limitations imposed by the beam-pipe. It is the combinations of these very forward tracks with other tracks that allow the measured total pseudorapidity $\eta_{J/\psi}$ of the J/ψ particle to be extended to the values shown. There appears also to be a larger number of events at around -2 and $+2$ rapidity units in figure 5.7. Merely using central tracks cannot find all of the events in the excess at $+2$ units, and this is where the forward detectors are of great importance.

Equation 3.2 gives a definition of the centre of mass energy of the γp system $W_{\gamma p}$, and the reconstruction technique of this variable is demonstrated in chapter 4. As shown in figure 5.8, the forward direction becomes important in detecting events with low values of $W_{\gamma p}$, potentially extending the measurement down to a value below around 30 GeV. Again, these values correspond to events within $\frac{3}{2}\sigma$ of the mean of figure 5.6.

5.4 Angle and Momentum Measurement

For 1994 data, a comparison was made of the momentum of tracks left in the Forward Tracker and those left in the FMD by single muons from the vertex. For this study, forward tracks were used that had links to the Forward Muon Detector. The total number of these muons after quality cuts was 54, with no cuts on invariant mass or event kinematics. From these, we can make a first study of multiple scattering in the material between the Forward Tracker and the Forward Muon Detector, and also compare momentum measurements in both these detectors.

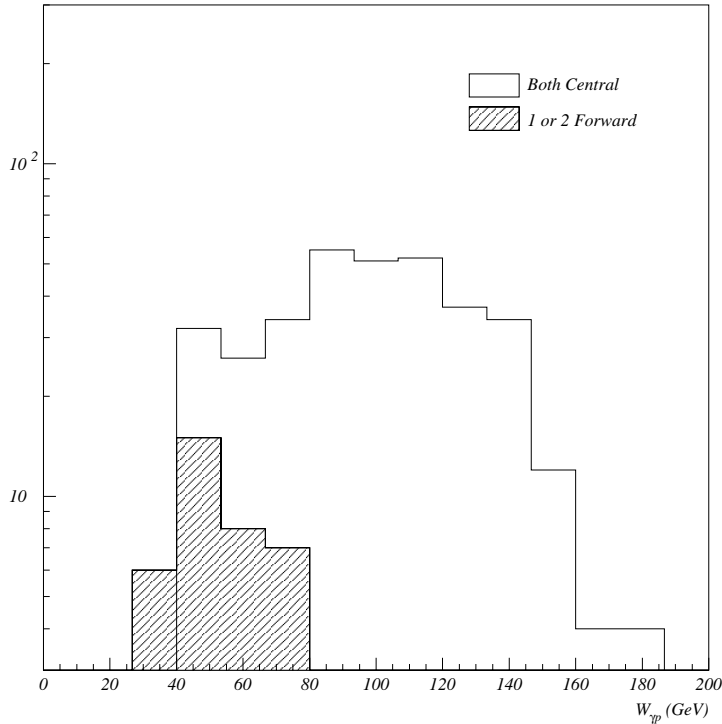


Figure 5.8: Contribution to the $W_{\gamma p}$ distribution from forward tracks (shaded histogram) and central tracks (solid histogram) in 1994 data.

5.4.1 Multiple Scattering

Previous studies [30] have used Monte Carlo simulation to describe multiple scattering of muons in the material of the H1 detector before entry to the FMD. Some of these findings are examined here using data taken in 1994. Figure 5.4.1 shows schematically the angles θ_{FMD} , θ_{POE} and θ_{VTX} that will be used in this study, although the level of scattering of the muon has been exaggerated in the diagram. The angle measured in the pre-toroid layers of the FMD is denoted θ_{FMD} , while the angle given by the extrapolation back to the vertex of the point of entry to the FMD is given by θ_{POE} . The angle θ_{VTX} is the initial angle of the muon at the event

vertex. As we use only vertex constrained tracks in our study, this is the value of theta given by the Central and Forward Tracker data banks.

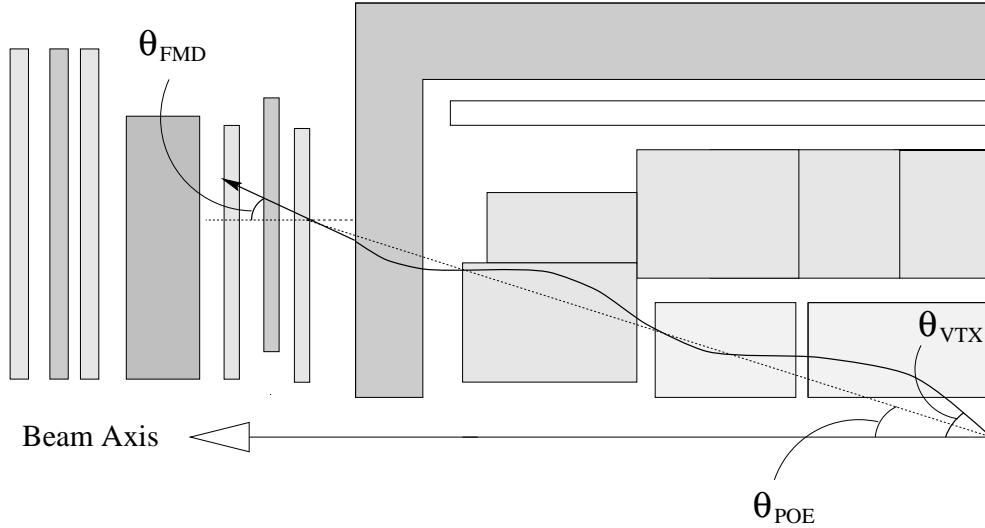


Figure 5.9: A section of the H1 detector is shown, illustrating the angles θ_{FMD} , θ_{POE} and θ_{VTX} characteristic of multiple scattering.

Let us consider the two distributions $\theta_{FMD} - \theta_{VTX}$ and $\theta_{POE} - \theta_{VTX}$. Both distributions are expected to be normal, with standard deviations we shall call θ_1 and θ_2 respectively. Particles passing through a constant medium are expected [16] to show the relationship $\theta_1 = \sqrt{3}\theta_2$. However, the material between the vertex and the FMD at H1 is not a constant medium, with the iron detectors causing most scattering. This would cause the constant factor in the above relationship to be greater than $\sqrt{3}$.

Using our sample of forward linked muons the values of θ_1 and θ_2 were directly measured and found to follow the relationship $\theta_1 = (2.9 \pm 0.6)\theta_2$. The value of the constant is, as expected, found to be larger than $\sqrt{3}$, and all distributions were found to be normal. This value compares well with the value obtained from Monte Carlo simulation of J/ψ events which gives $\theta_1 = (2.932 \pm 0.102)\theta_2$ from almost 20 thousand simulated events.

A prediction of the degree of scattering as a function of muon energy, also done in previous simulation studies [30] has led to the results of equation 5.1,

$$\begin{aligned}\theta_1 &= \frac{0.18}{p - 1.5} \text{ rad} \\ \theta_2 &= \frac{0.06}{p - 1.5} \text{ rad}\end{aligned}\tag{5.1}$$

where p is the momentum of the muon at the vertex and the factor of 1.5 is a first-order correction for energy loss of the muon before the FMD.

The relations 5.1 were found to hold for our data, with the distributions shown in figure 5.10. The upper two plots of the figure show the distributions $\theta_{FMD} - \theta_{VTX}$ and $\theta_{POE} - \theta_{VTX}$, whose standard deviations give us the values of θ_1 and θ_2 of (0.041 ± 0.008) rad and (0.014 ± 0.001) rad respectively. The large distance in z between the accurately known event vertex and first FMD layer position causes this measurement to be more accurate than for the comparatively short pre-toroid track ($\theta_2 < \theta_1$). The lower two plots show distributions of θ_1 and θ_2 obtained from muon momenta by using equations 5.1, the mean values of which give us the values $\theta_1 = (0.035 \pm 0.003)$ rad and $\theta_2 = (0.011 \pm 0.003)$ rad. These two values agree with the previous two values within error. It seems therefore that this multiple scattering effect is well modelled by the material simulation of the detector.

5.4.2 Momentum Loss

Another effect introduced by the material between the vertex and FMD is an attenuation of particle energy. Again, our data sample can be used to test the accuracy of previous simulation studies.

Figure 5.11 shows the difference between particle momenta measured by the Forward Tracker and the FMD for tracks linked between these detectors. The fit to the data contained in figure 5.11 gives us a value of (2.4 ± 0.3) GeV, for the mean energy loss between vertex and FMD. This is to be compared to the corresponding

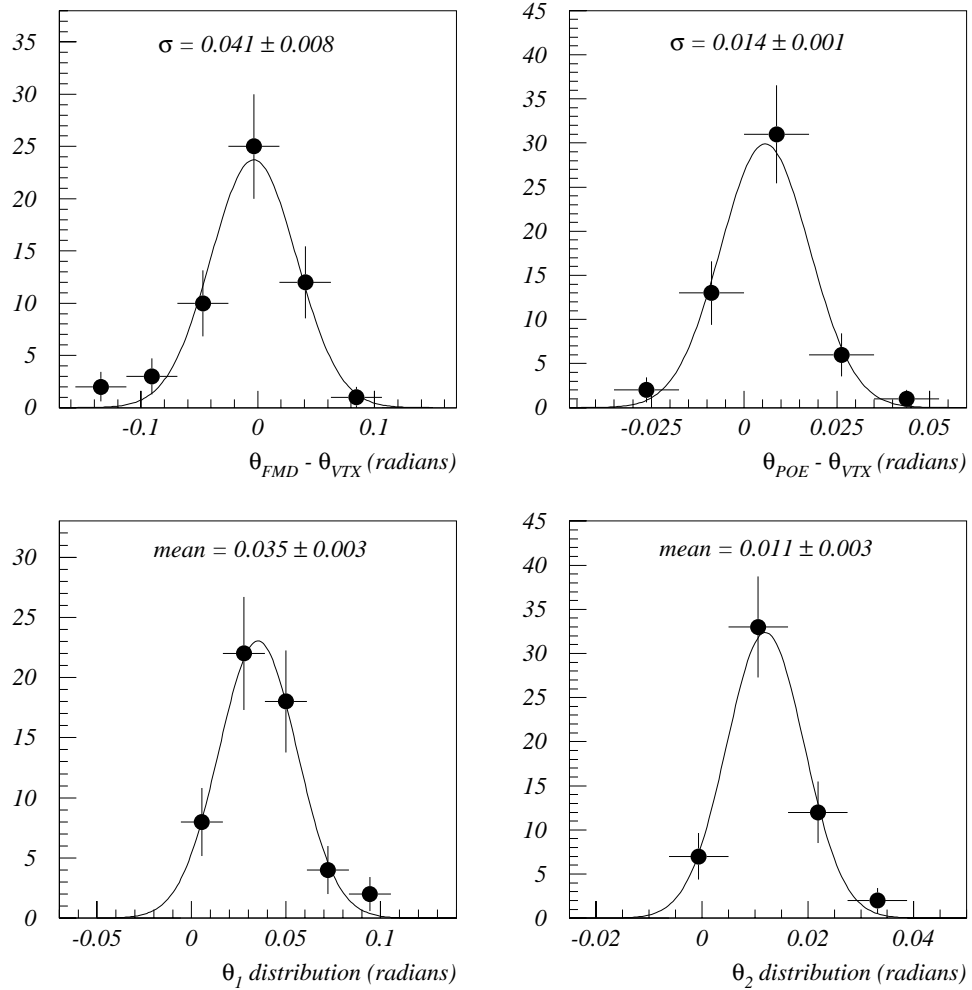


Figure 5.10: Various distributions used in our study of multiple scattering. The upper two plots show differences in angle θ reconstructed from FMD hits (θ_{FMD}) and point of entry (θ_{POE}) compared with the vertex value (θ_{VTX}). The σ values of the left and right hand upper plots are expected to agree with the mean values of the corresponding left and right hand lower distributions, the latter obtained from muon momenta.

value reconstructed from our J/ψ Monte Carlo of (2.80 ± 0.05) GeV. It can be seen that the values from data and Monte Carlo narrowly fail to agree within the quoted errors on their mean values, but were found to comfortably agree within 1 standard deviation. This is not to say that the Forward Muon Detector can measure muon momenta just above 2.4 GeV, as a FMD momentum measurement can only be made once the muon has also passed through all six layers and the forward toroid, requiring an average of around 2.25 GeV more [30]. It can therefore be seen that a muon will require a minimum momentum of around 4.7 GeV to be detected and measured by the FMD.

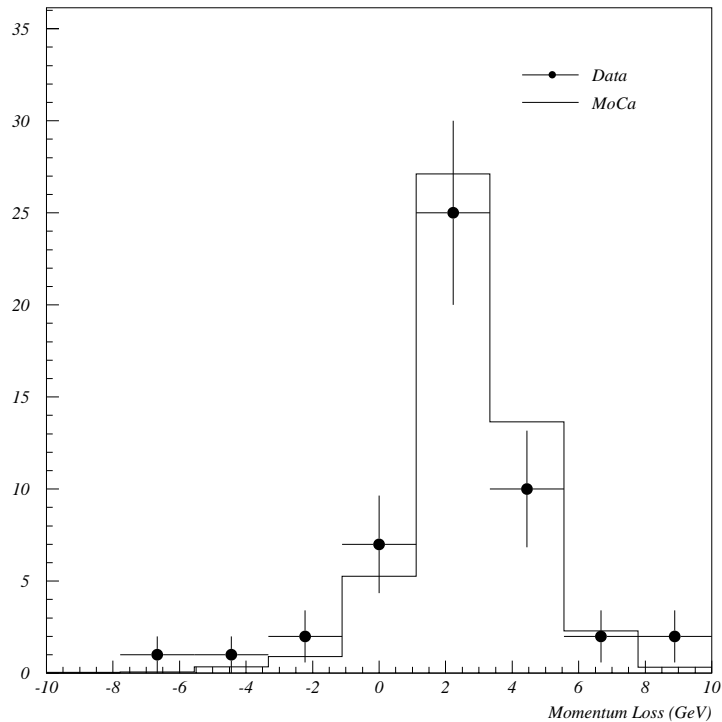


Figure 5.11: Momentum difference between measurements in the forward tracker and FMD for muons originating at the H1 vertex. Distributions are shown for data (points) and Monte Carlo simulation (solid histogram).

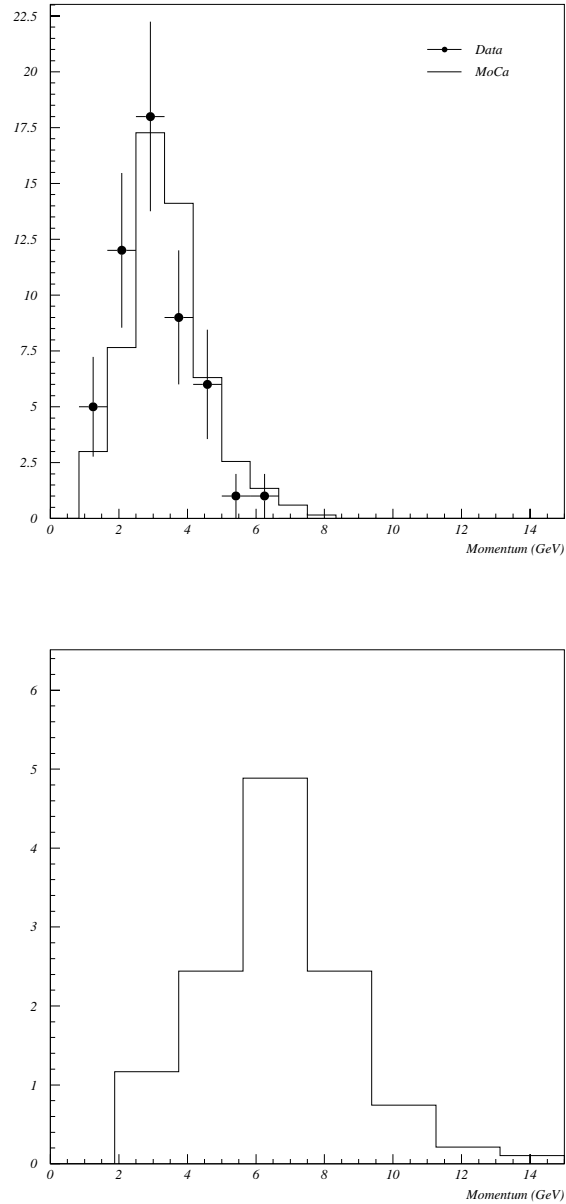


Figure 5.12: The upper plot shows forward momentum distribution of J/ψ events with one forward-going muon with our data sample and trigger selection (upper), and for 3 pb^{-1} of combined elastic/dissociative Monte-Carlo. The lower plot shows MC events found exclusively by simulation of the FMT for the same total luminosity.

The vertex momentum distribution of J/ψ decay muons in the forward direction is shown in the upper plot of figure 5.12. The points correspond to data, the solid line to Monte Carlo. The range of momentum extends up to a value of 7 GeV, with around 16 % of muons having a momentum measured as greater than 4.7 GeV. This is true of the event selection we chose for this particular study (i.e. with kinematic and invariant mass cuts), and for the trigger selection we have had imposed. The lower plot of figure 5.12 shows the momentum distribution for a 50/50 combination of elastic and dissociative J/ψ decays found exclusively by the Forward Muon Trigger, without any pre-scaling factor on the simulation of this trigger. The momenta of these muons can be seen to extend far beyond 4.7 GeV. This is a similar effect to that shown earlier in figure 5.5 and tables 5.4 and 5.5. It has also been shown [30] that for inelastic J/ψ production via photon-gluon fusion, the percentage of high momentum forward going muons is high, with a quoted ratio of 83 % of these muons having momentum greater than 5 GeV.

The effect of the loss of the FMD and therefore the FMT during 1994 can be further highlighted by considering the mass peak shown in figure 5.6. All of these events were triggered by other muon and topological triggers (described in section 6.2.2) and the potential extra number added by using events exclusively triggered by the Forward Muon Trigger was only 3 before further analysis cuts. For this reason, the FMT was not used in the calculation of the $\sigma(\gamma p \rightarrow J/\psi p)$ cross section presented in chapter 6.

A first look at data taken during 1995 HERA collisions has shown consistent performance of the FMT. Indeed, it is thought possible to perform J/ψ analysis on data from that year using events triggered by the FMT alone [31]. Furthermore, preliminary findings show that using momentum measurements from the Forward Muon Detector³ in invariant mass calculations of di-muon pairs yields a narrower resonance than using track momenta given by the Forward Tracker, possibly due to technical problems in this latter detector. This would suggest a superior momentum resolution is available in the FMD. This state of affairs is currently under investigation [32].

³Corrected for energy loss between event vertex and first plane of the FMD.

Chapter 6

Measurement of $\sigma(\gamma p \rightarrow J/\psi p)$

The equation for the cross section σ_{ep} of any production process from ep interactions has the deceptively simple form shown in equation 6.1,

$$\sigma_{ep} = \frac{N}{\mathcal{E} B \mathcal{L}} \quad (6.1)$$

where N is the total number of events of this process found in our data sample, \mathcal{E} is the total acceptance of our method of collecting this sample, B represents the branching ratio of the particle to decay into the final state considered and \mathcal{L} is the total integrated ep beam luminosity over which the data were collected. In our case the process is elastic J/ψ production, so the acceptance must be that for accepting purely elastic events. This chapter presents the measurement of the variables in equation 6.1 and examines potential sources of systematic error that were encountered.

6.1 Sources of Contamination

In order to accurately determine the variable N in equation 6.1, it is necessary to consider all processes that may contribute events to our data sample which are falsely attributed to elastic J/ψ production. It has been mentioned in section 3.3

that a major source of such contamination comes from diffractive events where the proton dissociates but remains undetected. Additional cuts may be made to veto such events. Other contamination processes include for example ‘feed-in’ from the production of higher energy particle states, where these decay into the J/ψ plus other daughter products.

6.1.1 Tagging the Proton Remnant

1994 saw the first operation of the forward proton tagger at H1. This and other forward detectors were used to veto inelastic contamination of our event sample, by seeking energy in the very forward region. Forward energy of this type is caused by fragments of the remnant proton. It has been mentioned already that the Forward Muon Detector (FMD) had also been very useful in this respect to previous analyses. This is also true of the plug calorimeter, covering the polar angle $0.6^\circ \lesssim \theta \lesssim 4^\circ$ in the forward direction. A description of these detectors is presented in chapter 2.

The cuts used for 1994 running to veto events containing proton dissociation are listed below. These are referred to as ‘proton-veto cuts’ throughout this chapter.

- The number of pre-toroid pairs in the FMD ≤ 1 .
- The energy deposited in the plug calorimeter < 3 GeV.
- No hits in the proton tagger scintillators.

A FMD pair is defined as a series of hits in the 2 successive planes of drift chambers that constitute a single layer of that detector (see section 2.2.3). It may appear that this cut excludes or at least reduces the possibility of using muon tracks from J/ψ decay that can be linked to the FMD. Care was taken to ensure this did not occur. Therefore, in events where a full track was found in the FMD, pre-toroid pairs within a radial distance of 50 cm around the track¹ were excluded

¹In the (x, y) plane of the H1 co-ordinate system.

when counting the total number for the event. The post-toroid layers were not used in this cut due to the high numbers of hits in these layers experienced in 1994 caused by synchrotron radiation from the positron beam. This is fully described in section 5.1.1. The cut on plug energy was made at 3 GeV on account of noise levels in this calorimeter during 1994 running [33]. In analyses of data from running periods preceding 1994 this cut was possible at around 1 GeV. By contrast the proton tagger has essentially no noise.

These cuts were made in addition to the cut on the elasticity variable of $|z - 1| < 0.05$ described in section 4.3. They were not expected to be totally efficient at removing dissociative events. The further steps that were taken to fully evaluate the degree of contamination from these events are presented later in this chapter.

6.1.2 Contribution from other Processes

QED and Cosmic Background

Figure 6.1 shows the invariant mass distribution for events passing our proton-veto cuts in more detail. The data points of the upper diagram show a Gaussian fit to the peak superimposed upon a linear background fit. The data correspond to tracks in **all** inner tracking detectors. Monte Carlo simulation of the QED process $\gamma\gamma \rightarrow \mu^+\mu^-$ has been used to successfully model this background in terms of both shape and magnitude, and is shown as the shaded area of figure 6.1. The lower plot of the figure shows the same data points with the peak from elastic simulation added to the QED background. The peak was normalised to the data in the invariant mass range $2.9 \text{ GeV} < M_{\mu^+\mu^-} < 3.3 \text{ GeV}$.

The number of events contained beneath the superimposed Gaussian fit in figure 6.1 is calculated as 163.0 ± 14.1 . This does not include events below the linear background fit. By examination of the total number of events seen in data in the mass range corresponding to $\frac{5}{2}\sigma$ either side of the mean of the fit², we find 176 ± 5 events. The error on this value corresponds to the uncertainty of the fit parameters

²Within this region lies approximately 99% of the events comprising the peak.

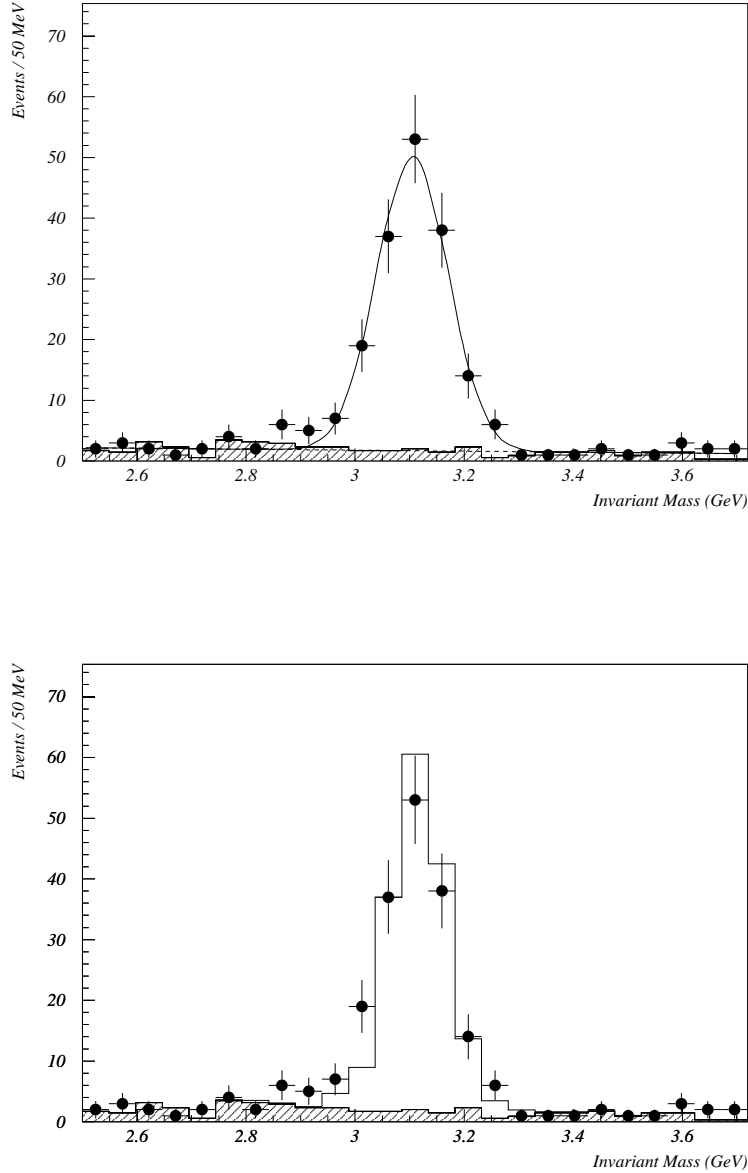


Figure 6.1: Invariant mass distributions of di-muon pairs passing proton-veto cuts. The upper plot shows data fitted with a Gaussian plus linear background fit which is also shown by the dashed line. The lower plot shows data (points) compared with simulation (solid histogram) normalised to the data in the region $2.9 \text{ GeV} < M_{\mu^+\mu^-} < 3.3 \text{ GeV}$. The shaded area on both plots shows simulation of QED background normalised to the data luminosity of 2.89 pb^{-1} .

of the mean and sigma values. In our calculation of the cross section it is necessary to bin our data with respect to $W_{\gamma p}$. This means that in effect we split the invariant mass signal into smaller peaks. For each of these distributions, a similar technique is adopted to superimpose a Gaussian signal upon the background of the distribution to evaluate the number of events contained therein.

This method accounts for all sources of muon pairs which have a flat invariant mass distribution, i.e. not only QED lepton pairs but also the small number of cosmic which are passed by the specific triggers and cuts designed to remove them. Other potential sources of flat background in our invariant mass range are chance muon pairs from π or K decay, or misidentified open charm events.

Feed-in from ψ' Decay

As mentioned in section 3.2 the charmonium level above the J/ψ can itself decay into a di-muon pair via the decay $\psi' \rightarrow \mu^+\mu^-$, or decay into a J/ψ plus other daughter products. Both of these processes are considered background to our calculation. These differ from QED and cosmic background as they contribute specifically to the J/ψ peak, as opposed to a flat mass distribution. Table 6.1 shows some of these decay modes. It can be seen that the ψ' decays into J/ψ plus anything 57 % of the time, with its branching ratio into J/ψ plus neutrals equal to 23 %. It also decays exclusively into a di-muon pair with a branching ratio of 0.8 %.

<i>Bound State</i>	<i>Mass (MeV)</i>	<i>Decay Modes</i>	<i>Branching Ratio (%)</i>
ψ' or $\psi(3685)$	3686.00 ± 0.09	$J/\psi + \text{anything}$	57 ± 4
		$J/\psi + \text{neutrals}$	23.2 ± 2.6
		e^+e^-	0.88 ± 0.13
		$\mu^+\mu^-$	0.77 ± 0.17

Table 6.1: Currently accepted properties of the charmonium state ψ' including some principle decay modes branching ratios.

The only case where we may be deceived into confusing J/ψ production with ψ' decay into a J/ψ plus other decay products is in the case where these other products are of neutral charge, for instance the decays

$$\begin{aligned}\psi' &\rightarrow J/\psi + \pi^0\pi^0 \\ \psi' &\rightarrow J/\psi + \eta \\ \psi' &\rightarrow J/\psi + \pi^0\end{aligned}$$

may all be confused with the photoproduction of J/ψ and must be accounted for. For this purpose we may use the results of previous experiments, the most recent (1987) being that of the NA14 collaboration [24] who quote a value for the ratio of cross sections of ψ' production to J/ψ production as

$$\frac{\sigma_{\psi'}}{\sigma_{J/\psi}} = 0.19 \pm 0.04$$

This result was arrived at from analysis at a lower centre of mass energy to that attainable at HERA of $W_{\gamma p} = 13$ GeV. Preliminary results from H1 analyses [34] quote a figure of 0.20 ± 0.09 evaluated at $W_{\gamma p} = 80$ GeV, suggesting the ratio does not vary to a significant degree with $W_{\gamma p}$. Using the NA14 result and taking the branching ratio of the ψ' to J/ψ plus neutral tracks from table 6.1 to be $\frac{\Gamma_n}{\Gamma} = (23.2 \pm 2.6)\%$, then the percentage of our muon pair sample that can be attributed to this cascade effect is

$$\frac{\sigma_{\psi'}}{\sigma_{J/\psi}} \times \frac{\Gamma_n}{\Gamma} = (0.19 \times 23.2)\% = (4.4 \pm 1.1)\%$$

There are several factors making this small ψ' correction to our J/ψ sample merely an estimate. For instance the contribution of $\psi' \rightarrow \mu^+\mu^-$ events to our signal is neglected. These events have invariant masses around the ψ' nominal mass and therefore lie well outside the mass range that we consider to constitute our

J/ψ signal. Also neglected is the contribution from $\psi' \rightarrow J/\psi + \text{charged particles}$ where these other particles fall outside of detector acceptance. Events from this decay where the particles pass through the sensitive region of the H1 detector are removed by a cut on track multiplicity. It is possible that J/ψ particles produced from ψ' decays have differing angular and momentum distributions than those from photoproduction, hence the analysis efficiency is different for these decays.

6.2 Detector Acceptance

In order to make an accurate cross section measurement, care must be taken to fully understand the efficiency of the H1 detector in accepting events of the type that are sought. Angular limitations imposed by the arrangement of the individual sub-detectors comprising H1 and the beam-pipe must be accounted for, as well as track reconstruction efficiencies and trigger efficiencies of these sub-detectors. The ability of the analysis code to recognise events when they happen must also be understood. Monte Carlo simulation of the elastic production process $\gamma p \rightarrow J/\psi p$ is used for this purpose.

The detector acceptance \mathcal{E} in equation 6.1 can be separated into several individual acceptances as shown in equation 6.2.

$$\mathcal{E} = \mathcal{E}_{GEO} \mathcal{E}_{TRG} \mathcal{E}_{ANA} \quad (6.2)$$

In equation 6.2, \mathcal{E}_{GEO} is the geometric acceptance of the H1 apparatus, \mathcal{E}_{TRG} the trigger efficiency while \mathcal{E}_{ANA} is the acceptance of the cuts outlined in chapter 4 for events to enter our low-multiplicity event sample. Each of these acceptances are examined individually in the following sections.

In order to have faith in the acceptance values obtained in this fashion, it is important to determine how closely the individual components of the H1 detector are modelled by the simulation. Discrepancies and statistical uncertainties in agreement must be accounted for.

This section includes a study of the various sets of selection cuts that have been made on our data sample, namely the quasi-elastic cuts outlined in chapter 4 and the proton-veto cuts mentioned in section 6.1 of this chapter.

6.2.1 Geometric Acceptance

Angular limitations of the H1 detector mean that particles falling outside the sensitive region cannot be detected. Together with the requirement that particles in the backwards region of H1 be reconstructed by the CJC alone, and not the backward proportional chambers, an angular range of $7^\circ < \theta < 160^\circ$ results. Our sensitivity to the photoproduction centre of mass energy $W_{\gamma p}$ is found to lie in the range $30 \text{ GeV} < W_{\gamma p} < 180 \text{ GeV}$, as shown in figure 5.8 of the previous chapter.

As the central and forward trackers each cover different angular ranges, an acceptance for each detector was determined separately. There is however some overlap in the range of $W_{\gamma p}$ covered by these two detectors. The column labelled ‘Forward’ throughout tables in this chapter refers to the case where at least one muon is reconstructed by the Forward Tracker and detected by the various forward muon detectors. Events with at least one combined central/forward track were also labelled ‘Forward’. The $W_{\gamma p}$ and θ limits on this bin were chosen on inspection of their observed distributions in the data. For example figure 5.8 shows the distribution in $W_{\gamma p}$ of muons found in the forward direction falling specifically in the range $30 \text{ GeV} < W_{\gamma p} < 80 \text{ GeV}$. Columns labelled ‘Central’ contain events with both muons found by the Central Tracker and any H1 muon detectors³. The forward bin considers the angular range $7^\circ < \theta < 25^\circ$, while the central bins cover the range $25^\circ < \theta < 160^\circ$.

To determine our geometric acceptance \mathcal{E}_{GEO} , we turn to Monte Carlo generated events. Table 6.2 shows these values for the elastic simulation files for each range of θ and $W_{\gamma p}$ considered. The kinematic range $Q^2 < 4 \text{ GeV}^2$ was also demanded at this stage. In each case the measurement was made using Monte Carlo

³It is possible to link central tracks to both the FMD and the forward endcap of the instrumented iron muon detector, as well as the barrel region and backward endcap.

<i>Parameter</i>	<i>Forward</i>	<i>Central</i>		
Range of θ	$7^\circ < \theta < 25^\circ$	$25^\circ < \theta < 160^\circ$		
Range of $W_{\gamma p}$ (GeV)	$30 \rightarrow 80$	$40 \rightarrow 90$	$90 \rightarrow 120$	$120 \rightarrow 180$
Geometric Acceptance \mathcal{E}_{GEO}	0.440	0.742	0.730	0.420
$\Delta\mathcal{E}_{GEO}$ Statistical Error	3 %	3 %	5 %	6 %
Systematic Uncertainties:				
$\Delta\mathcal{E}_{GEO}$ VMD Model	7 %	1 %	3 %	6 %
$\Delta\mathcal{E}_{GEO}$ Dissociation	5 %	1 %	5 %	3 %
$\Delta\mathcal{E}_{GEO}$ (W, θ) Resolution	1 %	1 %	1 %	1 %
<i>Quadratic Sum</i> $\Delta\mathcal{E}_{GEO}$	9 %	3 %	8 %	8 %

Table 6.2: Geometric acceptances calculated using elastic VMD Monte Carlo where both muons fall in the range $7^\circ < \theta < 160^\circ$ together with their statistical errors. The effects of using simulation of proton dissociation, and with different VMD parameter are also shown. The reconstruction resolution of $W_{\gamma p}$ and θ is also shown. All errors are shown as percentages of the acceptance value for their $W_{\gamma p}$ bin.

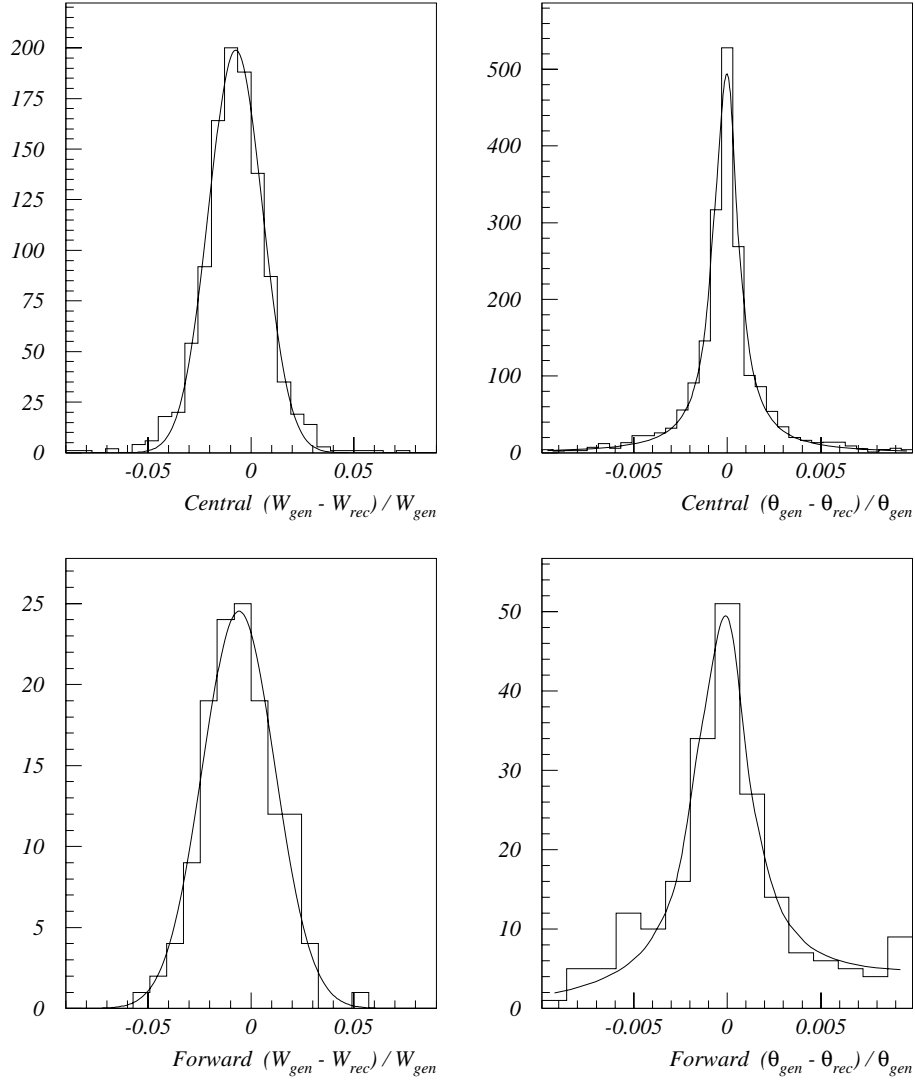


Figure 6.2: Normalised resolutions of the reconstruction of $W_{\gamma p}$ (left hand upper and lower diagrams) and track angle θ (right hand) fitted with Gaussian and Breit-Wigner fits respectively. The upper plots correspond to events containing 2 central tracks, the lower plots for the case where at least 1 forward track is found in the event.

generated with VMD parameters⁴ of $\epsilon = 0.0808$ and also $\epsilon = 0.225$ to assess the systematic effect of our original choice of $\epsilon = 0.0808$. Previous results [23][35][36][37] had suggested that the $W_{\gamma p}$ behaviour of the cross section tended towards the latter higher value. The difference in the $W_{\gamma p}$ distributions for each ϵ value was found to be rather different. Simulation containing the value $\epsilon = 0.0808$ was found to contain proportionally more events at lower $W_{\gamma p}$ values. The systematic error was therefore not thought to be constant with $W_{\gamma p}$ and was accordingly estimated separately for each bin of $W_{\gamma p}$ in our cross section calculation. The systematic effect of repeating the \mathcal{E}_{GEO} calculation using Monte Carlo containing proton dissociation is also shown.

Uncertainties in our reconstruction of the $W_{\gamma p}$ and θ variables is also a factor to be considered. Figure 6.2 shows the reconstruction resolution as a fraction of the generated value, determined from simulation. The fits give standard deviations equivalent to 1% and 0.1% for $W_{\gamma p}$ and θ respectively for the Central Tracker. For the Forward Tracker these numbers are 2% and 0.1% for $W_{\gamma p}$ and θ . Varying the bins of $W_{\gamma p}$ and θ individually by these amounts produces systematic shifts in geometric acceptance. Table 6.2 summarises these findings for each bin of $W_{\gamma p}$.

6.2.2 Trigger Selection

As mentioned in chapter 5, our trigger selection was based upon performance during the running period and their contribution to physics events recorded during 1994. For this reason the Forward Muon Trigger was not used for this analysis. The combination of trigger elements constituting our four chosen sub-triggers at level one are outlined in table 6.3, and are denoted as sub-triggers 18, 19, 22 and 54 in the level 1 numbering scheme.

The trigger element **dcr ϕ -Ta** passes or rejects a track according to the distance of closest approach (DCA) of the track to the beam axis. The **Mu_Bar** trigger element seeks muons penetrating the barrel region of the instrumented iron. The other elements of the sub-triggers are themselves combinations of trigger elements in

⁴In the VMD relation for the cross section $\sigma_{\gamma p} \sim W_{\gamma p}^{4\epsilon}$.

<i>Trigger Element</i>	S18	S19	S22	S54
<i>dcrϕ_Ta</i>	×	×	-	-
<i>dcrϕ_TNeg</i>	-	-	-	×
<i>zVtx_Cls</i>	-	-	-	×
<i>Mu_ECQ</i>	×	-	-	-
<i>Mu_Bar</i>	-	×	-	-
<i>Mu_BEC</i>	-	-	×	-
<i>Topo_BR</i>	-	-	-	×

Table 6.3: Combinations of trigger elements constituting the heavy flavour sub-triggers labelled 18, 19, 22 and 54 at level 1 of the H1 trigger system.

the backward endcap (*Mu_BEC*), and in either forward or backward endcaps (*Mu_ECQ*). The Topological big-ray sub-trigger 54 looks for two tracks back-to-back in angle ϕ with one track having momentum > 0.7 GeV and less than 5 tracks in the event. A big-ray is a pre-defined group of calorimeter cells whose trigger element is denoted *Topo_BR*. The other trigger elements of sub-trigger 54, *zVtx_Cls* and *dcr ϕ _TNeg*, examine the z-vertex and DCA values of a track respectively.

<i>Sub-Trigger</i>	<i>Level 1 Rate (Hz)</i>	<i>Mean Pre-Scale</i>
S18	2	1.09
S19	2	1.14
S22	1	1.12
S54	2.5	1.53

Table 6.4: Mean pre-scales and rates for our chosen sub-triggers during 1994 operation.

The rates of operation and weighted mean pre-scales of these sub-triggers at level 1 during the running period considered in 1994 are shown in table 6.4. The mean pre-scale value was weighted according to the magnitude of run luminosity during each of the 1816 H1 runs considered in the mean value. All of the sub-triggers

performed well during 1994, and ran at reasonable level 1 rates of approximately a few Hz.

For Monte Carlo events it was necessary to use the mean pre-scales for the complete running period when determining detector acceptances, rather than on a run-by-run basis. The systematic effect of this is examined later in the chapter. Monte Carlo events were weighted on a run-by-run basis according to the fraction of each run for which the voltages upon critical detectors were at suitable status, for example that on inner tracking detectors.

6.2.3 Trigger Efficiency

When Monte Carlo is used to simulate full detector response, it is important to test whether this simulation is accurate. One very important factor is whether the trigger response agrees with that seen in data. Any discrepancy must be determined and corrected.

<i>Trigger Element</i>	<i>Data (%)</i>	<i>MoCa (%)</i>	<i>Residual (%)</i>
<i>dcrφ-Ta</i>	81 ± 1	91 ± 1	10 ± 1
<i>dcrφ-TNeg</i>	64 ± 2	74 ± 2	10 ± 3
<i>zVtx-Cls</i>	79 ± 3	84 ± 4	5 ± 5
<i>Mu-ECQ</i>	62 ± 6	69 ± 4	7 ± 7
<i>Mu-Bar</i>	80 ± 3	83 ± 6	3 ± 7
<i>Mu-BEC</i>	70 ± 5	74 ± 5	4 ± 7
<i>Topo-BR</i>	53 ± 3	57 ± 2	4 ± 4

Table 6.5: *Difference between data and Monte Carlo for measured efficiencies of trigger elements dcrφ-Ta, Mu-ECQ, Mu-Bar and Mu-BEC. Only the trigger elements dcrφ-Ta and dcrφ-TNeg display a difference in efficiency greater than statistical error.*

In order to accurately measure the response of any sub-trigger it is important to use a sample of events which were found by a sub-trigger independent of that being studied. Examination of the sub-triggers described in table 6.3 shows

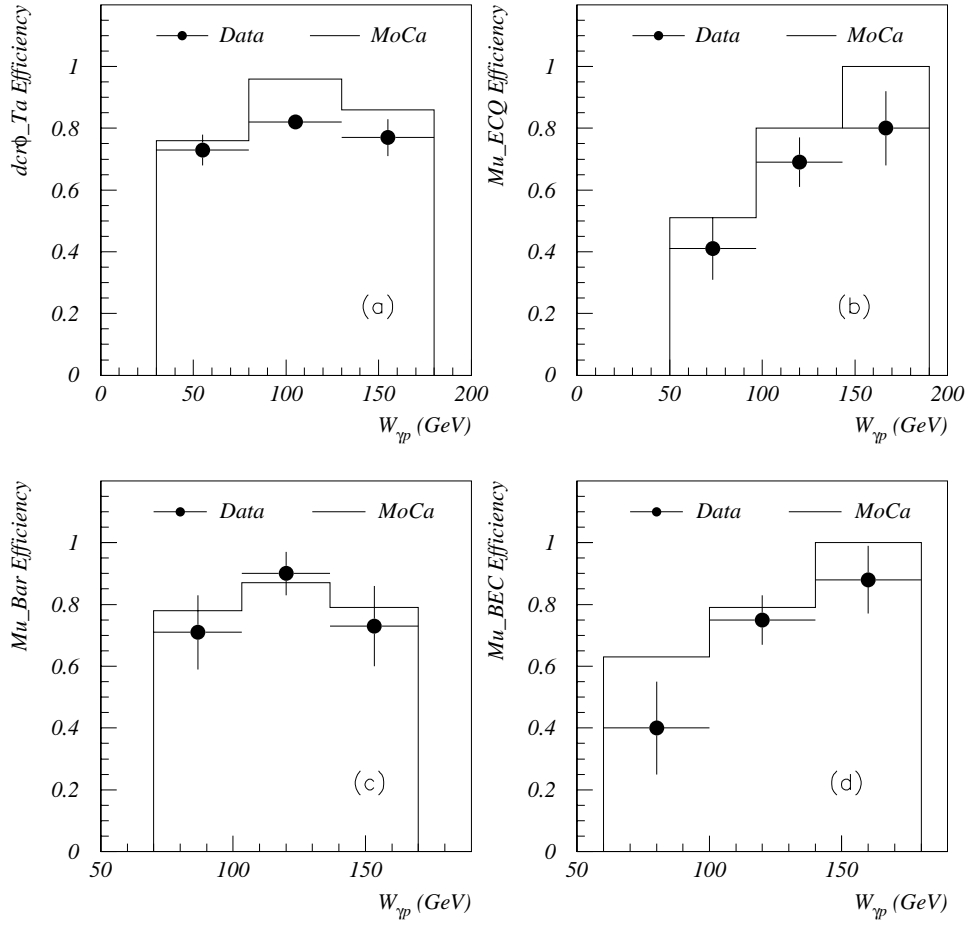


Figure 6.3: Efficiencies shown as a function of $W_{\gamma p}$ for the trigger elements (a) $dcr\phi_Ta$, (b) Mu_ECQ , (c) Mu_Bar and (d) Mu_BEC . The points represent data values, the solid histogram shows simulation values, whose errors are not shown.

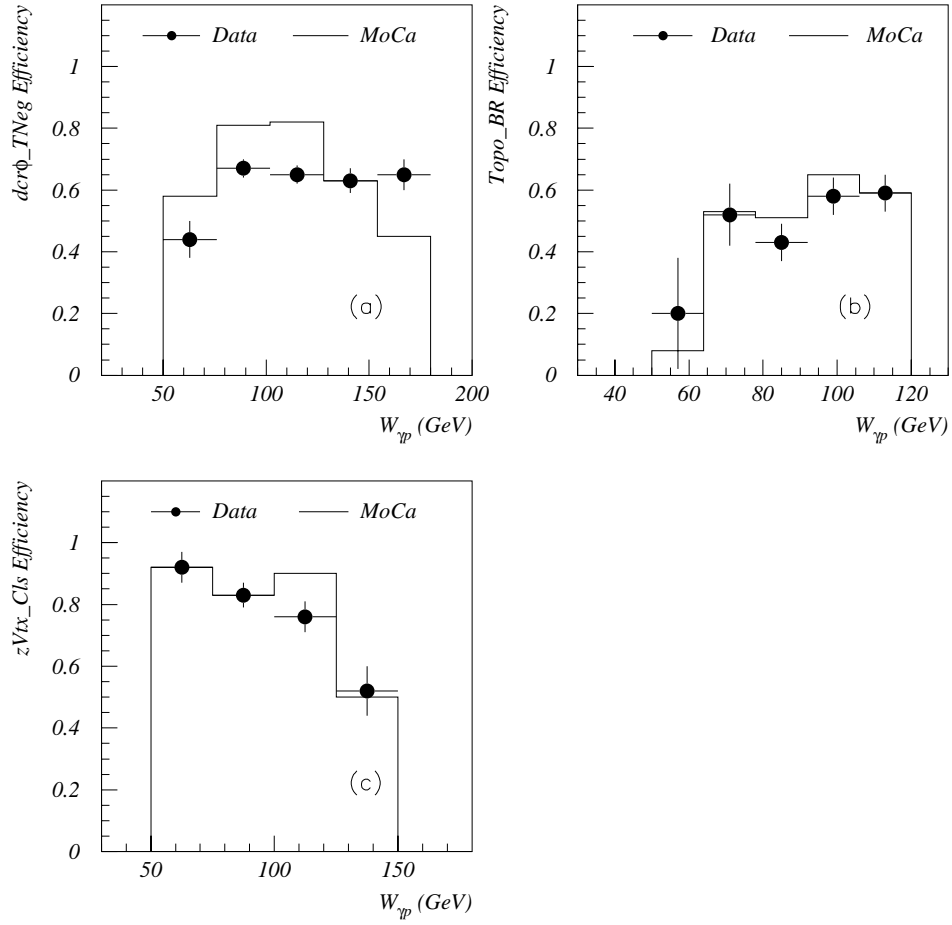


Figure 6.4: Efficiencies shown as a function of $W_{\gamma p}$ for the trigger elements comprising sub-trigger 54, (a) $dcr\phi_TNeg$, (b) $Topo_BR$ and (c) $zVtx_Cls$. The points represent data values, the solid histogram shows simulation values, whose errors are not shown.

<i>Parameter</i>		<i>Forward</i>	<i>Central</i>		
Range of θ		$7^\circ < \theta < 25^\circ$	$25^\circ < \theta < 160^\circ$		
Range of $W_{\gamma p}$ (GeV)		$30 \rightarrow 80$	$40 \rightarrow 90$	$90 \rightarrow 120$	$120 \rightarrow 180$
Trigger Acceptance \mathcal{E}_{TRG}		0.092	0.302	0.529	0.621
$\Delta\mathcal{E}_{TRG}$ MC Statistical Error		7 %	4 %	3 %	3 %
Systematic Uncertainties:					
$\Delta\mathcal{E}_{TRG}$	<i>dcrϕ_Ta</i>	2 %	1 %	1 %	1 %
$\Delta\mathcal{E}_{TRG}$	<i>Mu_Bar</i>	2 %	1 %	2 %	1 %
$\Delta\mathcal{E}_{TRG}$	<i>Mu_ECQ</i>	9 %	3 %	6 %	9 %
$\Delta\mathcal{E}_{TRG}$	<i>Mu_BEC</i>	1 %	1 %	1 %	2 %
$\Delta\mathcal{E}_{TRG}$	<i>dcrϕ_TNeg</i>	1 %	2 %	1 %	1 %
$\Delta\mathcal{E}_{TRG}$	<i>Topo_BR</i>	2 %	3 %	2 %	1 %
$\Delta\mathcal{E}_{TRG}$	<i>zVtx_Cls</i>	1 %	2 %	1 %	1 %
$\Delta\mathcal{E}_{TRG}$	Mean Pre-scales	6 %	4 %	4 %	4 %
<i>Quadratic Sum</i> $\Delta\mathcal{E}_{TRG}$		13 %	8 %	8 %	10 %

Table 6.6: Trigger acceptances calculated using elastic VMD Monte Carlo where both muons fall in the range $7^\circ < \theta < 160^\circ$, together with their statistical error. The effects of using simulation of proton dissociation, and with different VMD parameters are also shown. The reconstruction resolution of $W_{\gamma p}$ and θ is also shown. Errors shown are expressed as percentages of the acceptance values or each $W_{\gamma p}$ bin.

that sub-trigger 22 is independent of any trigger element at the vertex contained in the other sub-triggers, namely *zVtx_Cls*, *dcrφ-Ta* and *dcrφ-TNeg*. It is also independent of the calorimeter trigger element *Topo_BR* and the muon trigger element *Mu_BAR* constituent of sub-trigger 19. Hence, using events found by sub-trigger 22 allows us to test the efficiency of all these other trigger elements independently. To then measure the efficiency of the trigger element *Mu_BEC* constituting sub-trigger 22 itself, events were used that had been triggered by a scattered electron in the BEMC calorimeter (sub-trigger 00), but otherwise resembled an elastic photoproduction event. This was also necessary to examine the *Mu_ECQ* trigger element, which forms part of sub-trigger 18 and uses the backward endcap. Figure 6.3 shows the efficiencies of elements comprising sub-triggers 18, 19 and 22, each shown as a function of the γp centre of mass energy $W_{\gamma p}$. Similar plots for trigger elements comprising sub-trigger 54 are shown in figure 6.4.

The combined efficiency for events being found by a logical inclusive OR of our set of four sub-triggers, denoted \mathcal{E}_{TRG} , is determined from simulation. The effect on \mathcal{E}_{TRG} of the simulation of each trigger element must be examined. If significant discrepancy between data and simulation of the efficiency of a trigger element is found, the effect of this upon the sub-trigger it belongs to is assessed. The sub-trigger efficiency is then artificially corrected by this amount by adjusting the pre-scale factor of that sub-trigger in the simulation. Corrections of this type were done where necessary for each trigger element.

If agreement is found between data and Monte Carlo within statistical error then no correction is done. However, the statistical uncertainty on the agreement found constitutes an uncertainty on \mathcal{E}_{TRG} . The effect of the statistical uncertainty of the agreement for each trigger element on its sub-trigger efficiency is found, and the effect of this in turn on \mathcal{E}_{TRG} determined for each trigger element. The systematic effects on \mathcal{E}_{TRG} for the uncertainty on each trigger element are then added in quadrature.

Table 6.5 shows the efficiencies of all seven trigger elements that were studied, calculated across the entire range of $W_{\gamma p}$. It can be seen that only *dcrφ-Ta*

and `dcr ϕ _TNeg` show a statistically significant discrepancy between simulation and data. These were corrected for using the method outlined earlier. The acceptance of the combined sub-trigger selection \mathcal{E}_{TRG} is shown in table 6.6. The systematic effects of each trigger element on \mathcal{E}_{TRG} is also shown. Also included in the table is the effect of using mean rather than run-by-run pre-scale factors for the calculation \mathcal{E}_{TRG} in simulation, determined from the spread of the distribution of the pre-scales over the entire running period.

6.2.4 Selection Efficiency

Once we have an event sample triggered by our sub-trigger combination, the series of cuts outlined in chapter 4 to ensure data quality and also to remove some degree of inelastic events will reduce this data sample still further. This leaves us with a quasi-elastic low multiplicity sample before further cuts on the proton remnant outlined in section 6.1 of this chapter. The acceptance of these proton-veto cuts are examined later. The acceptance of the data quality cuts (\mathcal{E}_{ANA}) is something that must be determined as a function of $W_{\gamma p}$. In measuring this acceptance from Monte Carlo events, care must again be taken to ensure that the simulation describes the data accurately, with corrections applied and systematic uncertainties evaluated in the same manner as was done for \mathcal{E}_{GEO} and \mathcal{E}_{TRG} .

Figure 6.5 shows the efficiency of the detectors used in this analysis to find muon candidates, namely the LAr calorimeter and the instrumented iron. The efficiency is measured for finding muons according to our muon track quality cuts from section 4.1, and is determined from both data and simulation. The right hand plot of figure 6.5 shows the likelihood of finding a muon cluster in the LAr calorimeter with quality index 2 or higher, while the left hand diagram shows the acceptance of the instrumented iron detector according to the event class ECMUON cuts outlined in chapter 4. In both plots the solid histogram represents simulation, the points represent data. These values were measured by making a separate event sample in which we require only one identified muon candidate in either the calorimeters or the iron detectors, with exactly two tracks comprising the inner tracks of the event.

A cut was made on the invariant mass (M) of the track pair around the nominal J/ψ mass, namely $2.7 \text{ GeV} < M < 3.4 \text{ GeV}$. The response of the LAr calorimeter and the instrumented iron to the other muon is then used to determine the efficiency of these muon detectors. Table 6.7 shows the residual between data and simulation for this procedure, corresponding to the plots of figure 6.5 integrated over their ranges of $W_{\gamma p}$. Both are found to agree within the statistical error of the comparison. The large uncertainties on the measured efficiency of the instrumented iron detector is due to the comparatively poor statistics for this measurement.

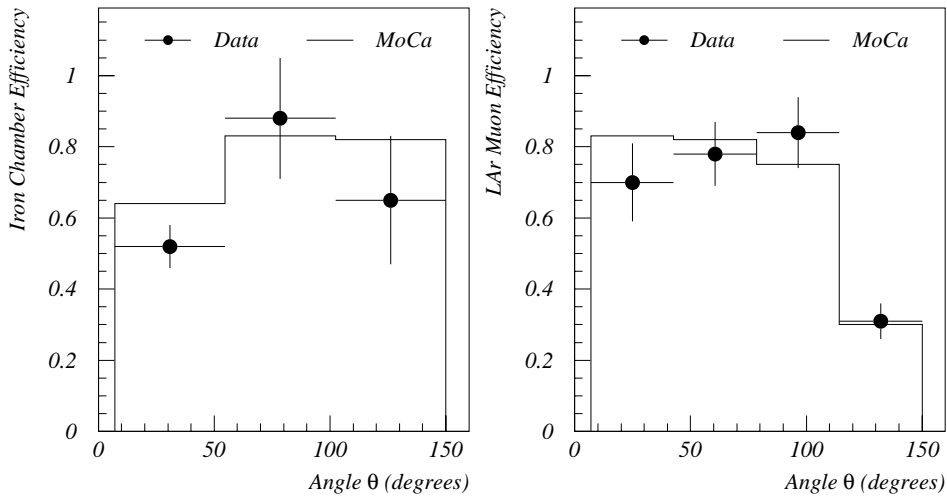


Figure 6.5: Efficiencies of the instrumented iron detector (left hand diagram) and the muon-finding routine of the LAr calorimeter. The solid histogram shows Monte Carlo simulation, the points data. Errors on the simulated values are not displayed.

Table 6.7 also shows the difference between data and Monte Carlo for the efficiency of the Forward Tracker. The efficiency was calculated in both cases for the angular range $7^\circ < \theta < 25^\circ$ and corresponds to sections of the plots contained in figure 5.4. This time the simulation did not accurately describe the data and so correction factors were used to compensate for this effect when obtaining our selection efficiency \mathcal{E}_{ANA} from simulation. The systematic errors from this study are contained in tables 6.7 and 6.8.

<i>Detector</i>	<i>Data (%)</i>	<i>MoCa (%)</i>	<i>Residual (%)</i>
Instrumented Iron	62 ± 7	66 ± 3	4 ± 8
LAr Calorimeter	65 ± 4	69 ± 2	4 ± 4
Forward Tracker	57 ± 3	68 ± 1	11 ± 3

Table 6.7: Comparison of data and simulation of the detection efficiencies of the two muon identification methods used for this analysis, and also the Forward Tracker.

<i>Parameter</i>	<i>Forward</i>	<i>Central</i>		
Range of θ	$7^\circ < \theta < 25^\circ$	$25^\circ < \theta < 160^\circ$		
Range of $W_{\gamma p}$ (GeV)	$30 \rightarrow 80$	$40 \rightarrow 90$	$90 \rightarrow 120$	$120 \rightarrow 180$
Analysis Acceptance \mathcal{E}_{ANA}	0.403 %	0.353 %	0.462 %	0.362 %
$\Delta\mathcal{E}_{ANA}$ MC Statistical Error	12 %	9 %	8 %	9 %
Systematic Uncertainties:				
$\Delta\mathcal{E}_{ANA}$ LAr Muon Finder	2 %	3 %	7 %	3 %
$\Delta\mathcal{E}_{ANA}$ Instrumented Iron	8 %	9 %	9 %	5 %
$\Delta\mathcal{E}_{ANA}$ Forward Tracker	6 %	-	-	-
<i>Quadratic Sum</i> $\Delta\mathcal{E}_{ANA}$	16 %	13 %	14 %	11 %

Table 6.8: Analysis acceptances calculated using elastic VMD Monte Carlo where both muons fall in the range $7^\circ < \theta < 160^\circ$. The systematic errors due to simulation of the Forward Tracker and muon detectors are also shown.

6.2.5 Proton Veto Cuts

In section 6.1.1 of this chapter, a series of cuts were outlined which were designed to remove much of the remaining events displaying proton dissociation from the low-multiplicity event sample formed thus far. In order to evaluate the full extent of contamination, Monte Carlo files were used which simulated proton dissociation in diffractive J/ψ production. Table 3.2 shows the generated properties of these files, and also the simulation files of the purely elastic process in more detail.

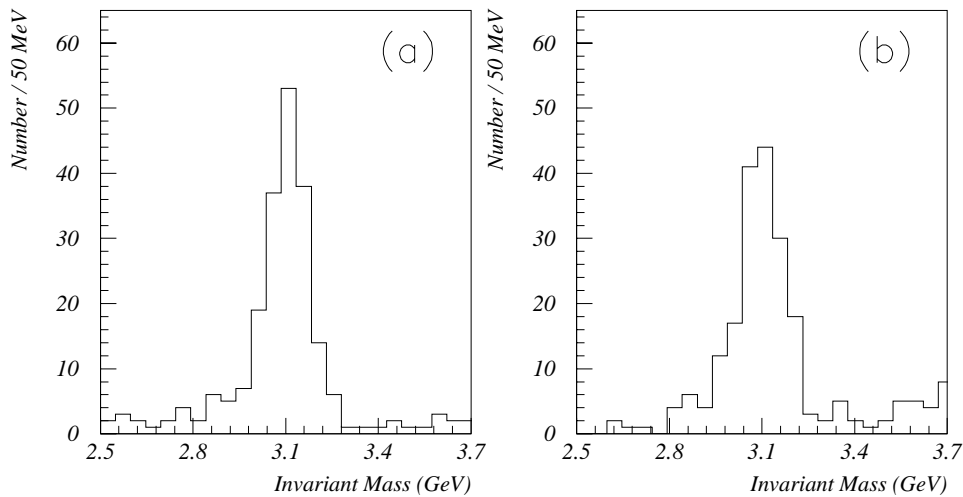


Figure 6.6: *Invariant mass distributions (a) all pairs in elastic data class X, (b) events failing elastic cuts thus belonging to class Y.*

The data may be separated into two classes according to whether events pass or fail our cuts on the remnant proton. These classes are labelled X and Y respectively, with figure 6.6 showing invariant mass plots for each class. The mass peak for class X corresponds to that shown in figure 6.1. The number of events under Gaussian fits to each mass plot are 163.0 ± 14.1 and 139.5 ± 13.3 for samples X and Y respectively. The acceptances of our cuts in finding events of each class can be found by using the simulation. Equations 6.3 show these acceptances which

are labelled \mathcal{E}_{class}^{MC} according to the Monte Carlo (MC) used (elastic or dissociative) and the data class considered (X or Y). For example the acceptance of finding class X events in dissociative Monte Carlo simulation is labelled \mathcal{E}_X^{diss} . It should be noted that for each Monte Carlo considered $\mathcal{E}_X^{MC} + \mathcal{E}_Y^{MC} = 1$.

$$\begin{aligned} N_X &= \mathcal{E}_X^{elas} N_X^{corr} + \mathcal{E}_X^{diss} N_Y^{corr} \\ N_Y &= \mathcal{E}_Y^{elas} N_X^{corr} + \mathcal{E}_Y^{diss} N_Y^{corr} \end{aligned} \quad (6.3)$$

Parameter	Forward	Central		
		Range of $W_{\gamma p}$	30 \rightarrow 80	40 \rightarrow 90
\mathcal{E}_X^{elas}	0.8538	0.9713	0.9808	0.9766
\mathcal{E}_Y^{elas}	0.1462	0.0287	0.0192	0.0234
\mathcal{E}_X^{diss}	0.2034	0.1649	0.1522	0.1600
\mathcal{E}_Y^{diss}	0.7966	0.8352	0.8479	0.8400
$\Delta \mathcal{E}_X^{elas}$	4 %	4 %	4 %	4 %
$\Delta \mathcal{E}_X^{diss}$	20 %	20 %	20 %	20 %
$\Delta \mathcal{E}_Y^{elas}$	4 %	4 %	4 %	4 %
$\Delta \mathcal{E}_Y^{diss}$	20 %	20 %	20 %	20 %
N_X	14.5 ± 4.2	57.5 ± 8.5	51.1 ± 8.7	35.7 ± 7.2
N_Y	17.0 ± 5.0	52.1 ± 8.3	33.2 ± 7.2	41.0 ± 7.4
N_X^{corr}	12.4	48.9	46.2	28.7
ΔN_X^{corr} (stat.)	5.4	9.0	9.0	7.5
ΔN_X^{corr} (syst.)	2.4	5.0	3.2	3.6

Table 6.9: Values of acceptances of the proton-veto cuts applied to the data sample for each bin of $W_{\gamma p}$, denoted \mathcal{E}_{class}^{MC} . The values labelled $\Delta \mathcal{E}_{class}^{MC}$ are estimates of the systematic uncertainties of these cuts. The number of events in class X and Y are denoted N_X and N_Y and are quoted with their statistical error. The value of N_X corrected for dissociative events is labelled N_X^{corr} and is quoted together with its statistical and systematic errors.

Once we have determined the various acceptances \mathcal{E}_{class}^{MC} of equations 6.3, we solve these equations simultaneously for N_X^{corr} , the corrected number of elastic events, i.e. the number of purely elastic events in sample X after removal of dis-

sociative events. This number corresponds to variable N in equation 6.1 for the calculation of the elastic cross section σ_{ep}^{elas} . Table 6.9 shows the values of the acceptances of equations 6.3 for various ranges of the variable $W_{\gamma p}$, together with a summary of the numbers N_X , N_Y and N_X^{corr} for the same $W_{\gamma p}$ bins. Since we are interested only in the elastic cross section, a value for N_Y^{corr} is not relevant. The systematic errors on the values of \mathcal{E}_{class}^{MC} are quoted in table 6.9 as 4 % for elastic simulation and 20 % for proton-dissociative Monte Carlo. The determination of these uncertainties is presented elsewhere [36] for the same set of proton veto cuts used for this analysis. They are obtained from a study of the simulation of various detectors used to tag the proton, and uncertainty in the simulation of the proton remnant in dissociative events. The resultant systematic error on the value of N_X^{corr} for each bin is done by a covariance method, and is outlined in appendix A.

6.3 Luminosity and Branching Ratio

The final parameters of equation 6.1 to be determined are the total 1994 integrated luminosity and the branching ratio of the J/ψ meson to a di-muon pair. The luminosity to be used in the calculation is the sum total accepted by H1 from that delivered by HERA. Only data from the e^+p running period were considered. The luminosity accepted in each run was suitably corrected and the sum total determined for all runs considered. The factors considered in this process are listed below.

- Critical detectors were included in the detector readout.
- Background removal via non-colliding satellite bunches.

Taking these two corrections into account, the integrated luminosity is evaluated at 2.89 pb^{-1} between runs 82961 and 90419, with a systematic error of 1.48 % [38]. The major sources of this systematic error are from uncertainties in satellite bunch correction and the performance of the luminosity system. For test purposes, a fraction of the 1994 running period had collisions at a vertex position

shifted towards positive z . These data were not considered for this analysis or for the luminosity calculation. This luminosity figure is to be compared with the luminosity of 4.98 pb^{-1} delivered by HERA during the same running period. The branching ratio of $J/\psi \rightarrow \mu^+ \mu^-$ that was used for our calculation was the currently accepted [16] value of $(5.97 \pm 0.25) \%$, whose quoted error corresponds to a systematic uncertainty of 4.19%. It is appropriate to add these systematic uncertainties across the entire range of $W_{\gamma p}$ bins.

Table 6.10 shows a summary of all values measured thus far and the values of the ep cross section σ_{ep} . In order for comparison to be made between our results and those of lower energy collider experiments, it is necessary to convert our measurements into photoproduction cross sections by considering the flux of photons emitted by the electron beam.

6.4 Photon Flux

A good approximation for converting the cross section σ_{ep} into a photoproduction cross section $\sigma_{\gamma p}$ is made by multiplying by a factor relating to the probability of the electron emitting a photon at the $e \rightarrow e\gamma^*$ vertex. This notion is shown in equation 6.4,

$$\sigma_{ep}(y, Q^2) = \int_{y_{min}}^{y_{max}} \int_{Q_{min}^2}^{Q_{max}^2} f_{\gamma/e}(y, Q^2) \sigma_{\gamma p}(y, Q^2) dy dQ^2 \quad (6.4)$$

where $f_{\gamma/e}(y, Q^2)$ describes the photon flux emitted by the electron [39][40]. For events of the type we are considering it is appropriate to use the Weizsäcker-Williams approximation [41] for the flux factor of the form given in equation 6.5, where contribution from longitudinal flux can be neglected for events with $Q^2 \rightarrow 0$ as in our case.

$$f_{\gamma/e}^T = \frac{\alpha}{2\pi} \frac{1}{Q^2} \left[\frac{1 + (1-y)^2}{y} - \frac{2m_e^2 y}{Q^2} \right] \quad (6.5)$$

<i>Parameter</i>	<i>Forward</i>	<i>Central</i>		
Range of $W_{\gamma p}$	30 \rightarrow 80	40 \rightarrow 90	90 \rightarrow 120	120 \rightarrow 180
N_X^{corr}	12.4	48.9	46.2	28.7
ψ' Corrected	11.9	46.7	44.2	27.4
\mathcal{E}_{GEO}	0.440	0.742	0.730	0.420
\mathcal{E}_{TRG}	0.092	0.302	0.529	0.621
\mathcal{E}_{ANA}	0.403	0.353	0.462	0.362
\mathcal{E}_{TOT}	0.016	0.079	0.178	0.094
Luminosity \mathcal{L} (nb $^{-1}$)	2891			
Branching Ratio B	0.0597			
σ_{ep} (nb)	4.3	3.4	1.4	1.7

Statistical Error	ΔN_X^{corr}	43 %	18 %	19 %	26 %
Systematic Error:					
Proton Veto Cuts	ΔN_X^{corr}	19 %	10 %	7 %	12 %
Geometric	$\Delta \mathcal{E}_{GEO}$	9 %	3 %	8 %	8 %
Trigger	$\Delta \mathcal{E}_{TRG}$	13 %	8 %	8 %	10 %
Analysis	$\Delta \mathcal{E}_{ANA}$	16 %	13 %	14 %	11 %
ψ' Correction		1.15 %			
Luminosity	$\Delta \mathcal{L}$	1.48 %			
Branching Ratio	ΔB	4.19 %			
$\Delta \sigma_{ep}$	Statistical	43 %	18 %	19 %	26 %
$\Delta \sigma_{ep}$	Systematic	30 %	19 %	20 %	21 %

Table 6.10: Cross section σ_{ep} for the kinematic region $Q^2 < 4 \text{ GeV}^2$. The parameters used in the calculation are shown in the upper table. A summary of the statistical and systematic errors encountered in the calculation is given in the lower table.

In equation 6.5, m_e represents the electron mass and α the fine-structure constant. The limits of the integrals shown in equation 6.4 come directly from the kinematics. The minimum value of Q^2 available is $Q_{min}^2 = m_e^2 \left(\frac{y^2}{1-y} \right)$, the upper limit of $Q_{max}^2 = 4 \text{ GeV}^2$ comes from our requirement that the scattered electron is not detected in the main H1 calorimeters. The limits on the y integral are taken from the ranges of $W_{\gamma p}$ considered for each of the bins of our cross section, and equation 6.6 which relates $W_{\gamma p}$ and y .

$$W_{\gamma p}^2 = sy + m_p^2 - m_e^2 \left(\frac{y^2}{1-y} \right) \simeq sy \quad (6.6)$$

The integral of the flux factor $f(y, Q^2)$ has been calculated as 0.156 across the full range $30 \text{ GeV} < W_{\gamma p} < 180 \text{ GeV}$. The integral values were also calculated for the ranges of each of the individual $W_{\gamma p}$ bins of our σ_{ep} cross section measurement. These are shown in table 6.11, which also displays the resulting values of $\sigma_{\gamma p}$.

There is a small effect upon the measured cross section value $\sigma_{\gamma p}$ owing to its y dependence and also that of the photon flux. To account for this effect one may either make a correction to the flux value calculated per bin and hence to the resulting $\sigma_{\gamma p}$ cross section, or instead correct the central $W_{\gamma p}$ value at which $\sigma_{\gamma p}$ is measured. It is the latter approach that is adopted here. Table 6.11 shows both original bin centres of each $W_{\gamma p}$ range considered, and values adjusted using a value of $\epsilon = 0.225$ in the $W_{\gamma p}$ (and therefore \sqrt{y}) dependence of the $\sigma_{\gamma p}$ cross section.

Figure 6.7 compares our results with those obtained at previous lower energy experiments, and also previous results from both H1 and ZEUS. The dashed and solid lines show the predicted rise of the cross section according to values of $\epsilon = 0.0808$ and $\epsilon = 0.225$ respectively in the relation $\sigma_{\gamma p} \sim W_{\gamma p}^{4\epsilon}$. The data point to which both functions are normalised is the E516 data point of the FTPS collaboration [18] to which our Monte Carlo parameters were also normalised (see table 3.2). This fixed target γp experiment successfully measured the elastic cross section by studying the recoil proton. Also, their cuts on inelasticity best resembled those of this analysis, with a cut on the z variable at $0.9 < z < 1.0$. Results from other experiments are also shown, namely the E687, EMC and E401 collaborations [19][42][43].

All previous results have been corrected with updated branching ratios [16] of the J/ψ into the final state detected at each experiment. Tables of data values from these experiments are documented elsewhere [44].

<i>Parameter</i>	<i>Forward</i>	<i>Central</i>		
Range of $W_{\gamma p}$ (GeV)	30 \rightarrow 80	40 \rightarrow 90	90 \rightarrow 120	120 \rightarrow 180
$W_{\gamma p}$ Central (GeV)	55	65	105	150
$W_{\gamma p}$ Corrected (GeV)	50	61	104	146
σ_{ep} (nb)	4.3	3.4	1.4	1.7
Flux Factor	0.098	0.078	0.023	0.024
$\sigma_{\gamma p}$ (nb)	43.9	43.6	60.9	70.8
$\Delta\sigma_{\gamma p}$ (stat.)	43 %	18 %	19 %	26 %
$\Delta\sigma_{\gamma p}$ (syst.)	30 %	19 %	20 %	21 %

Table 6.11: Photoproduction cross sections calculated for each bin of $W_{\gamma p}$. The bin centre values of $W_{\gamma p}$ are also shown.

From figure 6.7 it is seen that the soft \mathcal{P} model with $\epsilon = 0.0808$ is insufficient to describe the data at HERA energy. A relationship of the same form ($\sigma_{\gamma p} \sim W_{\gamma p}^{4\epsilon}$) though with a value of $\epsilon = 0.225$ shown as the solid line of figure 6.7 better represents the data. A fit to the 1994 central and forward points and the E516 point gives a relationship $\sigma_{\gamma p} \sim W_{\gamma p}^{0.88 \pm 0.04}$ which gives a corresponding measured value of $\epsilon = 0.22 \pm 0.01$. The 1993 ZEUS and H1 data points were not included in this measurement as they both contained unknown contamination from inelastic events.

If a QCD inspired model were to be the mechanism behind J/ψ production, we should expect equation 3.7 to hold, which read $\sigma_{\gamma p} \sim [xg(x)]^2$. This model would describe the data if $g(x)$ were to rise with decreasing x , i.e. increasing $W_{\gamma p}$ as equation 3.8 shows that $x \sim \frac{1}{W_{\gamma p}^2}$. Such a rise in $g(x)$ has been reported by other HERA analyses [45][46][47].

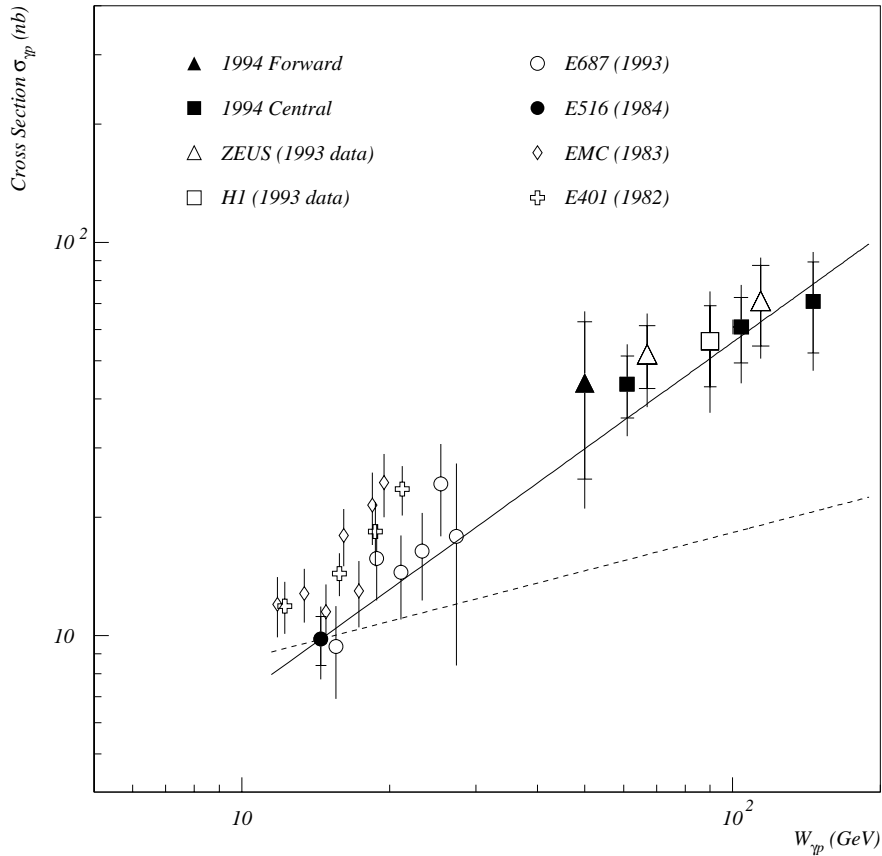


Figure 6.7: Elastic J/ψ photoproduction cross section shown as a function of $W_{\gamma p}$. Results from previous experiments are included. The lines represent functions normalised to the E516 data point and correspond to VMD models with values of $\epsilon = 0.0808$ (dashed line) and $\epsilon = 0.225$ (solid line). The other data include various experiments at lower energy to HERA and also the published H1 and ZEUS results from 1993 running.

6.5 Slope Parameter

In chapter 3 the behaviour of the photoproduction cross section was examined as a function of centre of mass energy $W_{\gamma p}$ according to the diffractive model VMD. Should a VMD model be the underlying mechanism of J/ψ photoproduction, we would expect the first of equations 3.6 to hold, repeated as equation 6.7.

$$\frac{d\sigma_{el}}{dt} \propto e^{-bt} \quad (6.7)$$

According to a VMD model, the parameter b in equation 6.7 varies with increasing $W_{\gamma p}$ according to relation 6.8, where $\alpha'_P = 0.25 \text{ GeV}^{-2}$ for a soft pomeron model. Using this value, equation 6.8 predicts a rise in b measured at $W_{\gamma p}$ from values normalised to b_0 at W_0 .

$$b = b_0 + 4\alpha'_P \ln \left(\frac{W_{\gamma p}}{W_0} \right) \quad (6.8)$$

We can approximate the t -channel momentum transfer shown in equation 6.7 by the magnitude of the transverse momentum of the J/ψ , as described in section 3.3. This approximation is valid for $p_t < 1 \text{ GeV}^2$ only, the reasoning for this is as follows. It is only for the elastic case where the elasticity variable $z = 1$ that the γp centre of mass frame is co-linear with the beam axis. Only in this case is the p_t^2 of the J/ψ equal to the t -channel momentum transfer squared. As Q^2 rises above $Q^2 \sim 1$ this frame and the beam axis are no longer co-linear and the approximation becomes invalid. The p_t^2 of the J/ψ is then gained not only from t -channel momentum transfer but also from Q^2 , the 4-momentum transfer squared of the photon between electron and proton. In the low p_t region the dominant contribution is from events whose $Q^2 \rightarrow 0$.

Measured values of b quoted by previous experiments [18][20][48] are rather inconsistent varying between 1 GeV^{-2} and 5 GeV^{-2} . A value of $(5.0 \pm 2.0) \text{ GeV}^{-2}$ was measured by the E516 experiment [18], whose results have already been used for

normalisation of our cross section measurement in figure 6.7 as this experiment measured the purely elastic process. Reasons for the inconsistency in lower energy data are possibly due to varying experimental conditions and differing levels of contamination from inelastic processes. According to equation 6.8 with $\alpha'_p = 0.25 \text{ GeV}^{-2}$ and normalising to $b_0 = 5 \text{ GeV}^{-2}$ at $W_0 = 14 \text{ GeV}$ we should expect, at a measured mean HERA energy of $\langle W_{\gamma p} \rangle \simeq 90 \text{ GeV}$, a slope parameter of $b \simeq 7 \text{ GeV}^{-2}$.

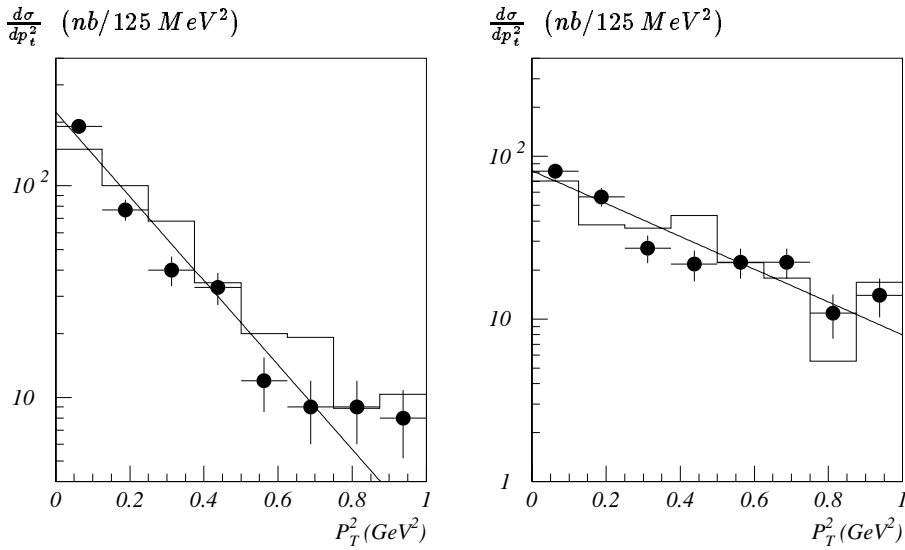


Figure 6.8: Slope parameter measurements. Distributions of $\frac{d\sigma}{dp_t^2}$ against p_t^2 are shown, where the points represent elastic data sample X (left hand diagram) and sample Y (right hand). The full histograms correspond to elastic and proton dissociation simulated events respectively.

Figure 6.8 shows distributions of $\frac{d\sigma}{dp_t^2}$ against p_t^2 for both sample X and sample Y. The solid histograms of each plot represent simulation, whose b values are $b = 4 \text{ GeV}^{-2}$ for the elastic case and $b = 2 \text{ GeV}^{-2}$ for proton-dissociative Monte Carlo. These simulation files are different to those listed in table 3.2, with the growth of b with $W_{\gamma p}$ not modelled. This enables simple comparison of these fixed values with those measured from data. The fits to the data shown in the plots are log-likelihood exponentials of the form e^{-bt} . The slope of the fit is measured for sample X as $(4.6 \pm 0.3 \pm 0.3) \text{ GeV}^{-2}$ in the region of $p_t^2 < 1 \text{ GeV}^2$. The first error

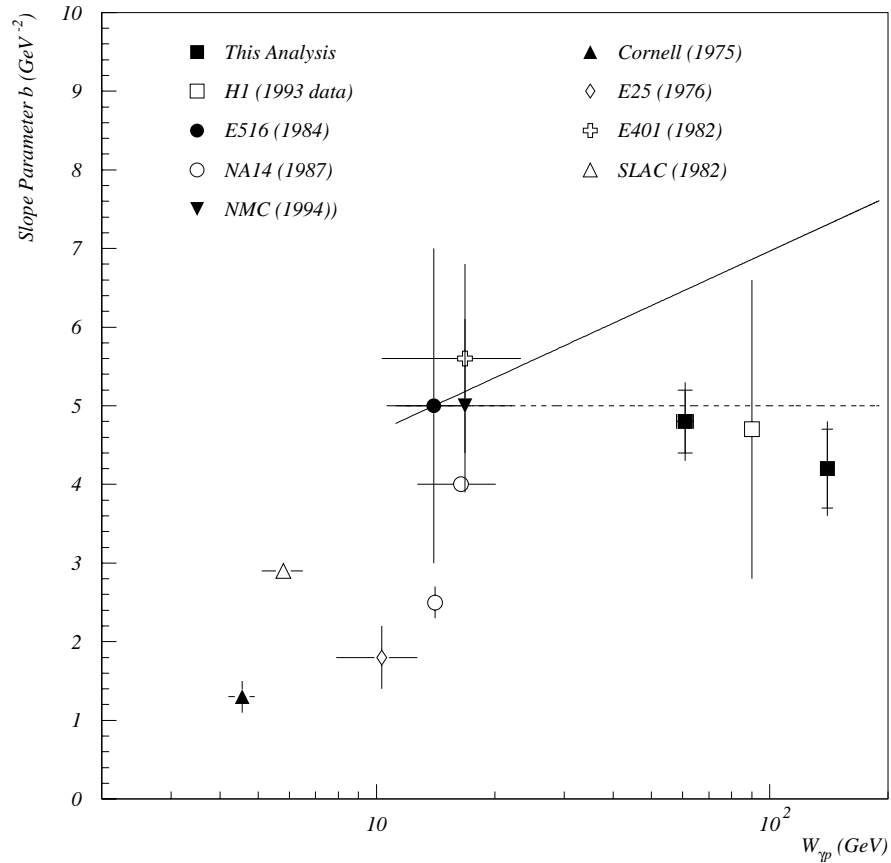


Figure 6.9: J/ψ elastic slope parameters. The solid line represents the predicted rise according to soft pomeron theory, normalised to the E516 data point. The dashed line represents the case of zero shrinkage of the b parameter, also normalised to the same point. Inconsistency of results at lower $W_{\gamma p}$ than HERA is apparent.

quoted on this number is statistical, the second systematic. Systematic error was assessed by varying the binning of the fitted distribution, using a χ^2 exponential fit, and also by altering the limits of the fit to the distribution between $p_t^2 < 0.75 \text{ GeV}^2$ and $p_t^2 < 1.25 \text{ GeV}^2$. This result compares favourably with the result obtained with poorer statistics from 1993 H1 data of $(4.7 \pm 1.9) \text{ GeV}^{-2}$ quoted at $|t| < 0.75 \text{ GeV}^2$, and like this result contains some degree of inelastic contamination. The distribution of the data comprising sample Y is found to have a somewhat shallower slope parameter of $(2.6 \pm 0.3 \pm 0.3) \text{ GeV}^{-2}$.

Range of $W_{\gamma p}$ (GeV)	30 \rightarrow 110	110 \rightarrow 180
Bin Centre $W_{\gamma p}$ (GeV)	70	145
Slope Parameter (GeV^{-2})	$4.8 \pm 0.4 \pm 0.3$	$4.2 \pm 0.5 \pm 0.3$

Table 6.12: Values of the slope parameter measured at lower and higher ranges of $W_{\gamma p}$. The first errors quoted are statistical, the second systematic. No evidence for increase of this parameter with increasing $W_{\gamma p}$ is found, with both values agreeing with the value of $(4.6 \pm 0.3 \pm 0.3) \text{ GeV}^{-2}$ measured across the entire range of $W_{\gamma p}$.

The measured value for sample X falls short of the predicted rise for elastic VMD production via soft \mathbb{P} interchange according to equation 6.8 and our choice of normalisation. However due to the inconsistency of previous results, and also the small level (measured as $\sim 14\%$) of contamination in sample X from dissociative events, it is not conclusive whether this total result constitutes deviation from the prediction of the soft pomeron. For instance normalisation of equation 6.8 to other low energy results for b_0 rather than that quoted by E516 could make our mean slope parameter consistent with a soft \mathbb{P} rise, as is apparent from figure 6.9. The large quoted error on the E516 data point ($\approx 40\%$) also questions any deviation from soft \mathbb{P} theory. The other data shown in figure 6.9 are from the NMC, NA14, E401 and E25 collaborations [20][24][43][49] as well as experiments at SLAC [43] and Cornell [48].

It is possible to test for evolution of the b parameter across the large range of $W_{\gamma p}$ available at HERA of $30 \rightarrow 180$ GeV. Table 6.12 shows measured values of b in two separate energy ranges, $30 \text{ GeV} < W_{\gamma p} < 110 \text{ GeV}$ and $110 \text{ GeV} < W_{\gamma p} < 180 \text{ GeV}$. The values are found to agree with each other within statistical error and therefore no evidence for an increase of b with $W_{\gamma p}$ is observed. Equation 6.8 with a soft \mathbb{P} value of $\alpha'_{\mathbb{P}} = 0.25 \text{ GeV}^{-2}$ predicts a rise in b of 0.7 GeV^{-2} between values measured at $W_{\gamma p} = 70 \text{ GeV}$ and $W_{\gamma p} = 145 \text{ GeV}$, the central values of the upper and lower energy ranges. These values are shown in figure 6.9 which also shows the inconsistency of previous measurements at lower energy including the E516 value of $b = (5 \pm 2) \text{ GeV}^{-2}$. This lack of growth with $W_{\gamma p}$ is probably due to the fact that the soft pomeron does not describe the data. It is interesting to note here that QCD-inspired models of J/ψ production do not predict any rise in b as a function of $W_{\gamma p}$.

Chapter 7

Summary

The elastic photoproduction cross section of the J/ψ meson has been measured from ep interactions via the decay $J/\psi \rightarrow \mu^+ \mu^-$. The measurement was made across a range of $W_{\gamma p}$ of 30 to 180 GeV, with the values obtained listed below.

$$\sigma(\gamma p \rightarrow J/\psi p) = \begin{cases} (44 \pm 19 \pm 13) \text{ nb} & \text{for } W_{\gamma p} = 50 \text{ GeV} \\ (44 \pm 8 \pm 8) \text{ nb} & \text{for } W_{\gamma p} = 61 \text{ GeV} \\ (61 \pm 12 \pm 12) \text{ nb} & \text{for } W_{\gamma p} = 104 \text{ GeV} \\ (71 \pm 18 \pm 15) \text{ nb} & \text{for } W_{\gamma p} = 146 \text{ GeV} \end{cases} \quad (7.1)$$

The soft \mathbb{P} has been found to be insufficient to describe the rise in the cross section from data at lower centre of mass energy. It is possible to parameterise the rise with the dependence $\sigma \sim W_{\gamma p}^{4\epsilon}$ with a measured value of $\epsilon = 0.22 \pm 0.01$ rather than that of $\epsilon = 0.0808$ used to describe previous data at lower γp energy. The rise can be described by perturbative QCD calculations with a rise of the gluon density of the proton at low x values. A measurement of the slope parameter of the relation $\frac{d\sigma}{dt} = e^{-bt}$ in the region $p_t^2 \leq 1 \text{ GeV}^2$ of $b = (4.6 \pm 0.3 \pm 0.3) \text{ GeV}^{-2}$ was found to agree with the corresponding measurement from 1993 H1 data [23]. This value is found to be lower than that of around 7 GeV^{-2} predicted by soft pomeron theory normalised to lower photoproduction energy. No rise of the parameter b governing the t -channel dependence of the cross section was found in the HERA energy range.

It should be noted that a soft pomeron describes very well the comparatively moderate rise in the cross sections of the lighter vector mesons, such as the $\rho(776)$, $\omega(783)$ and $\phi(1020)$ combinations of the (u,d,s) quarks. This is also true for recent measurements of the total photoproduction cross section [50] at the HERA energy range. It is possible we are witnessing the transition to a perturbative regime at the higher mass of the charm quark. Further work at higher integrated luminosities will seek to understand fully the mechanism by which J/ψ mesons are produced.

The forward direction has been used for the first time for analysis of this type, and was found to be of use for both detection of the J/ψ decay muons, and also as a veto of dissociative production by tagging the remnant proton. A study of momentum loss and multiple scattering in the material between the vertex and Forward Muon Detector has shown these features to be well modelled by the material simulation of the H1 detector.

Appendix A

Removal of Inelastic Events

In chapter 6 the number of events comprising class X and Y were denoted N_X and N_Y respectively. We sought to correct the former value according to the number of events from the dissociative process which pass all elasticity and proton-veto cuts, leaving us with a number which we labelled N_X^{corr} . Re-arranging equation 6.3 we can write equation A.1.

$$N_X^{corr} = \zeta_1 N_X + \zeta_2 N_Y \quad (\text{A.1})$$

where the values of ζ_1 and ζ_2 are given by

$$\begin{aligned} \zeta_1 &= \frac{1}{\mathcal{E}_X^{elas} - \mathcal{E}_Y^{elas} \left(\frac{\mathcal{E}_X^{diss}}{\mathcal{E}_Y^{diss}} \right)} \\ \zeta_2 &= \frac{1}{\mathcal{E}_Y^{elas} - \mathcal{E}_X^{elas} \left(\frac{\mathcal{E}_Y^{diss}}{\mathcal{E}_X^{diss}} \right)} \end{aligned} \quad (\text{A.2})$$

The meanings of the values $\mathcal{E}_{X,Y}^{elas}$ and $\mathcal{E}_{X,Y}^{diss}$ are given in chapter 6, and are now labelled \mathcal{E}_j where $j = 1 \rightarrow 4$, i.e. $\mathcal{E}_j = (\mathcal{E}_X^{elas}, \mathcal{E}_Y^{elas}, \mathcal{E}_X^{diss}, \mathcal{E}_Y^{diss})$. The errors on the values of \mathcal{E}_j in equation A.2 are known to us, but are correlated with each other.

Range of $W_{\gamma p}$	<i>Forward</i>	<i>Central</i>		
	30 \rightarrow 80	40 \rightarrow 90	90 \rightarrow 120	120 \rightarrow 180
ζ_1	1.225	1.036	1.023	1.029
$\Delta\zeta_1$	0.058	0.042	0.041	0.042
ζ_2	-0.313	-0.204	-0.184	-0.196
$\Delta\zeta_2$	0.132	0.083	0.074	0.079
N_X	14.5	57.5	51.1	35.7
N_Y	17.0	52.1	33.2	41.0
N_X^{corr}	12.4	48.9	46.2	28.7
ΔN_X^{corr}	2.4	5.0	3.2	3.6

Table A.1: Values of ζ_i ($i = 1, 2$) used in the correction for dissociative events shown for each bin of centre of mass energy $W_{\gamma p}$.

In order to correctly calculate the error on the values ζ_i ($i = 1, 2$), we use a covariance method as shown by equation A.3. In equation A.3 the covariance matrix V_{jk} is a 4×4 array, with the partial derivatives $\frac{\partial\zeta_i}{\partial\mathcal{E}_j}$ and $\frac{\partial\zeta_i}{\partial\mathcal{E}_k}$ both forming 4×1 rectangular matrices.

$$(\Delta\zeta_i)^2 = \sum_{jk=1}^4 \frac{\partial\zeta_i}{\partial\mathcal{E}_j} V_{jk} \frac{\partial\zeta_i}{\partial\mathcal{E}_k} \quad (i = 1, 2) \quad (\text{A.3})$$

The terms contained within the covariance matrix V_{jk} come from the errors on the \mathcal{E} values. We saw in table 6.9 that the uncertainty on the acceptances to classes X or Y was 4% for elastic simulation, and 20% for proton-dissociative simulation. We denote these values by the factors $\mathcal{F}_e = 0.04$ and $\mathcal{F}_d = 0.2$ respectively. The matrix V_{jk} is then of the form shown in equation A.4.

$$V_{jk} = \begin{pmatrix} \mathcal{F}_e^2 \mathcal{E}_1 \mathcal{E}_1 & -\mathcal{F}_e^2 \mathcal{E}_1 \mathcal{E}_2 & \mathcal{F}_e^2 \mathcal{E}_1 \mathcal{E}_3 & -\mathcal{F}_e^2 \mathcal{E}_1 \mathcal{E}_4 \\ -\mathcal{F}_e^2 \mathcal{E}_2 \mathcal{E}_1 & \mathcal{F}_e^2 \mathcal{E}_2 \mathcal{E}_2 & -\mathcal{F}_e^2 \mathcal{E}_2 \mathcal{E}_3 & \mathcal{F}_e^2 \mathcal{E}_2 \mathcal{E}_4 \\ \mathcal{F}_e^2 \mathcal{E}_3 \mathcal{E}_1 & -\mathcal{F}_e^2 \mathcal{E}_3 \mathcal{E}_2 & \mathcal{F}_d^2 \mathcal{E}_3 \mathcal{E}_3 & -\mathcal{F}_d^2 \mathcal{E}_3 \mathcal{E}_4 \\ -\mathcal{F}_e^2 \mathcal{E}_4 \mathcal{E}_1 & \mathcal{F}_e^2 \mathcal{E}_4 \mathcal{E}_2 & -\mathcal{F}_d^2 \mathcal{E}_4 \mathcal{E}_3 & \mathcal{F}_d^2 \mathcal{E}_4 \mathcal{E}_4 \end{pmatrix} \quad (\text{A.4})$$

Table A.1 shows the values of ζ_i calculated from equations A.2 together with their errors calculated from equations A.3 and A.4. Once we have these values we can use the relation shown in equation A.5 to find the systematic error on the corrected number of elastic events N_X^{corr} due to those on the four \mathcal{E}_j values.

$$(\Delta N_X^{corr})^2 = \Delta\zeta_1^2 N_X^2 + \Delta\zeta_2^2 N_Y^2 \quad (\text{A.5})$$

Also shown in table A.1 are the event totals of each of classes X and Y , the corrected numbers of elastic events N_X^{corr} and their resultant systematic error.

References

- [1] I. Abt et al. The H1 Detector at HERA. *DESY Pre-print*, **93-103**, (1993).
- [2] H. Jung, G. A. Schuler, J. Terron. J/ψ -Production Mechanisms and Determination of the Gluon Density at HERA. *DESY Pre-print*, **92-028**, (1992).
- [3] G. A. Beck et al. Paper Submitted to the Vienna Wire Chamber Conference. (1995).
- [4] S. E. Burke et al. Track Finding and Fitting in the H1 Forward Track Detector. *H1 Note*, **H1-03/95-434**, (1993).
- [5] J. Bürger et al. The Central Jet Chamber of the H1 Experiment. *Nucl. Instr. and Meth.*, **A279**:217, (1989).
- [6] B. Andrieu et al. Beam Tests and Calibration of the H1 Liquid Argon Calorimeter with Electrons. *Nucl. Instr. and Meth.*, **A350**:57, (1994).
- [7] B. Andrieu et al. Results From Pion Calibration Runs for the H1 Liquid Argon Calorimeter. *Nucl. Instr. and Meth.*, **A336**:499, (1993).
- [8] P. Biddulph et al. The H1 Forward Muon Spectrometer. *DESY Pre-print*, **93-020**, (1993).
- [9] A. Mehta. Measurement of the Diffractive Proton Structure Function. *University of Manchester PhD Thesis*, (1995).
- [10] P. Bispham. Laser Calibration of the Forward Muon Drift Chambers of the H1 Detector. *University of Manchester Diploma Report*, (1993).

- [11] R. K. Griffiths. Drift Chamber Calibration using Laser Ionization. *University of Manchester MSc Thesis*, (1994).
- [12] L. Favart. Integrated Luminosity Measurement using Bethe-Heitler Overlapping Events. *H1 Note*, **H1-06/94-366**, (1994).
- [13] B. List. Diffraktive J/ψ -Produktion in Elektron-Proton-Stößen am Speicherring HERA. *H1 Note*, **H1-10/93-319**, (1993).
- [14] J. E. Augustin et al. Discovery of a Narrow Resonance in e^+e^- Annihilation. *Phys. Rev. Lett.*, **33**:1406, (1974).
- [15] J. J. Aubert et al. Experimental Observation of a Heavy Particle J . *Phys. Rev. Lett.*, **33**:1404, (1974).
- [16] M. Aguilar-Benitez et al. *Particle Properties Data Booklet*, (1994).
- [17] T. H. Bauer et al. The Hadronic Properties of the Photon in High-Energy Interactions. *Rev. Mod. Phys.*, **50**:261, (1978).
- [18] B. H. Denby et al. Inelastic and Elastic Photoproduction of J/ψ (3097). *Phys. Rev. Lett.*, **52**:795, (1984).
- [19] P. L. Frabetti et al. A Measurement of Elastic J/ψ Photoproduction Cross Section at Fermilab E687. *Phys. Lett.*, **B316**:197, (1993).
- [20] M. Arneodo et al. Quasi-Elastic J/ψ Muoproduction from Hydrogen, Deuterium, Carbon and Tin. *Phys. Lett.*, **B332**:195, (1994).
- [21] A. Donnachie and P. V. Landshoff. Elastic Scattering and Diffraction Dissociation. *Nucl. Phys.*, **B244**:322, (1984).
- [22] P. V. Landshoff. Talk Presented at the Institute of Physics Meeting on Diffraction in Deep Inelastic Scattering, Imperial College, London. June (1995).
- [23] T. Ahmed et al. Photoproduction of J/ψ Mesons at HERA. *Phys. Lett.*, **B338**:507, (1994).

- [24] R. Barate et al. Measurement of J/ψ and ψ' Real Photoproduction on Lithium-6 at a Mean Energy of 90 GeV. *Z. Phys.*, **C33**:505, (1987).
- [25] T. Sjöstrand and M. Bengtsson. The Lund Monte Carlo for Jet Fragmentation and e^+e^- Physics. *Comp. Phys. Comm.*, **43**:367, (1987).
- [26] M.G. Ryskin. Diffractive J/ψ Electroproduction in LLA QCD. *Z. Phys.*, **C57**:89, (1993).
- [27] Ed. U Amaldi. Proceedings of the Study of an ep Facility for Europe. *DESY Pre-print*, **79-48**:391–394, (1979).
- [28] J.P. Sutton. *Private Communication*, (1995).
- [29] G. Schmidt. Nachweis von Myonen im H1-Kalorimeter. *University of Hamburg Diploma Thesis*, (1994).
- [30] C. Hilton. Forward Muon Detection in H1 and Hadronic Energy Flow in DIS. *University of Manchester PhD Thesis*, (1993).
- [31] J.P. Sutton. Talk Presented to the Regular H1 Group Meeting. March (1996).
- [32] J.P. Sutton. *Private Communication*, (1996).
- [33] A. Mehta. *Private Communication*, (1995).
- [34] C. Hilton. *Private Communication*, (1996).
- [35] M. Derrick et al. Measurement of the Cross Section for the Reaction $\gamma p \rightarrow J/\psi p$ with the ZEUS Detector at HERA. *DESY Pre-print*, **95-052**, (1995).
- [36] T. Jansen. Untersuchung Diffraktiver J/ψ Erzeugung bei HERA. *University of Hamburg PhD Thesis*, (1995).
- [37] S. Schiek and G. Schmidt. Talk Presented to the Heavy Quark Working Group Meeting at DESY, Hamburg. May (1995).
- [38] H1 Luminosity Group. Official Summary Tables. (1995).

- [39] V. N. Gribov et al. Covariant Derivation of the Weizsäcker-Williams Formula. *Sov. Phys. JETP*, **14**:1308, (1962).
- [40] V. M. Budnev et al. Equivalent Photon Approximation. *Phys. Rev.*, **C15**:181, (1975).
- [41] C. F. Weizsäcker. Ausstrahlung bei Stößen Sehr Scheller Elektronen. *Z. Phys.*, **88**:612, (1934).
- [42] J. J. Aubert et al. Production of Charmonium in 250 GeV μ^+ -Iron Interactions. *Nucl. Phys.*, **B213**:1, (1983).
- [43] M. Binkley et al. J/ψ Photoproduction from 60 to 300 GeV/c. *Phys. Rev. Lett.*, **48**:73, (1982).
- [44] J. E. Wiss, S. D. Holmes, W. Lee. High-Energy Photoproduction of Charmed States. *Ann. Rev. Nucl. Part. Sci.*, **35**:397, (1985).
- [45] I. Abt et al. Scaling Violations of the Parton Structure Function F_2 at Small x . *Phys. Lett.*, **B321**:161, (1994).
- [46] S. Aid et al. The Gluon Density in the Proton at Low x from a QCD Analysis of F_2 . *DESY Pre-print*, **95-081**, (1995).
- [47] S. Aid et al. A Direct Determination of the Gluon Density in the Proton at Low x . *DESY Pre-print*, **95-086**, (1995).
- [48] B. Gittleman et al. Photoproduction of the $\psi(3100)$ Meson at 11 GeV. *Phys. Rev. Lett.*, **35**:1616, (1975).
- [49] T. Nash et al. Measurement of $J/\psi(3100)$ Photoproduction in Deuterium at a Mean Energy of 55 GeV. *Phys. Rev. Lett.*, **36**:1233, (1976).
- [50] B. Burow. Results from the ZEUS and H1 Experiments at HERA on the Total Photoproduction Cross Section and its Contributions. *DESY Pre-print*, **94-215**:19, (1994).

Acknowledgements

After reading the acknowledgements of a few other theses, my main concern in writing mine is producing something that won't make me cringe in a few years time. Read any of a number of other theses to see what I mean.

Thanks to my supervisor Mike Ibbotson, not least for proof-reading skills, Roger Barlow for statistics help, John Dainton for expressing interest in my work and Fred Loebinger for enlisting me in the first place. John Banks, Joe Foster and Stuart Wild have been very helpful in maintaining the computer system at Manchester.

I owe Chris Hilton a huge debt for a great deal of help since I first set foot in Hamburg. He definitely deserves a pay rise in my opinion. Dave Milstead gave tireless help in the face of much ignorance. Thanks also to the Forward Muon group, Heavy Quark group, Guido Schmidt and Stephan Schiek (who I'm convinced are joined at the hip), Thomas Jansen, Benno List and Roland Martin.

Special thanks to Jennifer Bramley for enduring my 18 months in Germany and helping me run up the highest international telephone bill I've ever seen. Her moral support and also that from my parents, my sister Christine and her recently-acquired husband Tony was very important. Goodbye to Uncle Joey my Godfather, who died this year.

Some friends from Hamburg not already mentioned: Mark Burton, John Lomas, Verena Veitinger, 'Big Al' Wilson, Stuart Robinson and that clown Paul Sutton. Thanks and commiserations to Andy Mehta, Alison Wright and Ben Waugh for having to share an office with me. Thanks also to Phil Biddulph, who has entered

the higher echelons of the H1 directorate. Slept his way to the top I reckon. Other members of the Birmingham UK group not yet thanked are Vicky Hudgson, Paul Newman, Kirstee Hewitt and Lee West. Much gratitude to Mr Lomas for pointing out a regional *faux pas* just now in my acknowledgement of 'tragic' Tim Nicholls. Susan Ketels was very helpful and cheerful in much the same way as my landlord Hr. Seeger wasn't. Thanks to the Hamburg citizen who stole Andy Mehta's glasses off his face when he fell asleep drunk on the S-Bahn. It took us a good week to stop laughing. Who said the Germans have no sense of humour? By the way, did anyone ever find out who drew these ☺ all over Hamburg?

A mention for my late friend from school Danny Hughes to whom this thesis is dedicated. One of the cleverest and most decent people I have ever met, it was he together with Tilman Kleinhans our teacher at school, who were largely responsible for my decision to study Physics at University. Thanks to you both.

Finally, hello to very good friends from Manchester Dave Hutchinson and Steve Lane. For some reason it's always my fault when either of them get drunk or have a hangover. Dave thinks I owe him a fortune from the price difference in our drinks when we go in rounds at the pub, but if he thinks he's seeing any of it again he's sadly mistaken. Greetings to his girlfriend Caroline. Hello also to Rob Akers for visits to that awful awful nightclub. I haven't been there or touched Stella Artois since you left Manchester. Cheers to Stuart Barnett the rock god. Nick Lumb (M.Chef) deserves a mention for being an endless source of amusement while I was writing up. Ask him what his middle name is next time you see him. Now in Greece but a good friend is Nicos Petropoulos and his *ceegarettes*. Jabez Clegg (Physics Department South) and its staff, Babylon cheap pizza company (Manchester), Ronald McDonald (Hamburg) and late-night petrol stations everywhere have pretty much kept me alive for the last three years. Apologies to anyone I have accidentally missed out. And...some people are on the pitch...they think it's all over...it is now.

Pete Bispham

March 1996